UNIVERSIDAD POLITÉCNICA DE MADRID

ESCUELA TÉCNICA SUPERIOR DE INGENIEROS DE TELECOMUNICACIÓN

Methods for the analysis of multi-scale cell dynamics from fluorescence microscopy images

Ph.D. Thesis

David Pastor Escuredo, Eng., M.Sc.

2015

Departamento de Ingeniería Electrónica
Escuela Técnica Superior de Ingenieros de Telecomunicación
Universidad Politécnica de Madrid (2015)

Ph.D. Thesis:
Methods for the analysis of multi-scale cell dynamics from fluorescence microscopy images

Author:
David Pastor Escuredo, Eng., M.Sc.

Thesis supervisors:
María Jesús Ledesma Carbayo, Prof. and Andrés Santos LLeó, Full Prof.

POLITÉCNICA
"Ingeniamos el futuro"

CAMPUS
DE EXCELENCIA
INTERNACIONAL

Tribunal nombrado por el Sr. Rector Magnífico de la Universidad Politécnica de Madrid, el día _____ de _____ de 2015.

Presidente: _____.

Vocal: _____.

Vocal: _____.

Vocal: _____.

Secretario: _____.

Suplente: _____.

Suplente: _____.

Realizado el acto de defensa y lectura de la Tesis el día _____ de _____ de 2015, en la E.T.S.I. de Telecomunicación.

Calificación _____.

_____ _____

EL PRESIDENTE LOS VOCALES

_____

EL SECRETARIO

ABSTRACT

The embryogenesis is the process from which a single cell turns into a living organism. Through several stages of development, the cell population proliferates at the same time the embryo shapes and the organs develop gaining their functionality. This is possible through genetic, biochemical and mechanical factors that are involved in a complex interaction of processes organized in different levels and in different spatio-temporal scales. The embryogenesis, through this complexity, develops in a robust and reproducible way, but allowing variability that makes possible the diversity of living specimens. The advances in physics of microscopes and the appearance of fluorescent proteins that can be attached to expression chains, reporting about structural and functional elements of the cell, have enabled for the in-vivo observation of embryogenesis. The imaging process results in sequences of high spatio-temporal resolution $3D+time$ data of the embryogenesis as a digital representation of the embryos that can be further analyzed, provided new image processing and data analysis techniques are developed.

One of the most relevant and challenging lines of research in the field is the quantification of the mechanical factors and processes involved in the shaping process of the embryo and their interactions with other embryogenesis factors such as genetics. Due to the complexity of the processes, studies have focused on specific problems and scales controlled in the experiments, posing and testing hypothesis to gain new biological insight. However, methodologies are often difficult to be exported to study other biological phenomena or specimens. This PhD Thesis is framed within this paradigm of research and tries to propose a systematic methodology to quantify the emergent deformation patterns from the motion estimated in *in-vivo* images of embryogenesis. Thanks to this strategy it would be possible to quantify not only local mechanisms, but to discover and characterize the scales of mechanical organization within the embryo.

The framework focuses on the quantification of the motion kinematics (deformation and strains), neglecting the causes of the motion (forces), from images in a non-invasive way. Experimental and methodological challenges hamper the quantification of exerted forces and the mechanical properties of tissues. However, a descriptive framework of deformation patterns provides valuable insight about the organization and scales of the mechanical interactions, along the embryo development. Such a characterization would help to improve mechanical models and progressively understand the complexity of embryogenesis.

This framework relies on a Lagrangian representation of the cell dynamics system based on the trajectories of points moving along the deformation. This approach of analysis enables the reconstruction of the mechanical patterning as experienced by the cells and tissues. Thus, we can build temporal profiles of deformation along stages of development, comprising both the instantaneous events and

the cumulative deformation history.

The application of this framework to $3D + time$ data of zebrafish embryogenesis allowed us to discover mechanical profiles that stabilized through time forming structures that organize in a scale comparable to the map of cell differentiation (fate map), and also suggesting correlation with genetic patterns. The framework was also applied to the analysis of the amnioserosa tissue in the drosophila's dorsal closure, revealing that the oscillatory contraction triggered by the acto-myosin network organized complexly coupling different scales: local force generation foci, cellular morphology control mechanisms and tissue geometrical constraints.

In summary, this PhD Thesis proposes a theoretical framework for the analysis of multi-scale cell dynamics that enables to quantify automatically mechanical patterns and also offers a new representation of the embryo dynamics as experienced by cells instead of how the microscope captures instantaneously the processes. Therefore, this framework enables for new strategies of quantitative analysis and comparison between embryos and tissues during embryogenesis from *in-vivo* images.

RESUMEN

La embriogénesis es el proceso mediante el cual una célula se convierte en un ser un vivo. A lo largo de diferentes etapas de desarrollo, la población de células va proliferando a la vez que el embrión va tomando forma y se configura. Esto es posible gracias a la acción de varios procesos genéticos, bioquímicos y mecánicos que interaccionan y se regulan entre ellos formando un sistema complejo que se organiza a diferentes escalas espaciales y temporales. Este proceso ocurre de manera robusta y reproducible, pero también con cierta variabilidad que permite la diversidad de individuos de una misma especie. La aparición de la microscopía de fluorescencia, posible gracias a proteínas fluorescentes que pueden ser adheridas a las cadenas de expresión de las células, y los avances en la física óptica de los microscopios han permitido observar este proceso de embriogénesis *in-vivo* y generar secuencias de imágenes tridimensionales de alta resolución espacio-temporal. Estas imágenes permiten el estudio de los procesos de desarrollo embrionario con técnicas de análisis de imagen y de datos, reconstruyendo dichos procesos para crear la representación de un embrión digital. Una de las más actuales problemáticas en este campo es entender los procesos mecánicos, de manera aislada y en interacción con otros factores como la expresión genética, para que el embrión se desarrolle. Debido a la complejidad de estos procesos, estos problemas se afrontan mediante diferentes técnicas y escalas específicas donde, a través de experimentos, pueden hacerse y confrontarse hipótesis, obteniendo conclusiones sobre el funcionamiento de los mecanismos estudiados.

Esta tesis doctoral se ha enfocado sobre esta problemática intentando mejorar las metodologías del estado del arte y con un objetivo específico: estudiar patrones de deformación que emergen del movimiento organizado de las células durante diferentes estados del desarrollo del embrión, de manera global o en tejidos concretos. Estudios se han centrado en la mecánica en relación con procesos de señalización o interacciones a nivel celular o de tejido. En este trabajo, se propone un esquema para generalizar el estudio del movimiento y las interacciones mecánicas que se desprenden del mismo a diferentes escalas espaciales y temporales. Esto permitiría no sólo estudios locales, si no estudios sistemáticos de las escalas de interacción mecánica dentro de un embrión. Por tanto, el esquema propuesto obvia las causas de generación de movimiento (fuerzas) y se centra en la cuantificación de la cinemática (deformación y esfuerzos) a partir de imágenes de forma no invasiva. Hoy en día las dificultades experimentales y metodológicas y la complejidad de los sistemas biológicos impiden una descripción mecánica completa de manera sistemática. Sin embargo, patrones de deformación muestran el resultado de diferentes factores mecánicos en interacción con otros elementos dando lugar a una organización mecánica, necesaria para el desarrollo, que puede ser cuantificado a partir de la metodología propuesta en esta tesis.

La metodología asume un medio continuo descrito de forma Lagrangiana (en función de las

trayectorias de puntos materiales que se mueven en el sistema en lugar de puntos espaciales) de la dinámica del movimiento, estimado a partir de las imágenes mediante métodos de seguimiento de células o de técnicas de registro de imagen. Gracias a este esquema es posible describir la deformación instantánea y acumulada respecto a un estado inicial para cualquier dominio del embrión. La aplicación de esta metodología a imágenes $3D + t$ del pez zebra sirvió para desvelar estructuras mecánicas que tienden a estabilizarse a lo largo del tiempo en dicho embrión, y que se organizan a una escala semejante al del mapa de diferenciación celular y con indicios de correlación con patrones de expresión genética. También se aplicó la metodología al estudio del tejido amnioserosa de la Drosophila (mosca de la fruta) durante el cierre dorsal, obteniendo indicios de un acoplamiento entre escalas subcelulares, celulares y supracelulares, que genera patrones complejos en respuesta a la fuerza generada por los esqueletos de acto-myosina.

En definitiva, esta tesis doctoral propone una estrategia novedosa de análisis de la dinámica celular multi-escala que permite cuantificar patrones de manera inmediata y que además ofrece una representación que reconstruye la evolución de los procesos como los ven las células, en lugar de como son observados desde el microscopio. Esta metodología por tanto permite nuevas formas de análisis y comparación de embriones y tejidos durante la embriogénesis a partir de imágenes *in-vivo*.

Contents

Chapter 1

Introduction

1.1 Motivation

Recent advances in microscopy imaging techniques allow scientists to observe developmental biological processes at a microscopic scale [Peng, 2008, Kitano et al., 2002, Megason and Fraser, 2007]. The revolution of fluorescence microscopy [Stearns, 1995] enabled biologists to label biological structures during embryogenesis such as cell membranes or cell nuclei and also to obtain functional images of marking gene expression as well as actomyosin networks as proxy indicators of mechanical stresses. In this context, image processing and data analysis techniques are being developed to digitize and process these data for further analysis and ultimately extract biological insights [Doursat, 2008, Castro-González et al., 2010, Oates et al., 2009, Luengo-Oroz et al., 2011].

These experimental and methodological advances have led to the expansion of biological studies in genetics, morphogenesis, biomechanics, cell migration or cells interaction. *In-vivo* imaging techniques open new opportunities and paradigms through the observation of biological phenomena in a non-invasive way [Khairy and Keller, 2011, Megason et al., 2011] integrating different types of analysis to empower biological research on several animal models [Fernandez et al., 2010, Gorfinkiel et al., 2011, Supatto et al., 2009]. Thus, the main goal of the uprising bio-image informatics field is to digitally reconstruct the underlying biology phenomena from structural and functional imaging by quantitative, robust and reliable methods that can be applied to different problems exploiting the large pool of bioimage data available (see Fig. 1.1).

Furthermore, new challenges beyond the digital reconstruction of the development such as the characterization of the embryonic mechanics factors, the spatio-temporal organization of the genome and the characterization of other epigenetic factors. The ultimate objective is therefore to understand the contribution and interplay of the genetic and epigenetic factors determining the embryogenesis.

This PhD Thesis focuses in the quantification and characterization of spatio-temporal mechanical patterns that act shaping the embryo and determining relevant tissue behaviours. The approxima-

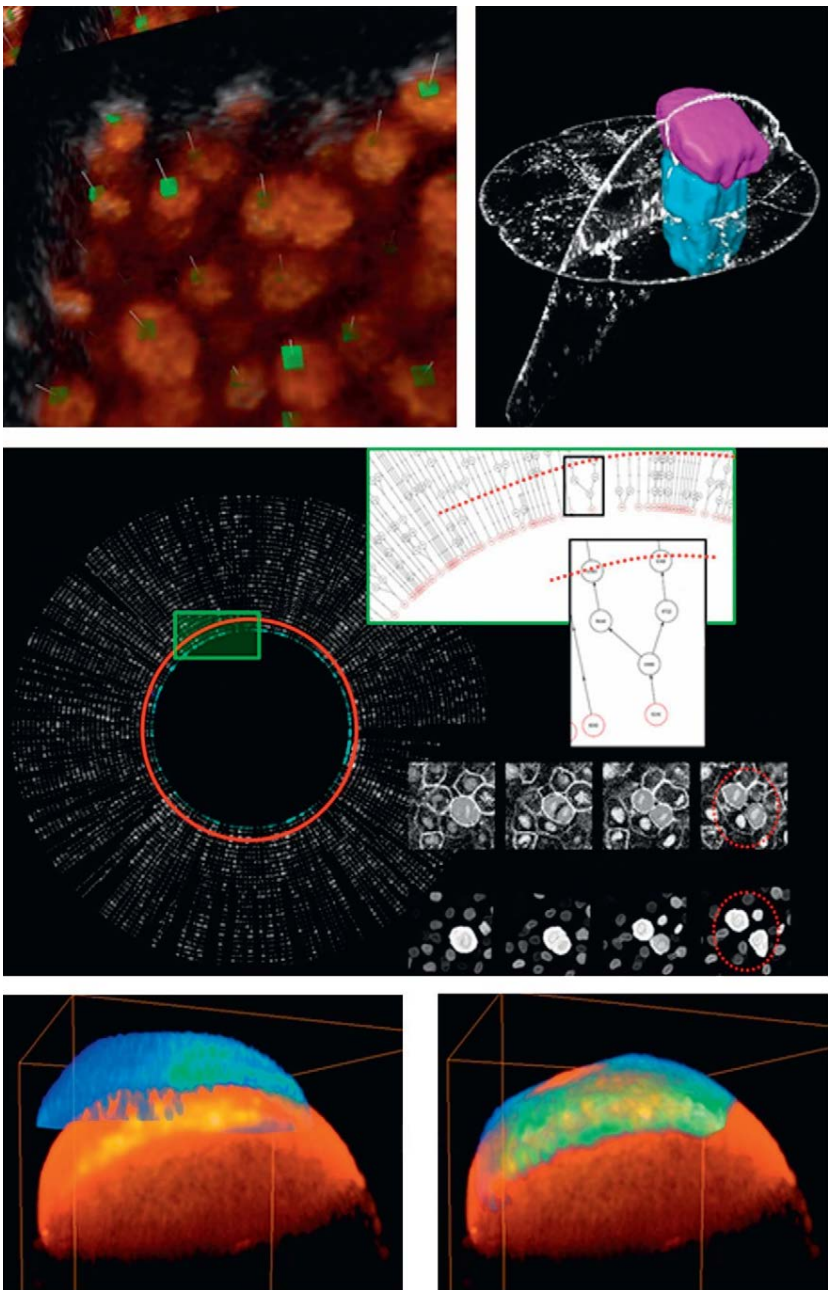

Figure 1.1: Digital reconstruction of embryogenesis: Top row: cell detection (left) cell segmentation (right). Middle row: cell tracking. Bottom row: building templates of gene expression (from [Luengo-Oroz et al., 2011]).

tion to *in-vivo* mechanics quantification must be conceived as a multi-scale analysis ([Stearns, 1995, Asnacios and Hamant, 2012, Farhadifar et al., 2007, Wang and Lin, 2007] that focused not only on the cell behavior, but also on subcellular behaviour, mesoscopic patterns and large scale embryonic mechanical structures.

Cell migration dynamics determine many organism processes such as those related to the immunological system or healing and the misfunctionality of these processes can cause multiple diseases including some types of cancer [Jonietz, 2012]. Mechanics can determine how cells interact with the Extra Cellular Matrix (ECM) or with surrounding cells [Maruthamuthu et al., 2011, Zamir et al., 2008, Lecuit and Lenne, 2007, McCain et al., 2012], how cells migrate and how they adapt to the environment exerting forces and change their shape according to the mechanical properties and the activity of mechanical sensing through integrins and cadherins proteins [Arciero et al., 2011, Trepat et al., 2009, Tambe et al., 2011, Heisenberg and Bellaïche, 2013].

On the other hand, large-scale collective cell migration during embryogenesis is part of the shaping mechanism during embryo development that eventually define the morphogenesis of tissue and organs in a complex system of concurrent and regulated processes at different scales [Rauzi et al., 2010, Kennaway et al., 2011, Davidson et al., 2009]. Recent studies also show that mechanics act as an epigenetic factor during embryogenesis through mechano-sensing where cell-cell and cell-ECM interaction mechanisms play an important role in individual cell behavior, for instance, triggering apoptosis or mitosis, or defining signaling pathways necessary to control embryogenesis or affecting the normal migration patterns producing diseases [Keller et al., 2000, Herszterg et al., 2013, von Dassow and Davidson, 2007, Levental et al., 2009, Guillot and Lecuit, 2013]. Mechanical processes are important not only at the cell level, the also conform a multi-scale system that comprises active force generation (actin-myosin structures activity) and passive behavior through mechano-sensing and signaling (based on cadherin and integrin functionality) that help to configure tissue properties and coordinate large-scale force transmission [Davidson et al., 2009, Lecuit et al., 2011]. Both active and passive mechanical processes are equally important to understand the development of embryos [Heisenberg and Bellaïche, 2013, Keller et al., 2003].

The study of *in-vivo* mechanics during embryogenesis is necessary to understand and measure how forces interactions contribute to two main characteristics of life generation: robustness and variability. Robustness ensures life and phenotype identification in the species. Variability ensures the differences in life and individuals of the same species. Mechanics are believed to actively shape tissues during embryogenesis and also passively regulate their behavior. Therefore, only by quantifying mechanics accurately, research will be able to understand, model and predict mechanisms involved in important biological phenomena such as cell migration, embryogenesis stages transitions, phenotyping or tissue differentiation with scientific, clinical and engineering purposes.

In this PhD Thesis, the strategies and methodologies to quantify mechanics from *in-vivo* imag-

ing have been reviewed, proposing new concepts and implementations that have required an integrative research comprising bioimage technologies, systems biology, machine learning, mathematics and physics. This research has been applied to real biological problems in the state-of-the-art of developmental biology helping to generate multi-scale characterization of mechanics pointing to new biological insights.

1.2 Objectives

The main objective of this Thesis is **to design, develop and validate a well-founded methodology to study multi-scale mechanics in complex $2D/3D+t$ bioimage data of embryogenesis acquired with fluorescence microscopy techniques**. Such a methodology would help to reach a better understanding of how biomechanical patterns can be identified and analyzed from image data and also provide biological insight in applied studies. Therefore, a framework will be developed considering theoretical and methodological aspects in order to successfully extract meaningful insight from different biological problems.

Concretely, the strategy proposed relies on the motion estimation of cell structures marked with fluorescent proteins in sequences of high spatio-temporal resolution images (seconds-minutes of time resolution and μm of spatial resolution). That estimation would allow us to build a multi-scale description of deformation and strain patterns, as a characterization of the embryo, neglecting the quantification of stresses[1]. Therefore, this PhD Thesis focuses on the *kinematics of embryogenesis*, describing the motion along stages of development without considering its causes (i.e. forces). The quantification of the stresses would additionally require the characterization of tissue mechanical properties to pose an inverse problem or experimental setups allowing the sensing of applied forces. Although some strategies have been proposed in these directions [Ishihara et al., 2013, Campas et al., 2014], the technology and methods are not mature enough to provide high throughput information of accurate and reliable stresses characterization. Nevertheless, due to the level of mechanical factors and interactions, deformation patterns provide a very valuable quantitative description of the shaping process that integrates several embryogenesis mechanisms. Here, we aim at providing a multi-scale characterization of patterns that would help to understand mesoscopic and embryonic constraints in the embryo and how subcellular and cellular mechanisms coordinated and synchronized lead to larger scale patterns necessary to shape the embryo and configure its organs and tissues [Keller, 2012].

In order to fulfill this objective, we distinguished specific goals within this PhD Thesis, being divided in theoretical and methodological goals, focused on the foundation and implementation of a framework of analysis, and also in biology oriented goals that exploit the framework and illustrate its

[1]From now on the term "mechanical description" will be generally used considering that no forces nor stresss are inferred, neither mechanical properties such as viscosity or stiffness.

potential.

From a theoretical perspective, this PhD Thesis addresses how mechanical processes can be quantified from images and their digital reconstruction. We grounded the methodology with continuum mechanics theory relying on a Lagrangian representation of the cell dynamics. This representation of physical dynamics is based on a particle-based description of the system, so the quantification of the motion is expressed in terms of trajectories (movement of fluid particles or material points of a solid). This representation is alternative to the Eulerian perspective that is based on spatial representation of the system referred to an external observer. Interestingly, the way processes are imaged with microscopes external to the embryo has led to a generalized Eulerian approach of analysis of biological phenomena. The study of deformation patterns in embryogenic tissues from *in-vivo* images has been restricted to an analysis of deformation from the displacements and cell morphology dynamics between time steps [Blanchard et al., 2009, Bosveld et al., 2012]. This approach provides a detailed description of mechanical patterns and interactions with other genetic and biochemical factors, but do not produce a description of the temporal scales of the patterns required to understand how mechanical patterns affecting cells evolve through time. The reconfiguration of the tissues along the shaping process requires a Lagrangian framework to better characterize the different length-scales of the processes. The cells move at the same time embryos are shaped, therefore, the mechanical patterns seen from an Eulerian perspective can only be mapped instantaneously (in the same way the embryo is observed from the microscope). However, within a Lagrangian (material) analysis, mechanical patterning can be quantified in finite time intervals along the trajectories

From a methodological perspective, this PhD Thesis aims at implementing a flexible framework that would provide such a characterization of mechanics for different types of images. More specifically, we will differentiate between discrete and continuous techniques of motion estimation to build a unique framework based on a continuum mechanics description. Such a framework will enable to study different biological phenomena observed with different types of images according to their resolution, marked structures and scales of movement.

From the developmental biology research perspective, this PhD Thesis pretends to exploit the designed methodology to better quantify and understand dynamics during embryogenesis in animal models. Specifically, new strategies will be required to understand the role of mechanical patterns in the shaping process of embryogenesis and the behavior of tissues in Drosophila and zebrafish *in-vivo* data provided by the biology researchers partners involved in this PhD Thesis.

To summarize, this PhD Thesis gets into the cross-roads between bioimage processing, informatics, computational solid mechanics and computational fluid dynamics, tackling the challenging problem of providing quantitative assessments of the complex multi-scale mechanisms involved in the embryogenesis.

1.2.1 A framework to quantify multi-scale mechanics in microscopy images

Image analysis techniques have been designed and implemented to reconstruct the embryogenesis processes observed with *in-vivo* images. This PhD Thesis aims one step further in order to characterize dynamics and mechanical patterning. We will implement a framework that unifies the dynamics implicit in the motion estimated from different image analysis techniques: cell tracking and B-splines sequential registration. Thus, we will propose a common a systematic quantification of mechanical patterns based on a Lagrangian representation of the dynamics. Using analysis tools this patterns will be further investigated in terms of biological domains and tissues. Therefore, the framework will comprise the following modules:

- A continuous motion description of tissue dynamics and cell collective movements
- Estimation of motion using B-splines sequential registration
- Estimation of motion using cell tracking
- A Lagrangian representation of dynamics to compute multi-scale mechanical descriptors
- A framework to generate mechanical profiles for spatial and material domains
- A statistics module to obtain characteristic patterns withing the mechanical description provided
- Interactive visualization tools to relate mechanical descriptors to biological domains

1.2.2 Characterizing the meso-level mechanical patterning during zebrafish embryogenesis

Digital cell lineages provide a spatio-temporal description of the embryogenesis at the cell level, but due to the state of the art in imaging and processing techniques, tracking methods do not produce complete and error-free lineages. Cell-level descriptions therefore do not robustly scale along several stages of development. On the other hand, mechanical patterns analysis based on displacements do not allow to observe different temporal length-scales that are necessary to understand the mechanics of, for example, the zebrafish gastrulation.

The framework proposed can use the digital cell lineage, output by any tracking method with a characterized given error rate, to generate a continuous flow approximation of the dynamics implicit in the displacements of a cell and its neighbors. Therefore, the framework is able to quantify mesoscopic patterning emergent from the interactions of the embryogenesis mechanical factors in different temporal length-scales. Thus, it would be possible to understand patterning in long temporal scales helping to describe how mechanics help to shape the embryos and determine the phenotype configuration. We will apply this strategy to zebrafish embryos imaged with 2-photon fluorecent microscopy

($3D + time$ data of cell nuclei and membranes) to discover the characteristic mechanical patterns and their organization in the temporal length-scale of gastrulation.

1.2.3 Quantification of the contractile behaviour of Drosophila's amnioserosa

The framework proposed is suitable not only to quantify large-scale reconfiguration processes along gastrulation, but also to quantify collective cell behavior within tissues in smaller scales. One tissue of interest is the Drosophila's amnioserosa (AS) during the dorsal closure (DC). AS cells show apical area fluctuations driven by actomyosin contractility. The AS then contracts while the epidermis undergo filopodia-mediated zippering to generate a continuous epidermis at the dorsal side of the Drosophila embryo. In this process, the relevant scales of dynamics go down to the subcellular level and up to the tissue level.

The mechanical patterns underlying this behavior can be also studied with the proposed framework by using B-splines sequential registration to estimate the motion (provided good spatio-temporal resolution of the observation adapted to the scale of the phenomena). We will apply the framework to data of stained cell membranes imaged with confocal microscopy ($2D + time$ data) to generate a continuous spatio-temporal dense description of the tissue that allows focusing on supracellular and subcellular scales. We expect to generalize the analysis done so far in this tissue and provide additional descriptions, showing the potential of this approach to characterize any tissue behavior during development.

1.3 Document Structure

In chapter 2 we will overview the current state of the art in analysis of mechanics in embryogenesis with special focus on studies using *in-vivo* data. From that overview, we will identify then the main challenges and opportunities in the field, concretely in the research of zebrafish and Drosophila embryogenesis processes. In chapter 3 we introduce the motion estimation techniques and the necessary processing to characterize continuous motion from images. Chapter 4 introduces a descriptive framework based on a Lagrangian perspective of analysis to provide multi-temporal length-scale descriptors. We will show the results of applying this framework to the analysis of zebrafish *in-vivo* data in chapter 5, providing a novel characterization of biomechanical profiles of wild-type embryos. Chapter 6 shows the results of applying the continuous motion analysis framework to the study of the Drosophila's amnioserosa (AS) during the Dorsal Closure. Finally, in chapter 7, we will discuss on the contributions of this PhD Thesis and the new challenges open after the achieved results.

Chapter 2

State of the Art

In this Chapter we will overview the necessary bibliography and context to understand the importance of the contribution presented in this PhD Thesis. First, we will address the developmental biology animal models that have been studied: zebrafish (Danio-rerio) and Drosophila melanogaster (fruit-fly). We will describe dynamic processes of interest within these animal models that have been the biological focus of this work. Then, we will overview technical aspects regarding imaging and analysis of *in-vivo* data of embryogenesis. Considering that this Thesis presents a new comprehensive framework to analyze mechanical factors involved in the embryogenesis, the main mechanics oriented studies in the field are discussed in detail pointing out to the missing gaps this PhD Thesis contributes to.

2.1 Biological context

In developmental biology research, some model organisms are used to drive biological research due to practical issues such as cost, ease of culturing, ease of imaging or seasonal availability, as well as biological advantages such as genetic content, phylogenetic similarity to humans and organs functioning. Following sections overview the work carried out in zebrafish and Drosophila melanogaster, both being models largely used in embryogenesis mechanics research.

2.1.1 Zebrafish

The zebrafish is one of the most widely used models to understand vertebrates development. This model, due to its transparency, is very suitable for fluorescent microscopy imaging and has been used as a reference to improve microscopy techniques [Keller, 2013, Olivier et al., 2010, Brend and Holley, 2009]. zebrafish has been also exploited for genetic manipulation and phenotyping, with very well characterized mutants regarding eye and brain development [Tawk et al., 2007, Jessen et al., 2002, Warga and Kane, 2003, England et al., 2006]. Recently, several methodologies have appeared in

order to create genetic atlases of zebrafish, both in early and late stages of its development [Castro-González et al., 2014, Ronneberger et al., 2012, Rittscher et al., 2011, Potikanond and Verbeek, 2012]. Because of its closer phylogenetic position to humans, zebrafish has been subject of toxicology and pharmacology essays [Burns et al., 2005, Hill et al., 2005, Yang et al., 2009].

Zebrafish develops fast, completing the segmentation stage within 24 hours-post-fertilization - hpf-[1], enabling researchers to image several stages of development, trying to understand how the cells differentiate and move through these stages to form the functional map of the cells -fate map- [Woo and Fraser, 1995, Kwan et al., 2012, Blum et al., 2009, Kwan et al., 2012, England et al., 2006, Kimmel et al., 1990, Fleury et al., 2015]. Regarding mechanics, there are studies describing and modeling the dynamics during early stages with special focus on gastrulation [Behrndt et al., 2012, Campinho et al., 2013, Keller et al., 2003, von Dassow and Davidson, 2007, Jessen et al., 2002].

The zebrafish starts developing through synchronous mitosis phases until it reaches the 1024 cells stage [Olivier et al., 2010]. Then the dynamics of the yolk and the epithelium layer help to start the blastula stage and the epipoly progression [Campinho et al., 2013, Behrndt et al., 2012]. The gastrulation onset is produced by an invagination in the hemisphere yet to be understood, but presumably initiated by apical contraction as local force generation mechanism and the EVL as large force generation mechanism. Later stages have been further investigated to compare different mutants and wild-type in terms of neurolation and eye formation [Tawk et al., 2007]. However, no recent studies have investigated the relationship between mechanics of the gastrulation and the fate map configuration [Woo and Fraser, 1995, England et al., 2006, Glickman et al., 2003, Keller, 2012].

2.1.2 Drosophila melanogaster

Drosophila melanogaster, has been widely used in developmental biology research due to its size and cost of culturing. Main recent contributions in imaging have been oriented to output whole-embryo data of this species [Tomer et al., 2012, Pantazis and Supatto, 2014]. The embryos size and the possibility to properly observe them with confocal microscopy motivated plenty of studies in genetic atlases [Fowlkes et al., 2008, Peng et al., 2011] and dynamics of cell migration [Amat et al., 2014] and gastrulation [Supatto et al., 2009, Martin, 2010, McMahon et al., 2008]. This Thesis focuses on the behavior of the Amnioserosa (AS), a tissue that oscillates and contracts during the Drosophila's DC. This tissue helps to drive the closure thanks to ratchet-like behavior of its cells, so the tissue that eventually disappears from the apical plane. Several studies have tried to find the driving forces during DC and the zippering of the epidermis, and understand the complex mechanism that integrates forces at the boundaries of the AS and the internal contraction of the cells forming the tissue [Gorfinkiel et al., 2009, Azevedo et al., 2011, Kiehart et al., 2000, Solon et al., 2009, Blanchard et al., 2010].

[1] http://zfin.org/

The dynamics of the dorsal closure have been extensively studied and characterized (reviewed in [Gorfinkiel et al., 2011]), however, more sophisticated methods are necessary to understand the coupling between the actomyosin networks generating forces and the observed behavior of the AS. The characterization and modeling of exerted forces will be also a major topic of research in Drosophila along with studies crossing signaling information and mechanical descriptions [Machado et al., 2014, Wang et al., 2012, Gorfinkiel, 2013].

2.2 Embryogenesis image data acquisition, processing and visualization

2.2.1 Image acquisition

Imaging techniques are evolving pursuing the *in-toto* observation of embryos during embryogenesis with the maximal temporal and spatial resolution [Megason and Fraser, 2007, Megason, 2009]. Most part of the studies of mechanics analysis have relied on confocal multi-photon Laser-Scanning Microscopy -LSM- because of the good balance between spatial resolution, temporal resolution and imaging artifacts [Megason and Fraser, 2003, Pawley and Masters, 2008, Supatto et al., 2011]. However, this technique loses precision when imaging in depth along the axis of illumination obtaining blurred images that can only be improved at the cost of longer exposure, reducing the temporal resolution and increasing the effect of photo-bleaching and radiation. The spinning-disk microscopy [Pawley and Masters, 2008] was designed to speed up the imaging process, but the spatial resolution of the images is sometimes not sufficient for studying cell structures.

The Light Sheet Fluorescence Microscopy -LSFM- technique, also known as Selective Plane Illumination Microscopy -SPIM-, was introduced trying to avoid the depth limitation of confocal imaging and reduce photo-bleaching, potentially enabling for imaging entire embryos [Meyer, 1979, Keller et al., 2008, Keller and Stelzer, 2008, Pantazis and Supatto, 2014]. However, initial results were not completely satisfactory because of the low temporal resolution and the need to fusion the different views into one single image with a temporal delay between them [Rubio-Guivernau et al., 2012, Temerinac-Ott et al., 2012, Keller, 2013, Preibisch et al., 2008, Maitre and Heisenberg, 2013]. New advances in this technique such as the simultaneous multi-view version of the LSM [Tomer et al., 2012] have allowed imaging the entire Drosophila melanogaster embryo, overcoming the time shift problem. This technique has been also used recently to quantify dynamics at large scales [Pampaloni et al., 2015], for example to study the dynamics of endodermal cells [Schmid et al., 2013] or the cell dynamics in large mouse embryos [Udan et al., 2014]. LSFM has been also enhanced with multi-photon excitation to make multi-color acquisition [Mahou et al., 2014] or to obtain functional images of the whole brain in mouse embryos [Wolf et al., 2015]. Alternative techniques such as bessel-beam plane illumination microscopy allows different operational modes reaching high speed and less photo-bleaching [Gao et al., 2014, 2012].

2.2.2 Digitizing and visualizing live embryos

The previous imaging techniques enable to acquire live images of embryogenesis producing high throughput images that are digitized using image processing methods [Luengo-Oroz et al., 2011, Mikut et al., 2013, Peng, 2008, Keller, 2013]. The ultimate goal defined in this field has been to reconstruct the motion, morphology and functional mechanisms along the development, allowing to generate multi-scale descriptions based on the subcellular-to-cellular-to-embryonic levels data [Amat et al., 2014, Olivier et al., 2010].

Motion estimation can be approached with discrete or continuous methodologies. Typically, embryogenesis is analyzed with cell tracking methods [Meijering et al., 2012, 2009], that can be classified according to the motion model assumed [Maška et al., 2014]. Most part of tracking methods would rely on a cell detection stage and a cell linking stage, but other methods work in the spatio-temporal domain to find connected structures as cell trajectories [Luengo-Oroz et al., 2012, Pastor-Escuredo et al., 2012, Bellaiche et al., 2011]. State of the art tracking workflows are powerful tools that generate cell lineages for different species and large $3D + t$ datasets with linking accuracy above 95% [Amat et al., 2014, E. Faure et al, 2015]. Image correlation techniques such as PIV [Keane and Adrian, 1992], widely used in in-vitro traction force microscopy [Oliver et al., 1998, Hall et al., 2013, Wang and Lin, 2007] for motion estimation are also used to quantify displacements fields during embryogenesis. Integrative frameworks have combined cell based analysis with image correlation techniques to relate cell and tissue level descriptions [Blanchard et al., 2009, Bosveld et al., 2012].

Data visualization is also critical for developmental biology research [Long et al., 2012]. Visualization is intended to have cell level resolution [Keller and Ahrens, 2015] and integrate different sources of data and processing, enabling the interaction with the digital embryos [Pietzsch et al., 2015, Chaumont et al., 2012, E. Faure et al, 2015].

2.3 Methods to study embryogenesis mechanics

Mechanics plays a key role in shaping the embryo, sculpting tissues and organs during the embryogenesis through force generation, force transduction and adaptive mechanical properties of tissues. Mechanics also acts as a regulator of cell proliferation and apoptosis, gene expression and signaling pathways thanks to mechano-sensing mechanisms based on cell-cell and cell-extracellular matrix adhesion [Heisenberg and Bellaïche, 2013, Lecuit et al., 2011]. Conversely, cell and tissue mechanical properties depend on genetics and molecular interactions that determine cell stiffness, adhesive interactions and cell coordination. It could be assumed that embryogenesis is composed of several interacting and concurrent processes at different scales that collaborate to shape the embryo and regulate each other to reach a robust and reproducible unique process that enables the development of embryos of the same phenotype [von Dassow and Davidson, 2007, Haeger et al., 2015].

Quantification of stresses and mechanical properties in embryonic tissues has been approached using invasive experimental techniques [Davidson et al., 2009], specially with laser ablations to observe tissue tensions [Rauzi et al., 2008, Hutson and Ma, 2007]. A less invasive approach has been used to obtain functional images as proxy indicators of mechanical activity by marking actin and myosin [Levayer and Lecuit, 2012, Machado et al., 2014]. However, for understanding the interactions and dependencies of mechanical patterns with other genetic and epigenetic factors [Kwan et al., 2012], it is necessary to quantify dynamics *in-vivo* from the observed motion of biological structures to explore the spatial and temporal scales of the processes shaping the embryo [Blanchard and Adams, 2011, Oates et al., 2009, Keller, 2012].

The advances in *in-vivo* data acquisition and processing overviewed in the previous section, have enabled the quantification of strain and deformation rates from the motion in the images. These techniques are closest state-of-the-art methodologies to the work proposed in this PhD Thesis. Cell based measurements (shape and position) have been exploited to measure local cell shape changes and cell rearrangements derived from a combination of tissue strain rates and cell shape analysis [Blanchard et al., 2009]. Also, discrete analysis approaches have been used to quantify tissue dynamics modeled as a topological network of cells [Graner et al., 2008]. A multi-scale imaging methodology has enabled to combine both cell level measurements and tissue strain rates (image correlation methods) [Bosveld et al., 2012], considering that cell intercalation and shape changes are quantified with the traceless strain rate tensor (deviatoric tensor). This framework also proposes a comparison strategy based on the subtraction of strain rate fields, after spatio-temporal alignment by removing rotation and elongations components of the deformation.

These works are presented for image data in $2D$ (including projections of thin $3D$ volumes into one slice), that simplifies the analysis and visualization, and applied to tissues that show a clear planar behavior and orientation (normally defined as the apical plane) of the mechanical patterning. However, in order to generalize strain and deformation quantification it is necessary to extend methodologies to $3D$ to understand processes with greater geometry complexity. Futhermore, it is necessary to understand large scale processes that not only deform the tissues but also configure the anatomy of the embryo through time [Keller, 2012]. Moreover, not only quantifying this spatial scale of deformation rates is required, but also the deformation and strain along finite intervals of time, as the mechanical processes during embryogenesis might be organized along several temporal length-scales.

Several methodologies are being proposed to not only quantify strain rates, but also stresses. Some of them infer stress rates (absolute stress quantification requires to define a zero-force state) from strain rates by posing an inverse problem assuming certain tissue properties or by modeling the force effects in terms of cell junctions [Chiou et al., 2012, Brodland et al., 2010, 2014, Ishihara and Sugimura, 2012, Fletcher et al., 2014, Ishihara et al., 2013]. A slightly different approach has been to formulate and solve constitutive equations for biological tissues [Tlili et al., 2015]. A recent

approach combines strain rates measurements based on cell morphology with myosin activity to infer mechanical properties assuming linear viscoelasticity of the tissue [Machado et al., in press]. These properties are then used to quantify stresses with laser-cuts.

However, the quantification of mechanics (strain and stresses) in the large scales of embryogeneis processes, such as gastrulation, is not yet addressed from images as it requires. The methodologies we have referred establish mechanical relationships in small spatial scales of the cell and the cell neighboring, but also in small temporal length-scales (as defined by the temporal resolution of the imaging). The quantification of stresses is not addressed in this Thesis (see related discussion in section 7.2.3), but the quantification of multi-scale deformation patterning (kinematics). Thus, it would be possible to provide descriptions to more generally understand the complexity of the mechanical interactions and mechanisms shaping the embryo.

2.4 Mechanics of actomyosin-driven pulsatile contraction

One of the most studied mechanical phenomena in developmental biology is the contraction driven by actomyosin networks (Myo-II motors and F-actin filaments). Due to its importance, we overview separately bibliography about this topic, which is related to the study presented in chapter 6. Actomyosin driven contraction is considered the main force generator in several biological processes such as the tissue invagination during the gastrulation, tissue foldings or the dorsal closure [Kasza and Zallen, 2011, Lecuit and Lenne, 2007, Munjal and Lecuit, 2014]. The mechanism of apical epithelial contraction produced by Myo-II (myosin) during the gastrulation has been studied in Drosophila embryos by comparing the development of wild-types with mutants that mimic Myo-II, finding that a synchronized mechanism of myosin pulses play a fundamental role generating incremental apical constriction and keeping tissue integrity [Vasquez et al., 2014]. Besides, tissue contraction, myosin is also a driving force during tissue rearrangement through intercalation and extension [Paré et al., 2014, Kasza et al., 2014, Bertet et al., 2004, Siedlik and Nelson, 2015].

The Drosophila's Dorsal Closure -DC- is an exceptional biological process involving the interplay between the amniserosa -AS- and the epidermis. The AS is a tissue forming a discontinuity in the epidermis that eventually contracts allowing the closure of the epidermis into a continuous tissue [Kiehart et al., 2000, Gorfinkiel et al., 2011]. The dynamics of the AS has been investigated initially combining imaging of myosin activity and laser cuts [Ma et al., 2009, Hutson et al., 2003] showing that the apical contraction of this tissue depends strongly in the apical myosin networks inside the cells. The myosin networks show a pulsatile behavior producing oscillation in the AS and eventually a progressive ingression of the whole tissue replaced by the epidermis [David et al., 2010, Sokolow et al., 2012, Blanchard et al., 2010, Gorfinkiel and Blanchard, 2011]. One of the main questions is to determine if the AS contraction is sufficient to lead the DC and or the leading edge between the AS

and the epidermis was the main regulator of the process [Solon et al., 2009, Kiehart et al., 2000].

However, there are still open questions about the origin of the pulsatile concentration of apical actomyosin activity and the apical contraction oscillations, and also about mechanical forces driving the net contraction of the AS (tissue level or cell level ratcheting mechanism), so the tissue eventually closes [Gorfinkiel, 2013]. In order to address these questions, a model of AS mechanics has been proposed by [Wang et al., 2012] to explain both the oscillatory behavior and the net contraction. This model uses a network force interaction topology defined by the position of the nodes and elastic forces in the edges combined with signaling of myosin activity that drives the pulsatile behavior. Furthermore, this model combines two temporal scales: the signaling of myosin activity and the relaxation of cells activity defined by viscoelastic properties. The model also tests the two ratchet-like assumptions, showing that the predictions output by the model enforces the hypothesis of a cell level ratcheting that produces the individual cell ingression until the complete zipping of the AS. Another AS model explains the oscillatory behavior through the coupling between active Myosin-driven forces, actin turnover and cell deformation [Machado et al., 2014]. In this model, the net contraction of the AS is driven by an increment of the actin turnover and the myosin force generation. The phenomenology of the contraction is still being analyzed at different scales, trying to explain the emergent tissue behaviors that arise from underlying synchronization mechanisms between cells [Xie and Martin, 2015].

Chapter 3

Estimating Continuous Motion from Microscopy Images

3.1 Unifying continuous and discrete image analysis

Motion estimation methods may be categorize into discrete, continuous and hybrid techniques. Depending on the image features, the scale of the dynamics of the system and the collaborative cell behavior, each strategy will be more suitable to analyze a specific problem. Embryogenesis analysis is fundamentally based on the behavior of the cells, single entities with characterized behavior and properties. However, during some stages, collective behavior can give rise to patterns with scales larger than the cell that can be described with continuous dynamics Keller [2012]. This duality has encouraged our work in the design and implementation of a framework that allows the analysis of bioimage data with either discrete or continuous image processing techniques, unifying both under the same characterization of continuous motion.

This strategy becomes important in order to exploit continuum mechanics formulation to describe and characterize the patterns in different types of tissues and domains and in different types of images. However, the continuous motion assumption does not hold when the behavior is not collective for the scales considered, and therefore, the mechanical interactions are better described by a network with topological changes instead than by a continuous motion. The continuous motion serves to describe large-scale cell movements approximated as a flow, as well as to describe the behavior of soft embryonic tissues as a continuum. The framework unifies both descriptions by calculating two elements: a differentiable displacements field $\mathbf{v_{cont}}$ and a trajectory field consistent with the local displacements $Trajs$. The spatio-temporal continuity implies also the smoothness of the trajectories. This is assumed for the data used in this work because the instantaneous deformation is considered infinitesimal for the time step of the acquisition. Therefore, the trajectories resulting by integrating

this field can be considered smooth.

These two elements enable the dual representation of the embryo dynamics from the Eulerian (spatial points seen from an external reference frame) and Lagrangian (particles describing trajectories as an internal reference frame) perspectives. However, as the different spatial points considered will be the instantaneous positions of the particles along their their trajectories, the framework proposed can be understood as a trajectory based (Lagrangian) representation of the dynamics which can be analyzed instantaneously or through time.

The displacements in $\mathbf{v_{cont}}$ must match a local differentiability condition (at each sample) to enable tensorial analysis. The displacements field can be sparse if calculated with a discrete image processing technique or a dense field if calculated with a continuous image processing technique. To fulfill the differentiability condition, the density of the field will define the spatial resolution of the description given at each sample. The trajectory field $Trajs$, defines the motion of the particles through time as determined by the displacements field (pathlines). Therefore, these trajectories enable the Lagrangian representation of the motion, either as the particles of a flow or as material points within a body or tissue.

Now, we introduce two different implementations of the model, one based on a discrete approximation to motion estimation (cell tracking) and another approach based on a continuous motion estimation technique (B-splines sequential registration). We will overview how both approaches can be used to provide the continuous motion description proposed.

3.2 Motion estimation based on cell tracking

In the last few years, bioimage processing has focused on developing cell tracking methods, mainly encouraged by the availability of high-resolution images of fluorescence-marked cell nuclei. Although none of them achieves a 100% correct cell lineage through different stages of development, most of them provide a high accuracy rate to obtain cell trajectories [Amat et al., 2014, Maška et al., 2014, Meijering et al., 2012], and therefore they can be exploited to implement the model proposed. Although several contributions have been made on cell tracking during the development of this PhD Thesis [Luengo-Oroz et al., 2012, Pastor-Escuredo et al., 2012, Pastor et al., 2009], the main contributions of our work are not linked to describe in detail an implementation of cell tracking but on techniques to use any cell tracking data to analyze embryogenesis dynamics.

Cell tracking, which is a discrete approach to estimate motion, provides a sparse map of samples map of samples. Typically an algorithm starts by nuclei detection followed by nuclei linking between consecutive steps. Most general method consists in selecting the closest nucleus in the next step, however, different approaches have been implemented to ensure robust linking. Through the linking, cell lineages are built but they propagate the error rate of the tracking building the trajectories. We

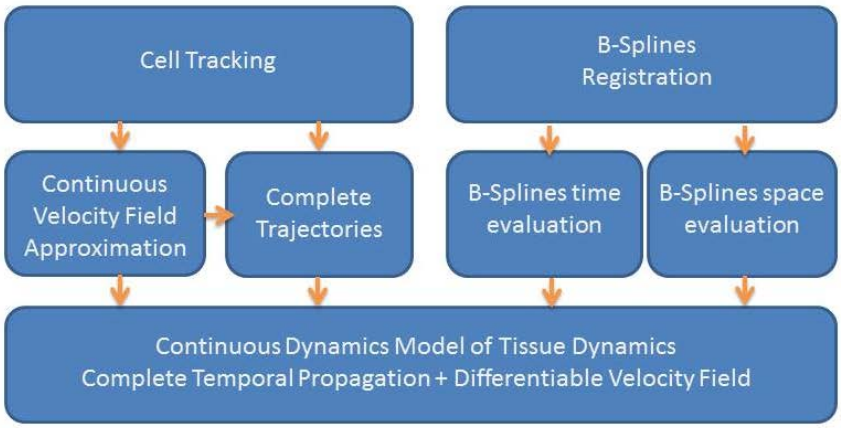

Figure 3.1: Scheme of the estimation of continuous motion with discrete analysis (cell tracking) and continuous analysis (B-Splines sequential registration).

will use the displacements implicit in the cell lineage to generate the differentiable vector field $\mathbf{v_{cont}}$ which integrates the displacements of a cell and its neighbors in a regularization process. Trajectories are built again using the differentiable vector field generating a continuous approximation of the cell lineage. This trajectory field is complete and defines a bijective map along the embryo development, so it can be considered as a flow assimilation of the lineage. Under the assumption of continuous motion, some phenomena like cell mitosis and cell apoptosis are disregarded as neglectable singularities for the description.

3.2.1 Digital cell lineage

A digital cell lineage is a spatio-temporal structure of the embryo comprising the information of cell nuclei position and also cell mitosis. It has been a major objective in *in-vivo* analysis of embryogenesis to create whole-embryo complete lineages. Thanks to the lineage it would be possible to understand the role of cell-level phenomena such as the proliferation or the organization of the fate maps (map of cells along stages of development according to their differentiation fate). However, only after tedious hand correction it is possible to ensure the accuracy of lineages for large embryos during long intervals

of time.

In the lineage, each cell is located spatio-temporally and uniquely identified with a cell identifier. Cell position is linked to the cell lineage by a reference to the mother cell allowing cell mitosis representation. We generally define each entry of a digital cell lineage with the following structure:

$$\{cellid, motherid, x, y, z, t\}_i \tag{3.1}$$

where i is each of the detected cells, $cellid$ is its corresponding unique identifier for the (x, y, z, t) spatio-temporal position and $motherid$ is the $cellid$ of the mother cell. Two cells with the similar mother cell describe a cell mitosis. Thus, the sparse map of samples is formed by all nuclei centers detected at each time $\mathbf{x_i}\,(x, y, z, t)$ that, alternatively, can be defined as a function of the unique identifier of each cell $\mathbf{x_i}\,(cellid)$. Any tracking method providing as output a lineage structure like this, could be used to further follow with the proposed processing pipeline.

3.2.2 Displacements field implicit in the cell lineage

We build a displacements vector field $\mathbf{v}$ at each embryo sample $\mathbf{x_i}$ calculating the displacements using the $motherid$ information to find the cell(s) in the next time step linked to the current cell $\mathbf{x_i\prime}$. In presence of mitosis, two occurrences may be found, being selected the cell that minimizes the Euclidean norm of the displacement. Therefore, only a part of the cell lineage is considered and some links are disregarded. This simplification could introduce a strong bias if the concentration of mitosis was high, so a mass change component would become relevant and it could not be neglected. Thus, $\mathbf{v}\,(\mathbf{x_i})$ is extracted from the displacement between the current position $\mathbf{x_i}$ and the following position $\mathbf{x_i\prime}$ when a link is available, which is not ensured if the lineage is not complete.

3.2.3 Temporal averaging of displacements

A temporal averaging process was introduced to filter out high-frequency noise within a trajectory (fast displacements changes of magnitude or direction within a trajectory). This noise may come from time-linking errors or high-temporal resolution phenomena such as mitosis that we disregard in a continuous analysis approach. We exploit the temporal information of the cell trajectories from the tracking to filter the velocity field $\mathbf{v}$ with a temporal Gaussian Kernel $N(0, T)$ centered on each sample within the trajectory. For each sample of the tracking data $\mathbf{x_i}$ within a branch k at a time frame t, being $\mathbf{v_k}$ the velocity of the same cell along the branch k, we define the temporal averaging as follows:

$$\mathbf{v_T}(\mathbf{x_i}) = \frac{1}{\alpha_i} \sum_{t\prime \in \pi(t,T)} w(i, t\prime)\mathbf{v_k}(t + t\prime) \tag{3.2}$$

where $t\prime$ is the index within a time window $\pi\,(t, T)$ centered on t, α_i is the sum of all weights $w\,(i, t\prime)$ for the links of the trajectory that the instance at $\mathbf{x_i}$ belongs to, following this expression:

$$w(i, t\prime\,) = e^{\frac{-t^2}{2T^2}} \text{ if the link at } t\prime \text{ exists}$$

$$w(i, t\prime\,) = 0 \text{ if the link at } t\prime \text{ does not exist or is marked incorrect}$$

In a discrete time domain, the ensemble for averaging π is defined as follows:

$$\pi(t, T) = \{t + h\Delta t \mid h \in \mathbb{Z},\ h\Delta t \in [-2T, 2T]\} \tag{3.3}$$

This filtering depends on the parameter T_{ave} which defines the Gaussian distribution parameter $T_{ave} = 2\sigma = 2T$, tuned considering the time step between acquisitions and covering the time necessary to mask cell mitosis (see Fig. 3.2). Some other parameters used are the $MaxMov$, that defines the maximum speed allowed for a tracking link, and the $MinWindow$ that defines the minimum number of steps to be averaged around each sample.

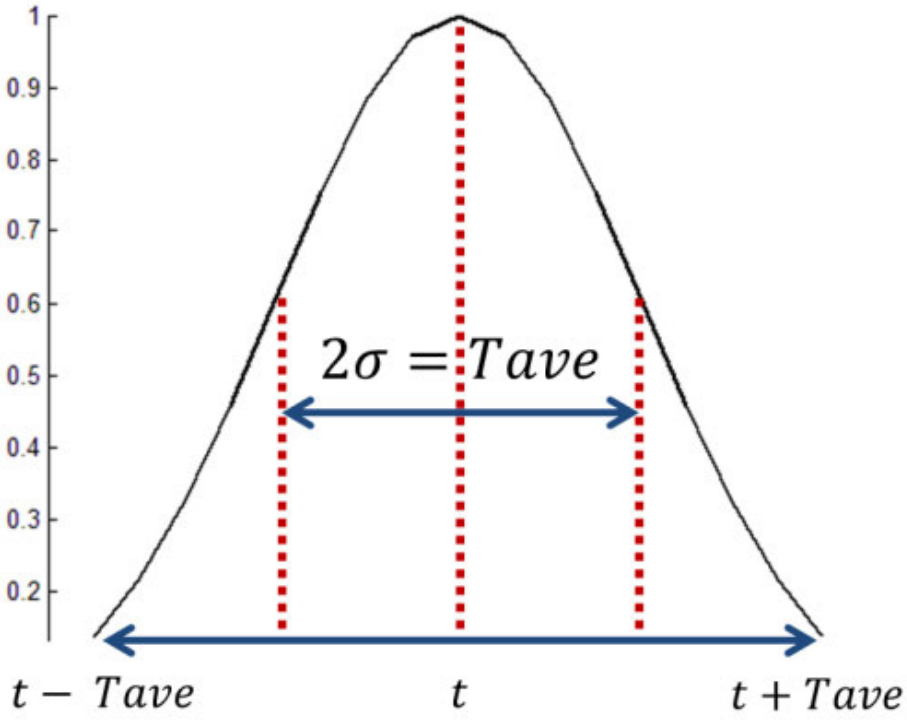

Figure 3.2: Schema of the Gaussian kernel parameters used for the temporal averaging of the velocity field.

3.2.4 Obtaining a differentiable displacements field

The vector field that describes the continuous motion is obtained by the regularization of the velocity field $\mathbf{v_T}$, using a kernel $N(0, R)$ adjusted to generate a differentiable vector field estimated around each sample $\mathbf{x_i}$. The interpolated field $\mathbf{v_{TR}}(\mathbf{x_i})$ is calculated for every embryo sample i in a time frame t as

$$\mathbf{v_{TR}}(\mathbf{x_i}) = \frac{1}{\beta_i} \sum_{m \in \eta(i,R)} w_{i,m}(\mathbf{x_m}) \mathbf{v_T}(\mathbf{x_i}) \tag{3.4}$$

where $\eta(i, R)$ is the set of selected neighbors for each sample, $w_{i,m}$ are the weights following the by $N(0, R)$ distribution centered in $\mathbf{x_i}$ being $\mathbf{x_m}$ the position of each neighbor and β_i the sum of all the weights. In order to preserve sharp dynamic boundaries that are treated as discontinuities inside the field, we use a binary function $S(\mathbf{x_m}, \mathbf{x_i})$ that determines if a sample $\mathbf{x_m}$ should be considered within the ensemble average of the sample $\mathbf{x_i}$ to be averaged.

$$\eta\,(i, R) = \{m \mid \|\mathbf{x_m} - \mathbf{x_i}\| < 2R, S(\mathbf{x_m}, \mathbf{x_i}) = 1\} \tag{3.5}$$

where $S(\mathbf{x_m}, \mathbf{x_i})$ considers three decision thresholds which are set based on experimental data observation:

- Maximum angle deviation of $\mathbf{x_m}$ against the reference $\mathbf{x_i}$
- Minimum speed module of $\mathbf{x_m}$
- Maximum speed module ratio of $\mathbf{x_m}$ against the reference $\mathbf{x_i}$

The parameter that defines the spatial scale is $X_{ave} = 2R = 2\sigma$ and is optimized using regularization based on discretized function to statistically measure the differentiability of the velocity field for a range of values. The parameter X_{ave} is selected using a regularization based on the second-order structure function for a velocity function *v* is generally defined as follows:

$$S_2\,(l) = \left\langle [v(r + l) - v(r)]^2 \right\rangle \tag{3.6}$$

where $< \langle \rangle$ stands for the ensemble average and $S_2(l) \approx l^2$ when $l \to 0$.

In our discretized and non-homogeneously sampled vector field, we perform an approximation using a power law fitting on a series of bins n to approximate the structure function with the velocity difference modulus. Thus, the discrete vector field $\mathbf{v_{TR}}(\mathbf{x_i})$ will be approximately differentiable when the function $S_{2,i}\,[n]$ on the spatio-temporal position $\mathbf{x_i}$ fits a decay power law of exponent $e \approx 2$, pl_{-2}.

$$S_{2,i}\,[n] = \{\left\langle \|\mathbf{v_{TR}}(\mathbf{x_k}) - \mathbf{v_{TR}}(\mathbf{x_i})\|^2 \right\rangle\}_{\Gamma_{n,i}} \tag{3.7}$$

To obtain this function, firstly, a discretized space around each position is built:

$$\Gamma_{n,i} = \{r \mid (n-1)dl < \|\mathbf{x_k} - \mathbf{x_i}\| < (n+1)\} \tag{3.8}$$

where $n \in [1, numberOfBins]$ and $\{\mathbf{v_{TR}}(\mathbf{x_k})\}$ are the vector samples of the set of cells $k \in \Gamma_{n,i}$ enclosed inside each concentric ring of size dl around a reference position $\mathbf{x_i}$. The samples enclosed in this space are statistically characterized with several parameters shown in Fig. 3.1.

Once the second order function is created for every sample $\mathbf{x_i}$, an ensemble average along space $S_2(n,t)$ is created by aggregating by rings all the samples in one time step. To compute this function, a subset of rings within the whole space of $S_{2,i}[n]$ are selected by matching a stability condition. This condition imposes that the parameter $\sigma(Acells)$ (see Table 3.1) within the rings should be below the third quartile Q_3 of the distribution of this parameter for the ring n in every sample. Thus, rings with divergent vector directions are disregarded as they could contain velocity discontinuities.

Dcell = Distance To Closest Cell $(\boldsymbol{\mu}, \boldsymbol{\sigma})$	$\min\{\|\mathbf{x}_k - \mathbf{x}_r\| \mid \mathbf{x}_k, \mathbf{x}_r \in Nn\}$
Acells = Angle between closest Cells $(\boldsymbol{\mu}, \boldsymbol{\sigma})$	$\arccos(dot(\mathbf{v_r}, \mathbf{v_k})) \mid \mathbf{v_r}, \mathbf{v_k}$ *velocity samples at* $\mathbf{x_r}, \mathbf{x_k} \in Nn$ *and each pair belongs to Dcell*$\}$
Number of neighbors	$\sum Nn$
Density	$\frac{1}{Vn}\sum Nn$

Table 3.1: Statistical descriptors of the velocity field in a discretized space around each cell

Thus, we obtain a function that characterizes the average differentiability of the spatial deformation field along the time steps of the nuclei data. This function is used to test several $N(0,R)$ regularization kernels to obtain the minimum $X_{ave} = 2R$ that makes the deformation field fit in average to pl_{-2} along time. The output of the regularization described is a sparse vector field $\mathbf{v_{cont}}(\mathbf{x_i})$ that approximates the cell displacements as a differentiable field.

3.2.5 Trajectory field generation

We then build the trajectory field consistent with $\mathbf{v_{cont}}$ that defines a bijective mapping along an interval $[t_n, t_m]$ as a set of complete and unique trajectories $Trajs_n^m$. For motion characterized by long displacements from the initial position but under infinitesimal local gradients, the trajectory field is assumed to define continuous domains formed by smooth trajectories. Thus, the trajectories form a flow field that approximates the cell dynamics implicit in the cell lineage.

The trajectories $traj_j$ are built integrating the vector field $\mathbf{v_{cont}}(\mathbf{x_i})$ from an initial position $\mathbf{x_j}$ in t_n until t_m using the information located in the samples map $\mathbf{x_i}$ with a *nearest cell interpolation* of the velocity field $\mathbf{v_{cont}}$. The result is a trajectory field $Trajs_n^m = \{traj_1, \ldots, traj_l\}$ where l is the number of trajectories equal to the number of cells in t_n and where each $traj_j(x,y,z,t)$ is a set of

spatio-temporal points with the same $trajid_j$. Each spatio-temporal point of the trajectory has been assigned to the nearest cell in the map of points $\mathbf{x_i}$ allowing the interpolation of vectorial and tensorial data and also the visualization of Lagrangian descriptions expressed in terms of the trajectory field. Thus, these trajectory field enables the Lagrangian expression of the dynamics and derived descriptors in terms of trajectories $\mathbf{v_{cont}}(Trajs)$.

3.3 Motion estimation based on B-splines sequential registration

Continuum deformation can be also estimated more directly with other image processing techniques such as PIV or registration [Keane and Adrian, 1992, Sorzano et al., 2005]. These techniques are preferred to cell tracking when the latter is difficult to achieve due to particle density, image quality or spatio-temporal resolution. These methods rely either on image correlation or on other intensity based metrics [Thévenaz and Unser, 2000]. We rely on an implementation based on B-splines registration which provides a continuous deformation field expressed in terms of continuous functions (B-splines) which ensure the spatial differentiability of the deformation field and is efficient for further analytical treatment [Kybic and Unser, 2003, Ledesma-Carbayo et al., 2005, 2006]. Thus, as shown in Fig.3.1, we estimated a dense version of $\mathbf{v_{cont}}$ expressed through the B-splines and a trajectory field $Trajs$ as the tracking of material points (initial seeds) evaluating the B-splines.

3.3.1 B-splines registration

Among the different techniques that work at the image level rather than the cell or particle level, we preferred the B-splines registration for the following reasons:

- Accurate deformation fields can be expressed with high-order B-splines as continuous functions
- Global optimization of image comparison metrics that avoid boundary effects
- Continuous function properties for derivation and deformation evaluation

Registration definition

Given two N dimensional discrete images $f_r(\mathbf{x})$ and $f_t(\mathbf{x})$ where $\mathbf{x} \equiv (x_1, x_2, ...x_n) \in \mathbf{I}$ being $\mathbf{I}$ the N dimensional discrete interval representing the set of all pixels coordinates in the image. We will refer to them as the *reference* image f_r and *test* or transformed image f_t, respectively. Supposing that the test image is a geometrically transformed version of the reference image and vice-versa. This is to say that the points with the same coordinates in the reference image $f_r(\mathbf{x})$ and in the correctly transformed test image $f_w(\mathbf{x}) = f_t^c(\mathbf{g}(\mathbf{x}))$ should correspond.

Where f_t^c is a continuous version of the test image. The aim of the registration procedure will be to find the deformation function $\mathbf{g} : \mathbb{R}^n \rightarrow \mathbb{R}^n$ ($n = 3$ for the case of our three dimensional images) that minimizes a given criterion trying to provide a f_w as close as possible to f_r. Therefore, we define the registration problem as a minimization problem that searches for a deformation function $\mathbf{g}$ such that $\mathbf{g} = \arg\min_{\mathbf{g}\in G} E(f_r, f_t^c(\mathbf{g}(\mathbf{x})))$ where G is the space of all admissible transformation functions $\mathbf{g}$ and E is the criterion being minimized.

Following sections give details of different characteristics of the proposed method, regarding the image model, the transformation model, and the criterion function.

Image model

We generate a continuous version f_t^c of the discrete test image f_t using uniform B-splines as interpolation functions:

$$f_t^c(\mathbf{x}) = \sum_{\mathbf{i}\in I} b_{\mathbf{i}} \beta_q(\mathbf{x} - \mathbf{i}) \tag{3.9}$$

where $\beta_q(\mathbf{x})$ is the tensorial product of centered B-splines of degree q. This interpolation provides a good approximation and a good framework for the evaluation of spatial derivatives analytically.

Transformation model

Given that $\mathbf{g} : \mathbb{R}^n \rightarrow \mathbb{R}^n$ represents the transformation function, we will restrict its representation to a family of functions described by a finite number of parameters $\mathbf{c}$ using also in this case B-spline functions.

$$\mathbf{g}(\mathbf{x}) = \sum_{\mathbf{j}\in\mathbb{Z}^N} \mathbf{c}_{\mathbf{j}} \beta_r(\mathbf{x}/\mathbf{h} - \mathbf{j}) \tag{3.10}$$

Therefore $\mathbf{g}$ is a linear combination of base functions $\beta_r(\mathbf{x})$ located on a regular grid. The parameter $\mathbf{h}$ represents the knot spacing of that regular grid, and therefore governs the scale of the transformation, the total number of parameters $\mathbf{c}_{\mathbf{j}}$, and the smoothness of the solution. The advantage of this deformation model are its good approximation properties, its fast evaluation, the local influence of the parameters, and its implicit smoothness.

A remarkable feature of the B-spline model is that the complexity of evaluating the deformation, and the gradient and the Hessian of the criterion does not depend on the sampling step $\mathbf{h}$, or equivalently, on the number of parameters. This can be seen from the fact that one pixel in the image always contributes to a fixed number of gradient (or Hessian) components. Additionally the explicit formulation of the deformation functions allows express explicitly the derivatives of the criterion [Kybic and

Unser, 2003, Thévenaz et al., 1998, Thévenaz and Unser, 2000] with respect to the parameters within the optimization procedure performed during the registration. Additionally transformation descriptors, such as the deformation gradient tensor, can be easily computed explicitly from the described transformation model.

Criterion

The criterion to be minimized is composed of two terms, a similarity or data term E_d and a regularization term E_r as described in the following equation.

$$E = E_d(f_r, f_t(\mathbf{g})) + \alpha E_r(\mathbf{g}) \tag{3.11}$$

As data term or similarity criterion we choose the Sum of Squared Differences -SSD- criterion because of its simplicity, fast computation time, and smoothness of the resulting criterion space. It is described by:

$$E_d = \sum_{\mathbf{i}\in I}(f_w(\mathbf{i}) - f_r(\mathbf{i}))^2 = \sum_{\mathbf{i}\in I}(f_t(\mathbf{i} + \mathbf{g}(\mathbf{i})) - f_r(\mathbf{i}))^2 \tag{3.12}$$

where $\mathbf{I}$ is the set of coordinates specifying the spatial region of interest, and N_I is the corresponding number of pixels.

Additionally to enforce smoothness of the transformation and to improve the stability of the solution in homogeneous areas, our non-rigid registration approach employs a regularization based on the separate norms of the second derivative of each of the deformation components [Rohlfing et al., 2003, Wollny et al., 2010] as energy term E_r in (3.11):

$$E(\mathbf{g}) := \int_\Omega \sum_i^d \sum_j^d \left\| \frac{\partial^2}{\partial x_i \partial x_j} \mathbf{g}((x)) \right\|^2 d(x). \tag{3.13}$$

As given in eq. (3.11) the regularization term will be weighted against the similarity measure by a factor κ.

3.3.2 Spatial and material definition of the continuous motion from B-splines registration

The spatial deformation along time given by $\mathbf{g_t}$ is expressed as a sequence of continuous transformation functions $\{\mathbf{g}\}$ for each pair of images, so it is considered to be a dense characterization of spatial tissue dynamics. In order to have a definition of $\mathbf{v_{cont}}$ in terms of spatial points, we define a differentiable discretized vector field $\mathbf{v_{reg}}$ using a grid of samples $\mathbf{x_{grid}}$ to evaluate the B-splines $\mathbf{g_t}$ and to obtain the instantaneous displacements between time steps. This grid can be adjusted to have

a specific density (parameter $snode$, that could be set as dense as the image pixel grid at the expense of more computational cost) and to be properly restricted to the tissue boundaries by masking the grid with the tissue contour of each time step to have $\mathbf{x_i} = \mathbf{x_{grid}}(t)$.

$$\mathbf{v_{reg}}(\mathbf{x_i}) = \mathbf{g_t}(\mathbf{x_{grid}}(t)) \tag{3.14}$$

The Lagrangian characterization of the system based on the material points can be also obtained by evaluating the B-splines in an interval $[t_n, t_m]$ as a spatio-temporal map generated from the grid in t_n. This new map stands for the positions within the trajectories followed by material points at each time point. These trajectories can be created by evaluating $\mathbf{g_t}$ to update the position in each time step from the seeds in the grid j in t_n.

$$\mathbf{x_{t,j}} = \mathbf{x_{t-1,j}} + \mathbf{g_t}(\mathbf{x_{t-1,j}}) \ , \ \mathbf{x_{t_n,j}} = \mathbf{x_{grid,j}(t_n)} \text{ where } t \in [t_{n+1}, t_m] \tag{3.15}$$

This expression determines the direction of the registration sequence $\mathbf{g_t}$ and the subsequent motion estimation. The registration has to be applied inversely to the direction of the displacement field expected. Thus, given spatio-temporal image data between two time points $[t_{ini}\, t_{end}]$, the causal displacements field is achieved by registering the sequence backwards $t_{end} \rightarrow t_{ini}$. Therefore, the anticausal displacements field is calculated by a forward registration $t_{ini} \rightarrow t_{end}$.

This way of evaluating the B-splines provides a trajectory field $\{\, Trajs_n^m \}_j$ that is smooth when the spatio-temporal continuity of the transformation is ensured with special regularization or constraints. Sequential registration provides incremental differentiable spatial deformation fields but does not ensure the smoothness of the trajectories [Ledesma-Carbayo et al., 2006]. However, as mentioned earlier on, the temporal resolution is assumed to provide infinitesimal deformation. In this situation, it can be also assumed that the trajectories of the material points will be smooth along the sequence of deformation displacements fields. Thus, B-splines sequential registration is used to create a dense Lagrangian description of the dynamics $\mathbf{v_{reg}}(\, Trajs_n^m)$.

3.4 Conclusions

In this chapter we presented a comprehensive framework to estimate motion from *in-vivo* images that provided a description of continuous motion in terms of the trajectories of material points moving within a continuum, whose deformation was spatially characterized with a differentiable displacements field. The framework included a pipeline to provide such a description from a digital cell lineage (as a result of cell tracking) and another pipeline based on B-splines sequential registration.

Both approaches of motion analysis (see Fig.3.3) were illustrated as the selection of their usage depended on the image features and the scale of motion to be analyzed (see discussion in Chapter 7). The lineage based approach required techniques to deal with sparse data containing displacements without prior differentiability conditions. The registration pipeline was more demanding in terms of image quality in resolution to provide a good motion estimation, but it provided a finer characterization in terms of continuous functions itself.

We expect that with the increasing quality of images, these techniques could be applied to numerous biological studies. There are unavoidable limitations coming from the scale of the dynamics to be observed. The methods can only be applied when collective behavior or large-scale motion produces quasi-continuous motion. The methods will not be suitable to describe network-like rearrangements in very small scales, where discrete analysis tools (and also discrete mechanics formulation) should be used instead.

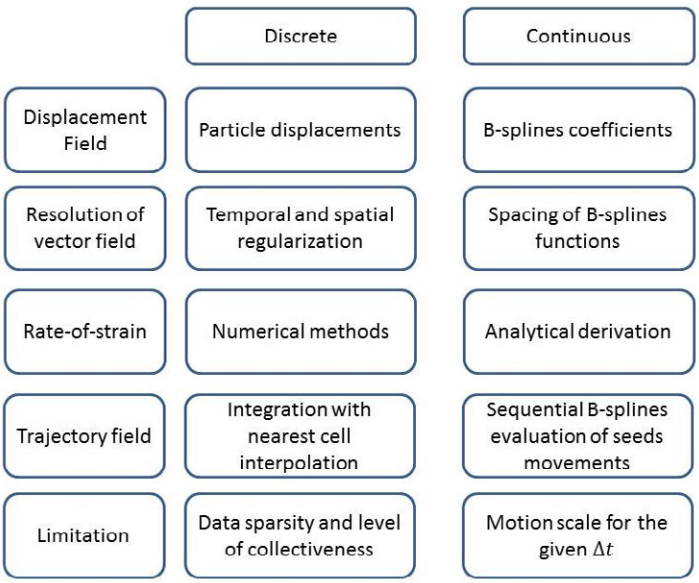

Figure 3.3: Continuous vs discrete analysis at the different stages of analysis. Analysis can be equivalent for specific data and can be combined throughout the processing pipeline depending on the data sources.

Chapter 4

Descriptive framework of embryogenesis mechanics

We propose a spatio-temporal framework that quantifies embryogenesis mechanics using multi-scale deformation and strain (kinematics) descriptors [1] to profile the history of deformation undergone by cell domains and tissues along stages of the development. This descriptive framework relies on the motion estimation framework introduced in chapter 3, which can be applied to flow-like movements or the motion of soft-tissues during embryogenesis.

This framework, as anticipated in section 1.2, is based on a Lagrangian representation of the dynamics, which has not been exploited in embryogenesis analysis so far. This representation will allow us to quantify instantaneous mechanical descriptors, in $2D$ and $3D$, equivalent to current works in the field based on an Eulerian description of deformation (see Appendix A.2 for details), but also to consistently explore other temporal length-scales with finite time descriptors. Patterns emerging from instantaneous descriptors show mechanical events as a result of cell intrinsic activity and cell interactions at a certain moment (instantaneous resolution assumption). On the other hand, the patterns emerging from finite-time descriptors indicate the history of mechanical activity providing insight about the organization of mechanical activity through time.

In this chapter we describe the different components of the analysis that will be applied to the studies of zebrafish and Drosophila embryogenesis. Figure 4.1 shows the schema of the representation and descriptors for zebrafish and its digital cell lineage. Spatial maps and material (Lagrangian) profiles are tools to observe patterns from different perspectives and further quantify and understand the mechanics of development.

[1] As mentioned in the Introduction, we will generalize the term to mechanical descriptors.

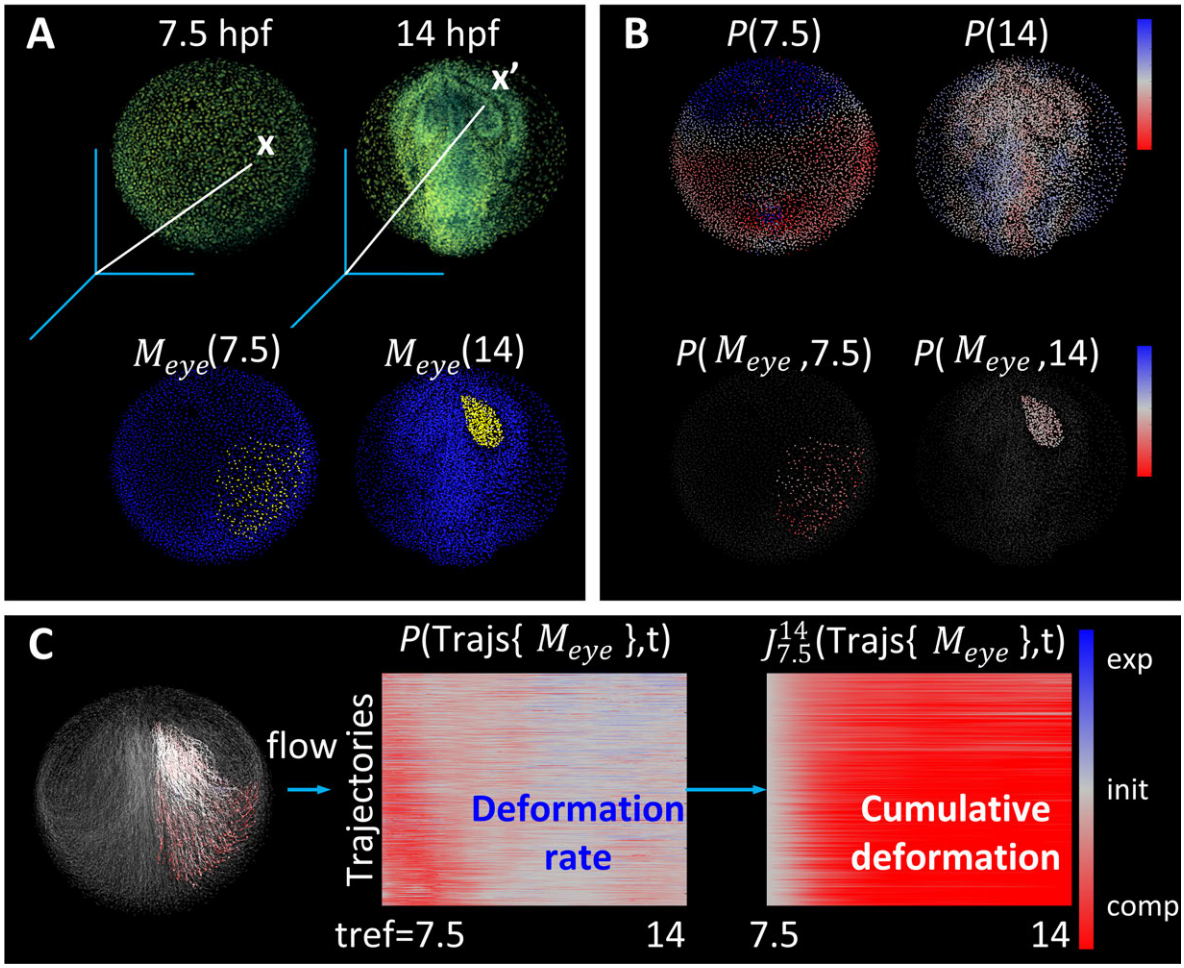

Figure 4.1: **A**: Top: Render of raw nuclei data acquired with fluorescent in-vivo microscopy for a wild-type zebrafish embryo. The orientation is from the animal pole at two stages of development: 7.5 hours post fertilization -hpf- (past half epiboly) and 14 hpf (segmentation stage). Bottom: Two snapshots of the digital embryo reconstructed from the raw data shown above. Nuclei are detected with image processing techniques forming a spatio-temporal map $\mathbf{x_i}$ as digital sampled embryo. Samples are linked through time with a tracking method forming a cell lineage. The cell selection defining the eye domain M_{eye} is shown for both stages highlighted in yellow over the rest of the embryo samples.
B: Top: The Eulerian descriptor P. This descriptor gives instantaneous information about the compression (red) and expansion (blue) rates. The patterns in this descriptor show organization in the instantaneous activity in the embryo. Bottom: The descriptor P is presented only for the eye domain M_{eye}. The definition of Eulerian descriptors in terms of the embryo samples $\mathbf{x_i}$ allows the aggregation of descriptor by cell domains.
C: Left: The descriptor P seen along the cell trajectories of the eye domain M_{eye}. The continuous trajectories definition for the computation of cumulative descriptors and a complete trajectory based representation (Lagrangian) of the descriptors as domain profiles abstracted from spatial coordinates. The profiles shown for volume change rate P and the cumulative volume change for the interval $J^{14}_{7.5}$ represent the Lagrangian dynamics of the eye field (rows: trajectories, columns: time steps). The descriptor J shows compression (red) to expansion (blue) from the initial state at reference time ($t_{ref} = 7.5$ hpf here).

4.1 Motion to deformation: Incremental Deformation Gradient (IDG) tensor

Due to the nature of data acquired with *in-vivo* imaging, the deformation information is based on spatial displacements characterized by $\mathbf{v_{cont}}(\mathbf{x_i})$. In order to study deformation patterns, it is necessary to first define the Incremental Deformation Gradient -IDG- $\mathbf{f_t}(\mathbf{x_i})$ tensor field for both approaches introduced in the previous chapter. Having defined this information for the spatio-temporal map implicit in the trajectory field $Trajs$, it would be possible to either present the spatial snapshots as an Eulerian description of the mechanical activity or provide a Lagrangian description through the trajectory of the particles. This way, the tensor data $\mathbf{f_t}$ is organized along the trajectories so it can be processed to generate cumulative mechanical activity profiles in finite temporal length-scales.

4.1.1 IDG tensor from tracking based motion estimation

The differentiable velocity field obtained through the regularization of the tracking data $\mathbf{v_{TR}}(\mathbf{x_i})$ is used to obtain the IDG tensor field $\mathbf{f_t}(\mathbf{x_i})$, that represents the local spatial variations of the dynamic system between two consecutive time steps ($t \rightarrow t + \Delta t$) for all the samples $\mathbf{x_i}$. The displacements field defined by this method is sparse, so the tensor has to be computed using a numerical approximation of the tensor with discrete elements to calculate the partial derivatives in each spatial dimension. Therefore, the IDG tensor $\mathbf{f_t}$ at the sample in the position $\mathbf{x_t}$ at time t is defined as the mapping from the material vector $\mathbf{dx_t}$ onto the spatial vector $\mathbf{dx_{t+1}}$ (see A.1):

$$d\mathbf{x_{t+1}} = \mathbf{f_t} d\mathbf{x_t} \tag{4.1}$$

For a discrete vector field, we define $\mathbf{dx_t}$ and $\mathbf{dx_{t+1}}$ as follows:

$$d\mathbf{x_t} = [\mathbf{x_l} - \mathbf{x_t}] \, \forall \mathbf{x_l} \in N_D(\mathbf{x_t})$$

$$d\mathbf{x_{t+1}} = [\mathbf{x_l} - \mathbf{x_{t+1}}] \, \forall \mathbf{x_l} \in N_D(\mathbf{x_{t+1}})$$

$$N_D(\mathbf{x_{ref}}) = \{l \, | \, \|\mathbf{x_l} - \mathbf{x_{ref}}\| < G, S(\mathbf{v_l}, \mathbf{v_{ref}}) = 1\}$$

where $G = X_{ave}$ is the diameter of the differentiable domain interpolated and regularized as described in the previous chapter and discarding the samples with the similarity function $S(\mathbf{x_l}, \mathbf{x_{ref}})$ used in the velocity field regularization (see section 3.2.4). The discrete numerical problem is solved using a least squares approximation to get the Incremental Deformation Gradient -IDG- $\mathbf{f_t}$. We solve this numerical problem writing the terms of the expression 4.1 as matrices and using a least squares

approximation to get $\mathbf{f_t}$ minimizing the error $\mathbf{M_f}$ in the gradient calculation for the non-homogeneous deformation field. The IDG tensor fied is created by applying this expression to all samples $\mathbf{x_i}$.

$$\mathbf{f_t} = \mathbf{dx_{t+1}} \mathbf{dx_t}^t (\mathbf{dx_t}^t \mathbf{dx_t})^{-1} \tag{4.2}$$

4.1.2 IDG tensor from B-splines registration based motion estimation

The IDG tensor can be also evaluated for the samples of the spatial points defined by $Trajs_j$ obtained by the B-splines sequential registration (section 3.3.2), $\mathbf{x_i}$, by directly calculating the partial derivatives from the continuous functions B-splines that define the dense deformation field $\mathbf{g_t}$. Alternatively, we could use the vector field definition $\mathbf{v_{reg}}(\mathbf{x_i})$, but it would require numerical methods that would introduce some error of approximation and would be more computationally expensive. However, the analytical differentiation of the B-splines is a more accurate and fast way to calculate the IDG tensor. Thus, the $\mathbf{f_t}(\mathbf{x_i})$ for each sample in each time step can be obtained as:

$$\mathbf{f_t}(\mathbf{x_i}) = \nabla_x \mathbf{g_t}(\mathbf{x_i}) + \mathbf{I} \tag{4.3}$$

being $\mathbf{I}$ the identity tensor as $\nabla_x \mathbf{g_t}$ represents the Incremental Gradient of Displacements -IGD- as we will see in the next section. The quantification of this gradient is based in the analytical derivation of the B-splines series forming $\mathbf{g_t}$ (section 3.3.1) for each selected point of evaluation $\mathbf{x_i}$.

4.1.3 Spatial and temporal scales of the IDG tensor for each motion estimation method

The IDG tensor field is the basic deformation information used to build the descriptors framework. This tensor provides the local characterization of the deformation and strain rates at each reference position of the field. The temporal scale depends on the time resolution of the image sequence which imposes a limit in the resolution. We assume that the imaging has been performed to observe the dynamics instantaneously, so we will consider that each incremental time step is instantaneous for the used data. Thus, the IDG represents the deformation and strain rates and infinitesimal deformation descriptors will be used. The spatial scale of the deformation measure depends on the method of analysis used:

- For the cell tracking based estimation, the descriptors integrate information of the cell and its neighbors (number of neighbors depends on the information required during the regularization process to obtain a differentiable vector field) to calculate the gradients, so the characterization of the patterns is already mesoscopic, minimally at the cell domain level. The interpretation of the descriptors will be done in terms of the relative position of the nuclei around the reference sample between two time steps.

- For the motion estimation based on the B-splines sequential registration, the resolution is given by the separation between B-splines nodes ($cnode$ parameter) and the properties and order of the B-splines functions. Generally, the scale of the description provided by a B-splines field is smaller than the $cnode$ value. This means that one node per cell would offer a subcellular resolution of the description. Using more that one node by cell would provide a very detailed resolution of the deformation in subcellular regions.

4.2 Instantaneous deformation description

The system can be seen as snapshots of the state of several processes at a given time point. In this case, we simply create descriptors derived from the IDG tensor to generate spatial maps with the instantaneous deformation descriptors (assumed high temporal resolution of observation). We use invariants of tensors derived from IDG, independent of orientation and velocity of the reference frame to obtain meaningful and comparable descriptor fields $E(\mathbf{x_i})$. The family of invariants summarized in Table 4.1 comprises local topology descriptors and different types of strain rates. The descriptor maps generated are well suited to describe the emergent behavior of collective interactions that generate patterns between the cell domain and the whole embryo scales (mesoscopic scales), even crossing recognizable tissues. The existence of emergent patterns warranties the suitability of the continuous analysis approximation at least for some stages of development where mechanical activity organizes in scales beyond the scale of analysis as defined in the previous section.

4.2.1 Deformation topology and strain rate descriptors

From the IDG and the derived tensor Incremental Gradient of Displacements -IGD- tensor field $\mathbf{h_t}(\mathbf{x_i}) = \mathbf{f_t}(\mathbf{x_i}) - \mathbf{I}$ we obtain the instantaneous deformation and strain descriptors (see Table 4.1). We can study the topology of the deformation of the displacements field inspired in flow topology analysis (see A.3.1). This description includes the expansion and compression rate P and the rotation descriptors D and Q. Moreover, P and D can be combined into the $Topology$ descriptor. The strain rate descriptors are obtained from the symmetric tensor $\boldsymbol{\varepsilon}$ (see A.3.1). However, this tensor do not differentiate the elongations from the shears, so we use the deviatoric tensor $\mathbf{d}$ to characterize the shears in the displacements field isolated from the elongations [Blanchard et al., 2009, Bosveld et al., 2012].

4.2.2 Biological interpretation of instantaneous descriptors

Given the considerations of the scales presented in section 4.1.3, it is possible to give a biological interpretation to the previous descriptors:

P	Volume Change Rate $P>0$ Expansion $P<0$ Compression	Expansion and Compression of the tissue (changes in cell sizes)
D	*Rotation Discriminant* Rotation vs Elongation >0 Rotation <0 No Rotation	Quantitative measurement of the amount of rotation compared to linear deformation
Topology	*P* and *Rotation* 1 Expansion and Rotation 2 Expansion and No Rotation 3 Compression and Rotation 4 Compression and No Rotation	By crossing P and the Rotation Discriminant, the main topological configurations can be classified
Q_d	Incremental Distortion.	Distortion of the tissue that does not produce tissue volume changes (cell shape and cell intercalation changes)
$\{e_i\}$	Incremental strain components	Magnitude and geometry of local deformation changes
$\{de_i\}$	Incremental distortion components	Magnitude and geometry of local volume changes

Table 4.1: Eulerian descriptors:
The Eulerian descriptors are the quantitative aspects of the embryo dynamics seen from a spatial reference frame, or in other terms, as the relative spatial variations of the displacements. As the description is generated from a cell tracking, the descriptors quantitatively describe the relative changes in the nuclei position topology between consecutive time steps.

- P: The compression/expansion rate expresses the changes in the size (area $2D$ or volume $3D$) in the region surrounding the sample. This descriptor involves an incremental change in the continuum size within the scale of the IDG tensor that can be confined to one cell (B-splines with $cnode <$ cell size) or several cells (tracking based method).

- D: Rotation discriminant expresses how the continuum rotates in comparison with linear strain rates. This descriptor does not provide much information in very local scales, but it can be used to highlight vortexes and rotation centers described by cells along their movement in the tracking based approach.

- Q: Second invariant of $\mathbf{h}$. This descriptor provides similar information to D but it does not isolate the P component, so D is better suited to quantify the amount of rotation.

- $Topology$: This descriptor combines the signs of P and D, so it is possible to classify the regions of the tissue with both rotation and expansion/compression behavior properly.

- Q_s: Second invariant of $\boldsymbol{\varepsilon}$ provides information of the amount of strain after removing the rotation component. However, it does not isolate the P behavior, so it quantifies both shears and compression/expansion. This descriptor, used in non-compressible fluids is disregarded here.

- e_i: Principal components of $\boldsymbol{\varepsilon}$ show elongations (positive-blue) and shrinking (negative-red) strain rates and their directions. This is a geometrical characterization of the strain rate useful in $2D$ but too complex for $3D$. Therefore, principal invariants are preferred as they provide the information as scalar fields.

- Q_d: Second invariant of $\mathbf{d}$ provides information of the amount of strain after removing the rotation component and P. This descriptor is therefore, very important because it isolates the tissue distortion. In cell domain scales, this descriptor provides information about tissue rearrangements that can be produced by smooth cell intercalation (fast and sharp intercalation is not a continuous motion) or cell shape changes. In small scales (small $cnode$) this descriptor describes shear deformation of the cell shape. The tensor $\mathbf{d}$ has been previously used to measure this tissue behavior [Blanchard et al., 2009, Bosveld et al., 2012], but using the principal components instead of this invariant that is defined here inspired in the invariant Q_s used in non-compressible flows.

- $\mathbf{w}$: The angular velocity derived from the skew-symmetric tensor $\boldsymbol{\Omega}$ has been used to describe rotation, but the usage of Q and D is preferred here to quantify rotation rates.

For the shake of simplicity, we have selected P, D and Q_d to generally describe instantaneous behaviour in $3D$ data as they capture the main behaviors in an isolated way: compression/expansion, rotation and distortion. Additionally e_1, e_2 and geometrical projections of epsilon on anatomical axis are considered in $2D$ dimensions.

4.3 Finite-time deformation description

4.3.1 Finite-time Deformation Gradient ($FTDG$)

From the Langrangian perspective, $\mathbf{v_{cont}}(traj_j)$ enables for the characterization of the deformation history along each trajectory. The deformation for a finite-time interval $[t_n, t_m]$ can be quantified by the Finite Time Deformation Gradient -$FTDG$- $\mathbf{F_n^m}(traj_j)$. This tensor is built, as described in eq. 4.4 (see A.1 for details), applying the chain rule with the IDG tensors along each trajectory of $Trajs_n^m$. This is possible because the IDG tensor is expressed in terms of the spatial position of particles $\mathbf{x_i}$ for which we have built a consistent trajectory, so the instantaneous description is integrated within a Lagrangian representation of the motion.

$$\mathbf{F_n}^{\mathbf{m}}\{traj_1\} = \mathbf{f_{m-1}} \dots \mathbf{f_{n+1}} \mathbf{f_n} \tag{4.4}$$

where $\mathbf{f_n}$ is the IDG tensor between t_n and t_{n+1} for the trajectory $traj_1$ and so forth. Thus, the trajectory field allows us to calculate the $FTDG$ tensor which can be expressed at the initial estate at t_n or from the deformed estate at t_m.

4.3.2 Finite-time deformation and strain descriptors

From the tensor $\mathbf{F_n^m}$ it is possible to obtain the finite time deformation and strain descriptors. This deformation can be arbitrarily large for a time interval $[t_n, t_m]$, so the infinitesimal assumption used in the calculation of instantaneous descriptors does not apply. Instead, finite deformation expressions and the polar decomposition of mechanical contributions is used (see Appendix A.4.1). Using this decomposition we can extract the finite elongations $\mathbf{U}$ and the rotation $\mathbf{R}$ tensors. The finite strains are calculated by the *Cauchy-Green* strain tensors $\mathbf{C_n^m}$ and $\mathbf{B_n^m}$. In order to isolate the expansion and compression component of the deformation as we did with the deviatoric tensor for instantaneous deformation, the isochoric deformation tensor $\tilde{\mathbf{F}}\mathbf{_n^m}$ and its Cauchy-Green tensors are calculated. Again, principal components and invariants of these tensors are used to describe the mechanical behavior (see Table 4.2). These descriptors generalize the instantaneous deformation descriptors to quantify deformation in temporal intervals and we have designed a set of descriptors analogous to the previously presented for instantaneous deformation and strain. Technical details of the descriptors are provided in the Appendix A.4.1.

4.3.3 Biological interpretation of finite-time descriptors

- J: The compression/expansion expresses the changes in the size (area $2D$ or volume $3D$) between two different configurations between an interval of time. This descriptor shows the evolution of the size of the cells within the spatial scale of the descriptor (see section 4.1.3) along time given an initial state.

- $MIC1$: First distortion descriptor. This descriptor contains information about the tissue distortion that linearly increments with the amount of shears. This descriptor quantifies the distortion of the tissue between any two time points, so it allows to map how a cell domain can deform or intercalate during long intervals of time. The limitation of the intercalation is that the trajectories cannot cross (smoothness of trajectories is part of the motion estimation framework's assumptions).

- $MIC2$: Second distortion descriptor. This descriptor provides also a description of tissue reconfiguration like $MIC1$, but it adds more terms when there are more dimensions of reconfigu-

J	Volume Change J>1 Expansion J<1 Compression	Tissue changes its volume compared to the initial state
Rotation	Angle of finite rotation and axis of rotation	Angle of rotation of the domain from its initial position around a moving axis
MIC1	First distortion parameter	Parameter that varies linearly with the amount of shearing deformation from initial state
MIC2	Second distortion parameter	Parameter that varies with the amount and dimensions of shearing deformation from initial state
$\{c_i\}$ / $\{b_i\}$	Finite deformation components	Magnitude and geometry of deformation
$\{ic_i\}$ / $\{ib_i\}$	Isochoric deformation components	Magnitude and geometry of deformation not producing volumetric changes

Table 4.2: Lagrangian descriptors:
The description relies on the evolution of the trajectories based on an initial state, so the descriptors not only considers the changes in the topology of the nuclei positions, but how they evolve describing shapes along time and which are the relations between the trajectories describing a continuous system.

ration. In other words $MIC1$ and $MIC2$ will be similar when the tissue reconfigures oriented in a plane and $MIC2$ will be larger than $MIC1$ when the tissue reconfigures with two plane orientations.

- θ: The angle of rotation (also named as $Rotation$ in this document) quantifies how much a domain has rotated over itself through time. The direction of the rotation may vary along time and it can be calculated as described in the Anexo (Euler's theorem).

- c_i, b_i, e_i: The principal components of the Cauchy-Green tensor provides information about the strains undergone by the tissue and their directions and magnitude. The eigenvalues of the right and the left CG tensors C and B are the same, so we will consider them as the principal strain components e_i.

- ic_i: The principal components of the Cauchy-Green tensors of the isochoric deformation. This descriptors provide information about the geometry of the shape change of the tissue in long time intervals isolated from the volume change.

- $FTLE$: This descriptor provides information about which is the most expanding direction of strain. It separates repelling structures in one direction (positive values) and identifies sink-like structures in $2D$ (negative values).

For the shake of simplicity, we have selected J, θ, $MIC1$ and $MIC2$ to generally describe finite deformation in $3D$ data as they capture the main behaviors in an isolated way: compression/expansion, rotation and distortion (that requires two parameters in $3D$). Additionally e_1, e_2 and geometrical projections have been used in $2D$ data. In $2D$ we also used the $FTLE$ descriptor to observe repelling and attracting structures.

4.4 Temporal analysis of deformation

The instantaneous and finite-deformation tensors and descriptors are tools to perform an analysis to find patterns in different temporal length-scales. Minimum spatial scales are characterized by the source of information and the motion estimation method. Figure 4.2 shows the different types of temporal analysis that can be performed with these tools.

- Instantaneous: This analysis explained in section 4.2 only considers each spatial position within the trajectories[2].
- Incremental temporal window analysis: This analysis exploits the trajectory based representation to generate a time series of finite-time tensors and descriptors setting a fix temporal reference and obtaining the deformation in incremental intervals of analysis. This analysis generates a profile of cumulative deformation regarding the initial state. Therefore, the instantaneous deformation description is the temporal derivative of this description given a initial state. The deformation is always expressed at the end of the incremental time interval.
- Sliding temporal window analysis: This analysis moves the temporal reference to calculate the finite-time descriptors with a fix length interval of time. This analysis generates a new series with rescaled deformation temporal scale. For example, for a sequence of data with time step of 10 seconds, it would generate a new series where each step shows the deformation along one minute or one hour. This analysis allows to express the deformation at the beginning and at the end of the interval defined by the time window.

4.4.1 Incremental window analysis

The incremental time analysis from a time reference t_n returns the cumulative deformation from the state at that time as a series of $FTDG$ tensor fields $\mathbf{F}_{\mathbf{n}}^{\mathbf{W(t)}}(t_n + W(t))$. An incremental window $W(t)$ is used to measure the evolution of a local domain from the initial state at a time point of reference t_n, either forwards $t_n + W(t)$ or backwards $t_n - W(t)$ being $W(t) = |t - t_n|$. The analysis forwards

[2]Reminder: high temporal resolution is assumed

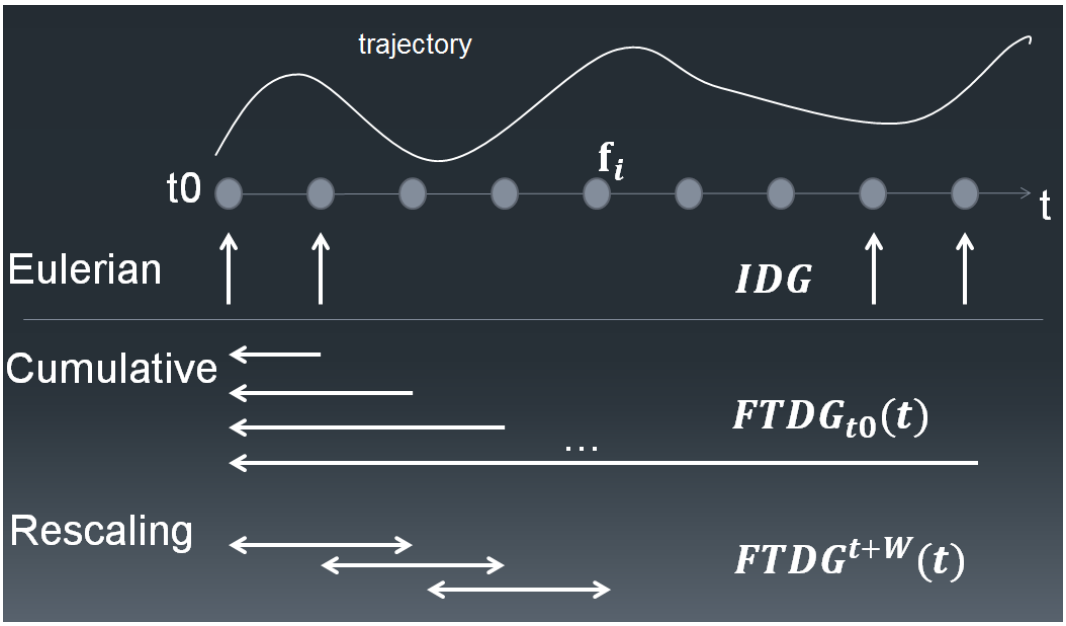

Figure 4.2: Temporal analysis of deformation:
The trajectory based representation (Lagrangian) allows a instantaneous description, but also cumulative along the trajectory and a temporal rescaling of the deformation.

captures the cumulative deformation undergone by the the local domains around the $\mathbf{X}(i, t_n)$ samples of the positions map. Each time layer of the tensor field $\mathbf{F_n^{w(t)}}$ is computed as described in section 4.3.1:

$$Trajs_{W(t)}(t_n \rightarrow t) = \{traj_{1W(t)} \ \dots \ traj_{lW(t)}\} \tag{4.5}$$

On the other hand, the analysis backwards predicts the deformation of the embryo until reaching the configuration at t_n. The backward tensor field $\mathbf{F_n^{w(-t)}}$ is computed by applying eq. 4.4 to the tracking:

$$Trajs_{W(t)}(t \rightarrow t_n) = \{traj_{1W(t)} \ \dots \ traj_{lW(t)}\} \tag{4.6}$$

obtaining $\mathbf{F_{w(t)}}^{\mathbf{n}}$ and then inverting the tensor field $\mathbf{F_n}^{\mathbf{w(-t)}} = \mathbf{F^n_{w(t)}}^{-1}$

4.4.2 Fixed window analysis

Using a fixed integration window W, it is possible to rescale the deformation in different time intervals ($\delta t \rightarrow W\delta t$). This is possible by calculating the *Finite Time Deformation Gradient -FTDG-* field represented in two configurations ($\mathbf{F_W}(t_n)$ and $\mathbf{F_W}(t_n + W)$) along the trajectory for the intervals $[t_n, t_n + W]$. Using the original configuration $\mathbf{F_W(t_n)}$, the derived descriptors show a predictive local behavior along W. The configuration $\mathbf{F_W}(t_n + W)$ shows how this cumulative mechanical

activity organizes after at the end of the interval analyzed. The computation of the $FTDG$ tensors is performed as described for the incremental window analysis but for intervals of the trajectory field defined by the fixed window W:

$$Traj_W(t_n \rightarrow t_n + W) = \{traj_1 W \ \ldots \ traj_l W\} \tag{4.7}$$

4.5 Analysis of descriptors as Lagrangian profiles

4.5.1 Lagrangian profiles

Using the trajectory based representation, it is possible to switch between a map representation of descriptors (visualized in terms of the map $\mathbf{x_i}$) and a trajectory based representation that will be called Lagrangian profile. A subset of trajectories defines a material domain M (points that have an associated trajectory so they are defined as material points with a complete spatio-temporal mapping within the interval). Thus, instantaneous and finite-time descriptors can be expressed in terms of the trajectories of M: $E(M,t)$ or $L_n^m(M,t)$.

Material domains are generated as the subset of the trajectory field that passes by a given tissue region or cell domain previously labeled or segmented. This is an important advantage to, for instance, profile the behavior of a cell as it does not require a whole segmentation of the cell for the sequences of images, but a segmentation in one step that is used to select the associated trajectories. Moreover, a given morphogenetic domain of the zebrafish embryo such as the early eye field M_{eye} can be profiled through several stages with descriptors using the trajectories of the flow field passing by a labeled cell population (selected by embryologist) in a stage where it is recognizable. Thus, the mechanics of tissues and morphogenetic domains are profiled, providing an statistical characterization (mean and variance) of the history of deformation undergone by all the cell population within the domain.

$$E(M,t_i) = \{e_{traj_j}(t)\}_n^m traj_j \in M \text{ and } t \in [t_n, t_m] \tag{4.8}$$

where e_{traj_j} is any instantaneous descriptor along each trajectory in M (instantaneous profile).

$$L_n^m(M,t_i) = l_{traj_j}(t)_n^m traj_j \in M \text{ and } t \in [t_n, t_m] \tag{4.9}$$

where each l_{traj_j} shows a finite-time descriptor along a trajectory relative to an initial state (cumulative profile).

4.5.2 Profiles categorization

The individual profiles within a domain M can be further segregated into M_k subdomains that minimize the variance of a distance distribution between the Lagrangian profiles $l_j = l_{traj_j}(t)$ of the

trajectories in M. In order to both weight the magnitude and the temporal evolution of the descriptor, we use a distribution of distances based on the cosine metric defined as follows:

$$d_{cos} = 1 - \frac{l_s l_t^{'}}{\sqrt{l_s l_s l_t l_t^{'}}} \tag{4.10}$$

The resulting distribution is used as the input for a k-means clustering, chosen as classification tool for its simplicity and because it generates independent and additive classes according to the distance. Several k values can be used to evaluate statistically several partition levels for each descriptor. The number of k in the clustering must be optimized checking experimentally the evolution of the variance of the resulting segmentation. A canonical profile is defined as the average profile of the population within the cluster (appropriate because the variance has been minimized). The different canonical profiles for each descriptor form a basis that explains the different types of profiles for that descriptor within the original domain M.

4.5.3 Mechanical signatures and organization of profiles

Trajectories within the domain M can now be expressed in terms of a *mechanical signature*, consisting in the binary projection of the trajectory into the basis of canonical profiles $B(M)$. Basis can contain as many descriptors and the corresponding canonical profiles as considered. Thus, each trajectory is described by a distance feature that comprises the mechanical description calculated. The classification of trajectories according to their mechanical signature returns populations within M with the similar mechanical features across all the descriptors considered. Hierarchical clustering [Saraçli et al., 2013] was used to classify trajectories, comparing each mechanical signature with the Euclidean distance. This clustering approach allows us to segment the domain M into new sub-domains which have the same mechanical behavior as determined by the basis of canonical profiles $B(M)$.

4.6 Conclusions

In this section we introduced a computational framework built over the continuum mechanics formulation, specifically based on motion kinematics. A Lagrangian description based on the trajectory fields enabled the quantification of instantaneous and finite-time deformation descriptors. These descriptors were suitable to understand the local and instantaneous behavior of tissues, previously exploited in other frameworks [Blanchard et al., 2009, Bosveld et al., 2012], but also to understand the deformation of the tissues as a result of sequences of mechanical activity in different temporal length scales.

The Lagrangian description allowed us to visualize the descriptors as spatial maps but also as biomechanical profiles associated to the trajectories. Biomechanical profiles analysis based on unsupervised clustering techniques was proposed in order to deal with the high dimensionality of the data.

This approach could be enriched with other statistical tools and machine learning strategies, although, the simplicity of theses procedures ensured that the results would be driven by the descriptive capabilities of the framework. We expect that this analysis will be critical to understand the role of mechanics in the embryo shaping process and how tissues differentiation happens during embryogenesis as it will be illustrated in the next two chapters.

Chapter 5

Characterizing the mesoscopic mechanical patterning of the zebrafish gastrulation

The proposed methodology has been applied on *in-vivo* data of zebrafish development between 7 and 14 hours-post-fertilization (hpf). We will quantify mechanical patterns and their spatio-temporal organization in the length-scale of gastrulation, trying to relate them to the configuration of the cell fate map. The tracking-based implementation of the motion model has been applied using the BioEmergences cell tracking as source of information and has been connected to the platform's visualization tool Mov-IT [E. Faure et al, 2015], allowing interactive profiling of tissues, cell selections and also providing visual representation of kinematics descriptors and mechanical clusters. First, details on the data used and the specific configuration of the methodology for this analysis are presented. Then, the results with biological interest are presented, providing a global perspective of the potential of the methodological contribution of this PhD Thesis to the community of developmental biology researchers. The conclusion discusses about the future improvements and potential biological applications that this paradigm of embryogenesis analysis may bring.

5.1 Materials and Methods

5.1.1 *In-vivo* images of zebrafish

Five zebrafish wild-type embryos have been cultured and image ($Z1-5$, see Video). Embryos were injected [Brend and Holley, 2009] with fluorescent [Chudakov et al., 2010, Stearns, 1995] EGFP for cell membranes and H2B mCherry for cell nuclei. A two-photon Leica SP5 microscope[1] has been

[1] http://bioemergences.iscpif.fr/bioemergences/imaging.php

Embryo	x-y resolution	z resolution	timestep	temperature
Da.Re.1	1.37 μ^2	1.37 μ	2'33''	26º C
Da.Re.2	1.26 μ^2	1.26 μ	2'28''	26º C
Da.Re.3	1.38 μ^2	1.38 μ	2'24''	26º C
Da.Re.4	1.38 μ^2	1.38 μ	2'26''	28º C
Da.Re.5	1.37 μ^2	1.37 μ	2'25''	24º C

Table 5.1: zebrafish wild-type embryos acquisition parameters.

Field	Description
CellID	Unique identifier for each cell within the tracking
CellNumber	Identifier within the current timestep
x	Pixels from the image center
y	Pixels from the image center
z	Pixels from the image center
t	Timestep within the timelapse 3D+t dataset
MotherCell	Identifier of the mother cell
reserved	Variable used to identify cells that have been corrected manually and for classification purposes

Table 5.2: BioEmergences tracking parameters.

used to acquire two channels of $3D + t$ dataset for each embryo covering the development interval from the shield stage in the Gastrulation until early segmentation ($6-14$ hours post fertilization -hpf-). Datasets parameters are summarized in Table 5.1.

The orientation of the acquisition setup has been designed to observe the early eye formation but covering the longest observation of the hypoblast in the animal pole. For that purpose, datasets have been acquired from the shield stage ($\approx$ 6 hpf) so the dorsal side could be identified and the orientation could be moved from the animal pole to the posterior part of the embryo where the formation of the midline could be properly observed and the hypoblast could be imaged deeper.

5.1.2 Cell tracking

Cell tracking has been generated using the BioEmergeces workflow processing pipeline. This tracking is based on nuclei detection and a temporal linking algorithm that optimizes the best links and the most complete trajectories. The tracking is output as a comma separated table where each entry of the table represents a nuclei center $\{CellID\ CellNumber\ x\ y\ z\ t\ MotherCell\ reserved\}$. The link between each nucleus position is expressed in terms of the $MotherCell$ allowing the representation of cell mitosis when two nuclei have the same $MotherCell$ (see Table 5.2). This tracking does not

ensure complete and error-free lineage reconstruction, but it does contains mitosis when two cells refer to the same mother cell identifier.

5.1.3 Continuous flow approximation from tracking

The $\mathbf{v_{cont}}(\mathbf{x_i})$ data is obtained as described in section 3.2 to provide the continuous approximation of the digital cell lineage. The values of the parameters necessary are enumerated here: Threshold

T_{ave}	Window for temporal Gaussian averaging (2σ) in minutes
MaxMove	Threshold of speed (μm / min) to discard outliers in the processing of the spatial average
MinLinks	Minimum number of links of a trajectory within the temporal window to discard outliars
X_{ave}	Window for isotropic spatial Gaussian averaging (2σ) in μm
MaxAngle	Maximum angle deviation of the speed at $\mathbf{x_j}$ against the speed at the reference $\mathbf{x}$
MinSpeed	Minimum speed module at $\mathbf{x_j}$ in μm / min
MaxSpeedRatio	Maximum speed module ratio of $\mathbf{x_j}$ against the reference $\mathbf{x}$
X	Window to calculate spatial derivatives in μm

Table 5.3: Parameters for the filtering of the tracking displacements and the regularization to obtain a differentiable vector flow field

values have been tuned by experimental observation of the data using Mov-IT. The selection of T_{ave} is set considering the scale of the high-frequency phenomena to be neglected such as mitosis. The zebrafish datasets presented have been filtered using $T_{ave} = 20$ mins. The spatial parameter X_{ave} has been optimized to obtain the regularization of the velocity field and results of this analysis are detailed described in section 5.2.1.

5.2 Results

5.2.1 Accuracy of the continuous approximation

The regularization of the displacements implicit in the cell tracking data as described in section 3.2 has been performed for the presented data (Fig. 5.1A) using the following values $X_{ave} : \{10\,20\,30\,40\,50\}\mu m$. As shown in Fig. 5.1B, the regularization performed with low values of X_{ave} would result in an averaged second-order function that would not fit to the power law pl_{-2} in the timesteps displayed (6, 8, 10 and 12 hpf). The second-order function by time step starts converging for higher X_{ave} values and saturates for $\geq 40\mu m$. In Fig. 5.1C, the $S2$ curve for $X_{ave} = 40\mu m$ is compared to the power law pl_{-2}, showing that the fitting is more accurate in early stages near the reference position, but for 6 hpf the fitting is worse far from the reference in average probably due to the sharp discontinuity between the midline dynamics and the rest of the embryo. We found out a spatial scale of displacements

averaging $X_{ave} = 40\mu m$ that provides a differentiable vector flow field approximation that enables for a mesoscopic tensorial analysis of the cell dynamics. Thus, we obtain the $\mathbf{v_{cont}}(\mathbf{x_i}) = \mathbf{v_{TR}}(\mathbf{x_i})$ characterization of our motion model to further analyze mechanical descriptors.

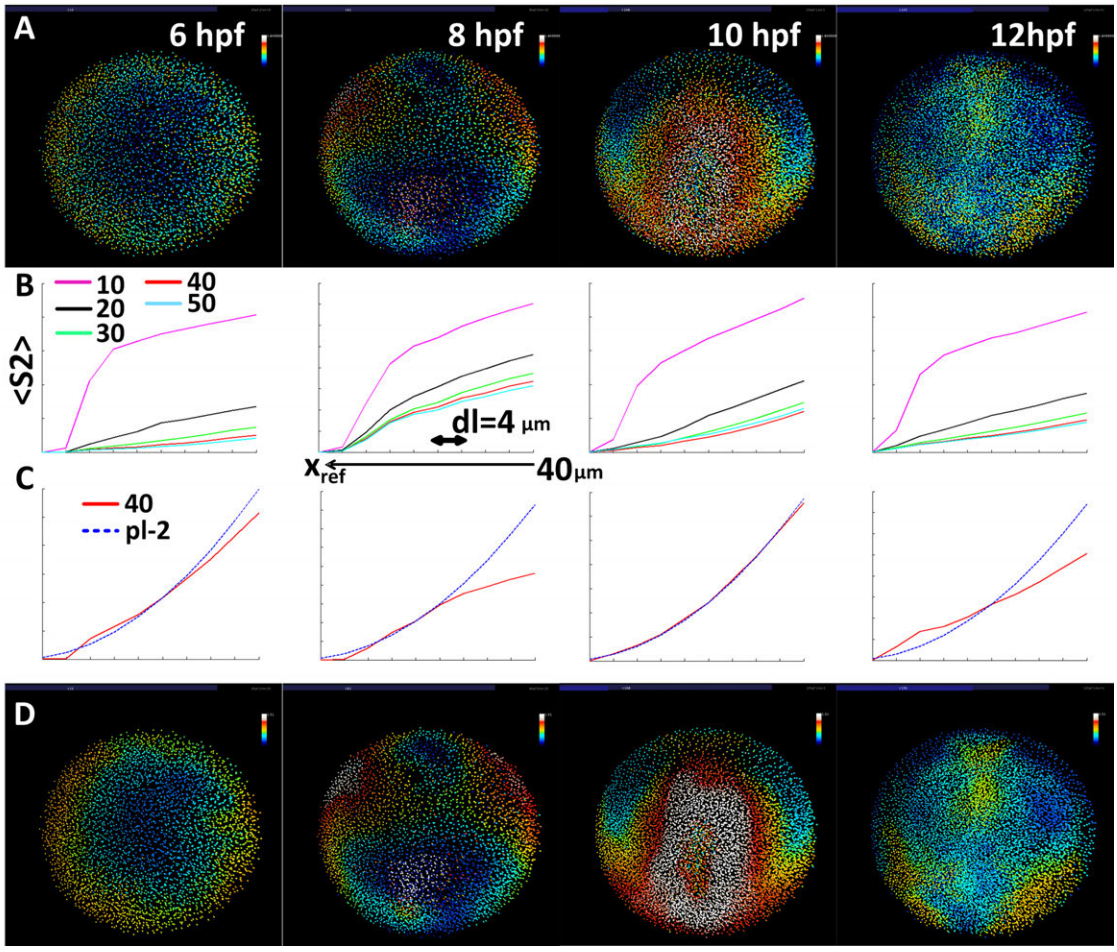

Figure 5.1: Velocity field regularization.
A: Several time steps (6, 8, 10 and 12 hpf) of $Z1$ showing the velocity field built from the displacementes implicit in the cell tracking and processed with the temporal smoothing filter ($T_{ave} = 20$ mins), $\mathbf{v_T}(\mathbf{x_i})$. B: Ensemble average of the $S_2[n]$ function for all the cells in each time step for several spatial scales (X_{ave} from 10 to 50 μm). Curves converge for $40 - 50\mu m$ depending on the stage. The value $X_{ave} = 40\mu m$ has been selected to process the data. C: Fitting of $S_2[n]$ for $X_{ave} = 40\mu m$ to the power law pl_{-2} D: The resulting vector flow field $\mathbf{v_{TR}}(\mathbf{x_i})$ output by the regularization at 6, 8, 10 and 12 hpf.

5.2.2 The phenomenology of gastrulation with quantitative descriptors

The Eulerian description of the embryogenesis dynamics provides a detailed spatio-temporal map of mechanical activity along the stages of the embryo (see Video). A mechanical timeline from 6 to 14 hpf for a zebrafish wild-type embryo, from an animal pole view leaning to a dorsal view, is shown

in Fig. 5.2. In the temporal dimension, the onset and offset of large scale mechanical activity can be clearly identified. Spatially, it is possible to determine the location and shape of the most relevant mechanical patterns. At 6 hpf (shield) the activity at the top of the embryo is low and organized as a planar expansion with an isotropic source point of velocity (see P, $Velocity$). Between $7-8$ hpf, as epiboly goes on, the compression starts dominating the posterior side forming a mechanical boundary between the posterior side and anterior side that is expanding, corresponding with the so-called evacuation area. This layout of large and high activity patterns suggests a mechanical coordination along the whole embryo with a clear polarization between the anterior and posterior sides. However, a disruptive behavior appears in the symmetric bilateral plane in the posterior side, assumed to be produced by the hypoblast moving below the epiblast, giving rise to the appearance of tissue distortion in that region (see Q_d) at 8 hpf. At 9 hours, symmetry from the bilateral plane can be clearly identified. Compression is still high whereas vorticity emerges at both sides and the tissue close to the midline moves fast and linearly (see All). These patterns suggest also that there exists coordination and interplay between the rotation at both sides of the embryo and the dynamics of the midline favoring the movement from the posterior to the anterior side, being the hypoblast the precursor domain of this process. From 10 to 11 hpf, once epiboly is completed, the compressive behavior deceases and forms clusters in the most anterior part of the embryo and also in the most posterior side of the midline imaged, while the distortion at the midline grows and rotation, still in a symmetric layout, forms clear high rotation areas (see Q_d, P, D). This topological description indicates complex large tissue reconfiguration along the midline and the global convergence of the migrating cells from the sides to the midline. At 12 and 13 hpf, large patterns have already vanished and the rotation appears in more local clusters that indicate that the convergence to the midline at this stage is oriented around very specific rotation centers that help to shape the anatomical boundaries of the embryo (see D). At 14 hpf no patterns are distinguished for any descriptor indicating that the range of mechanical activity is lower.

5.2.3 Quantitative comparison of Lagrangian biomechanical profiles in a cohort of zebrafish embryos

The proposed framework allows us now to quantify the dynamics described in the previous section from the perspective of the cells composing the tissues being shaped. For that, we have compared five wild-type zebrafish datasets $Z1-5$ and selected the domains representing the epiblast and hypoblast tissues -M_{epi} and M_{hypo}− (see Video), profiling their Eulerian and Lagrangian descriptors.

In Fig. 5.3A, the profiles show the mechanical activity experienced by the tissues in each timestep between $\approx 7-14$ hpf, characterized with statistics of samples of the Eulerian descriptor fields P, Q and Q_d enclosed by M_{hypo} and M_{epi}. The instantaneous expansion/compression activity, characterized by P, shows a global trend transition from expansion to compression in the epiblast around 7.5

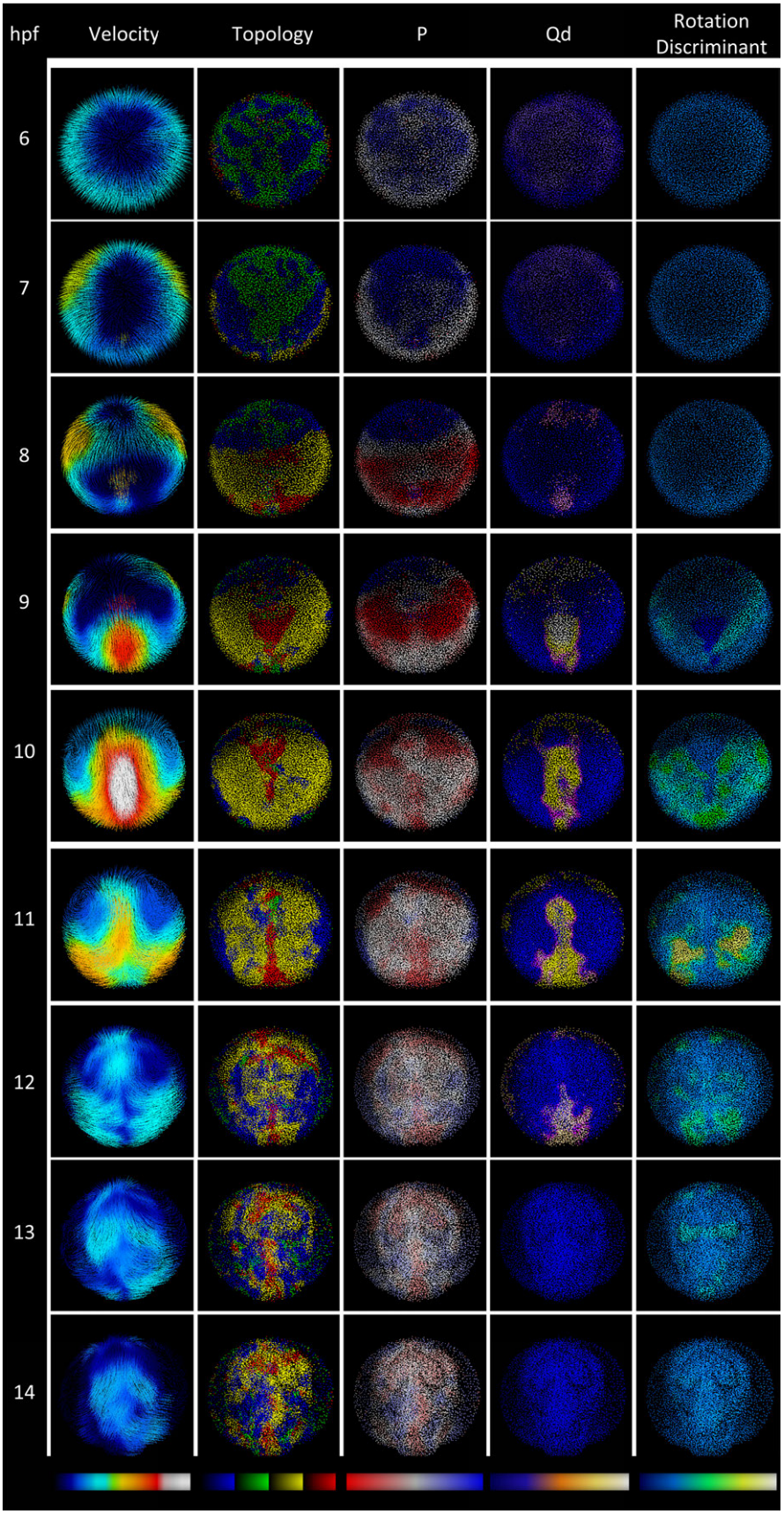

Figure 5.2: zebrafish Development timeline: Timeline of the mechanical activity, as described by Eulerian descriptors, of one wild-type zebrafish embryo imaged from the animal pole along several time points of the development. The times are shown on the left side going from 6 to 14 hours post fertilization. Rows: Time points by hour-post-fertilization. Columns display different Eulerian: $Velocity$, $Topology$, P, Q_d, D.

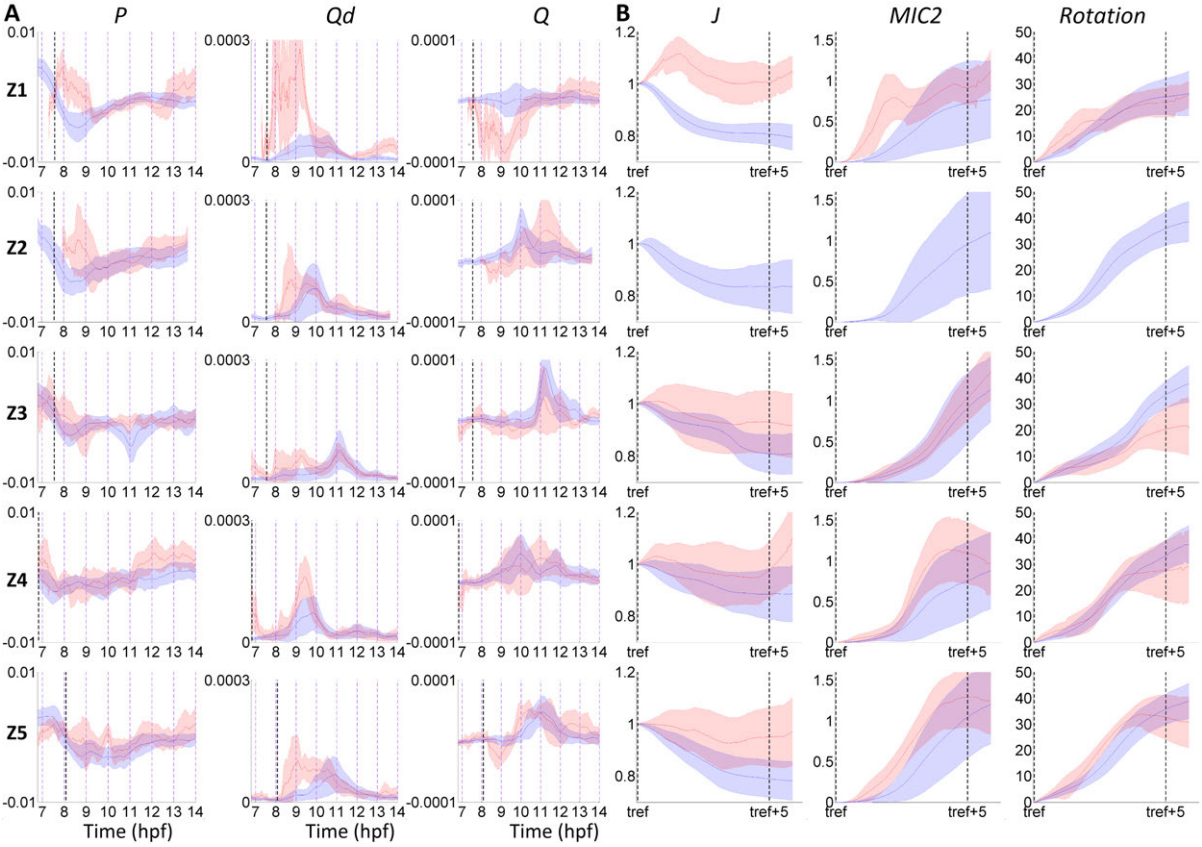

Figure 5.3: Comparison of the deformation profiles of hypoblast (red) and epiblast (blue) of five different wild-type zebrafish embryos (Z1-Z5). Profiles are characterized by the mean (central line) and the standard deviation (symmetric shaded area). The first three embryos were imaged at $26°C$, Z4 was imaged at $28°C$ and Z5 at $24°C$.

A: Profiles of instantaneous stimuli by the statistical characterization of the descriptors P, Q_d and Q along the trajectories comprised in these tissue domains. Time is divided by hours post fertilization (hpf). The vertical black dashed line shows a selected synchronization time t_{ref} that varies between 7 and 8 hpf depending on the temperature used to image the embryo. This temporal reference is chosen as the striking point determined by the transition of the epiblast from expansion to compression.

B: Profiles of cumulative stimuli by the statistical characterization of the finite-time descriptors J, $MIC2$ and $Rotation$ having t_{ref} as the initial state of the tissues . For that, the timeline of the embryos have been shifted to be aligned in the same temporal reference defining a new relative mechanical timeline. The embryo Z2 lacks the profile of the hypoblast as this tissue was not present at this time due to a less ventral field of view and it does not exist in a Lagrangian sense in the new relative timeline. The vertical black dashed line shows a temporal mark of 5 hours past the beginning of the new timeline so the process at this stage can be compared among the embryos.

hpf for $Z1-3$. This transition is observed earlier on at 7 hpf for $Z4$ which was imaged at a higher temperature (27°C) and at around 8 hpf in $Z5$, imaged at 26°C. This sharp event, which is consistent with the timeline in Fig. 5.2, can be considered a robust temporal mark of the dynamics evolution across wild-type zebrafish embryos. The activity in the hypoblast seems to have a different timing although the difference in appearance time of this tissue in the field of view of the data does not allow a very precise quantification across the specimens. However, the temporal shift between the onset of compression in the hypoblast and the epiblast seems to be a very distinctive feature of the Gastrulation process in wild-type zebrafish embryos. The distortion and rotation activity, characterized by Q_d and Q, show a less distinctive pattern across embryos, although certain peaks are observed, they do not occur at the same stage at with the same relative temporal positions in the embryos. We assume this as the consequence of mechanics spatio-temporal variability within one embryo phenotype. This variability, even seen for the same tissues in different embryos, limits the spatio-temporal alignment and comparison of instantaneous dynamics in complex embryos.

The same mechanical activity is now quantified by its cumulative temporal effect in each trajectory within the tissue domains, so that the spatio-temporal effects of the sequence of stimuli happening during the shaping process of the embryos can be compared and understood. For that, the Lagrangian descriptors are calculated for all the domain cell trajectories using the compression onset in the epiblast as a time reference t_{ref} to align all embryos at the same dynamics stage. The resulting profiles for each tissue $\{L_{t_{ref}}^{t_{ref}+6h}\}_{EpiHypo}$ are shown in Fig. 5.3B. It can be observed now how the compression and expansion activity results in an average compression of $\approx 20\%$ of the epiblast, while the hypoblast maintains a more neutral behavior. Note that the hypoblast behavior is worse determined as the amount of tissue present at t_{ref} is not the same in each embryo. The distortion captured by $MIC2$ indicates a growing distortion effect for both tissues with a faster accumulation for the hypoblast and a significant growing variability in the epiblast that may indicate a divergent behavior within this tissue for this descriptor. Rotation for both tissues follows a similar temporal evolution till late stages where epiblast features higher rotation. In general, we interpreted that the deformation induced by mechanical stimuli sequences can be variable instantaneously, but tend to be organize in a similar way along time for specific populations.

5.2.4 Identifying canonical profiles of deformation

Considering the previous results, we have investigated the existence of characteristic sequences of spatio-temporal deformation patterns that converge for specific cell populations. We defined an *in-toto* cell population M_{all} for a consistent classification of profiles. We used unsupervised classification based on k-means clustering over the distances distribution of the trajectories generated with the metric d_{cos} for each descriptor. The minimization of this metric would group trajectory profiles describing the similar temporal evolution of a specific descriptor within the interval. After considering different

levels or partitioning, the canonical profiles for each descriptor are presented in Fig. 5.4A-B. For the descriptor J_{8hpf}^{14hpf}, we observe 3 different behaviors, the tissues may undergo a fast volume reduction, a moderate reduction and an almost neutral behavior. The distortion parameters $MIC1_{8hpf}^{14hpf}$ and $MIC2_{8hpf}^{14hpf}$ have very similar canonical profiles meaning that the geometry of the distortion is organized planarly. One of the canonical profiles features a faster increase of distortion and a general different timing, whereas the other two canonical profiles mainly differ in the level of distortion along time. Finally, the $Rotation_{8hpf}^{14hpf}$ is also decomposed in a mode that has an earlier onset and another two canonical profiles that differ on the level of rotation towards the end.

The profile of the domains M_{hypo}, M_{epi} and M_{eye} are shown in Fig. 5.4C-E projected over the canonical profiles. The hypoblast dynamics can be explained by a single mode for each of the descriptors, J_{m1} in terms of volume change, $MIC1_{m1}$ and $MIC2_{m1}$ for distortion and $Rotation_{m3}$. The epiblast and the eye domains ($M_{eye} \in M_{epi}$) are qualitatively very similar as both are determined by the same canonical profiles: J_{m2}, J_{m3}, $MIC1_{m2}$, $MIC1_{m3}$, $MIC2_{m2}$, $MIC2_{m3}$, $Rotation_{m1}$ and $Rotation_{m2}$.

5.2.5 Spatio-temporal organization of mechanical patterns during zebrafish gastrulation

The information of the canonical profiles is integrated as a mechanical signature for each trajectory for further classification. The mechanical signature is a feature vector based on the projection of each trajectory into a number of canonical profiles (binary projection). Thus, trajectories can be clustered together as described in section 4.5 into domains with similar deformation history along gastrulation. Figure 5.5A shows the ordered distribution of trajectories for the J, $MIC1$ and θ (also named as $Rotation$) canonical profiles into four clusters, whereas Fig. 5.5B shows the statistical distribution of the mechanical signatures of each cluster and Fig. 5.5C shows the spatial organization of each cluster as domains in the embryo (unfolding back the trajectories into spatial points). The first domain (green) is distinguished mainly by being the sole domain containing $MIC1_{m2}$ and $Rotation_{m3}$. The distribution of this domain shows that coherently with Fig. 5.4, it corresponds with the hypoblast, meaning that the hypoblast can be explained by a distinctive behavior in mechanical terms with respect to other any other tissue. The other three domains separate the epiblast with two different symmetries, along the midline and across the midline. The second domain (purple) has a fate distributed along the midline, forming part of the early brain and the eyes. Mechanically, it is distinguished by very high distortion for all the trajectories in the domain which is consistent with the instantaneous distortion distribution along the midline of Fig. 5.2. The third domain (red), located most anteriorly and almost symmetric to the second domain at the reference time, is distinguished by a high compression and its fate forms the most anterior and lateral part of the eyes as a mechanical boundary of the epiblast and epithelial tissue. Finally, the fourth domain (yellow) shows high rotation and it serves to define

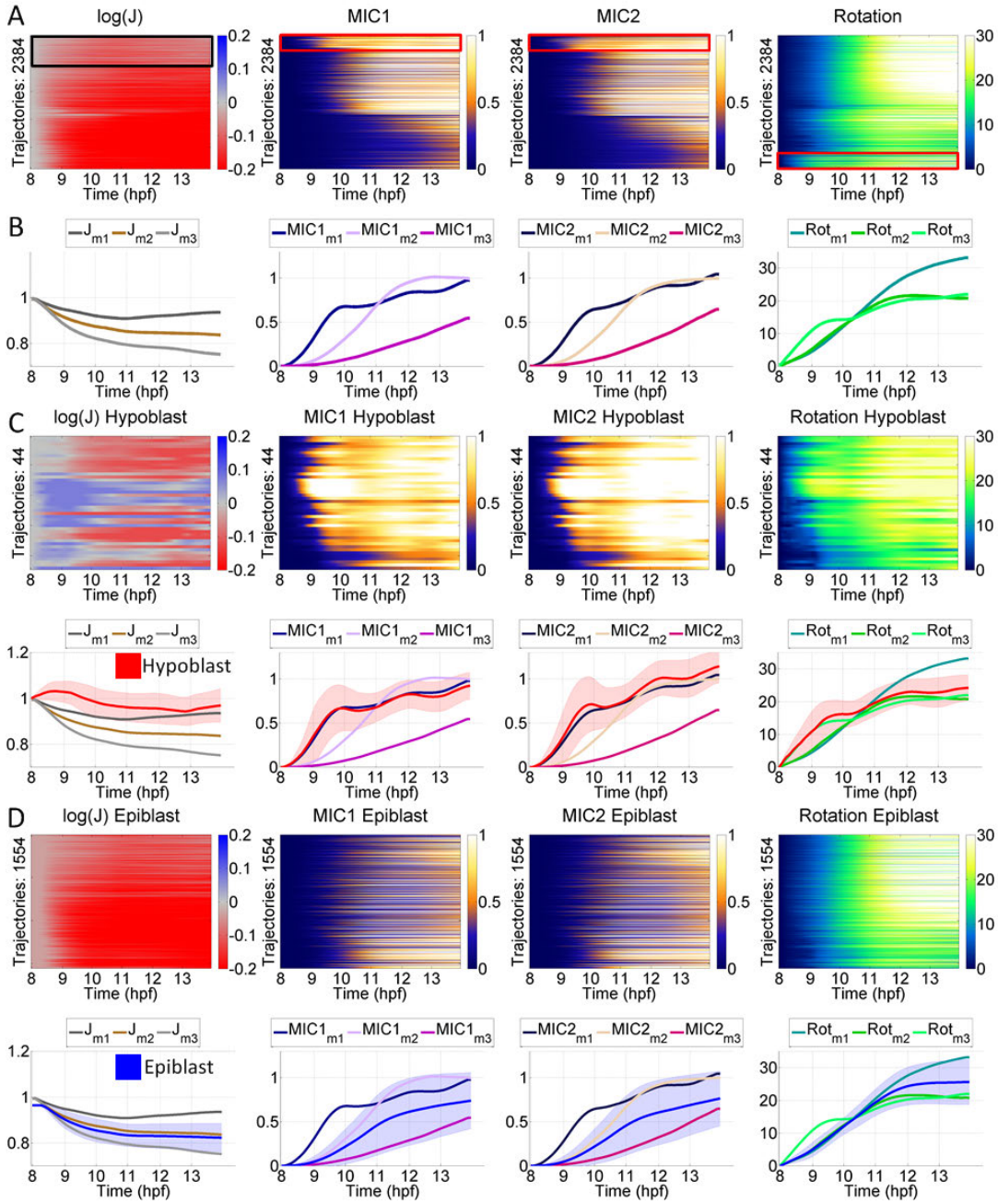

Figure 5.4: **A**: Profiles of Lagrangian descriptors for the trajectory flow field subset M_{all} generated from the cell population formed the epiblast and the hypoblast at 8 hpf. **B**: Modes generated by unsupervised k-means clustering over a distance distribution between all trajectory profiles with a cosine metric. Each descriptor has been categorized in three different canonical profiles that capture the different behaviors optimally. The trajectories profile is ordered according to the cluster output (first row) and the average value of each population of trajectories is used as the canonical profiles for each descriptor (second row). **C**: The mechanical profile of the hypoblast (red shaded area showing mean and std) is shown overlaid to the canonical profiles. **D**: The mechanical profile of the epiblast (blue shaded area showing mean and std) is shown overlaid to the canonical profiles. **E**: The mechanical profile of the eye field (yellow shaded area showing mean and std) is shown overlaid to the canonical profiles.

the eyes posteriorly clearly showing that the convergence towards the midline is closely related by a rotation movement that also helps to define a the anatomical symmetry at both sides of the midline.

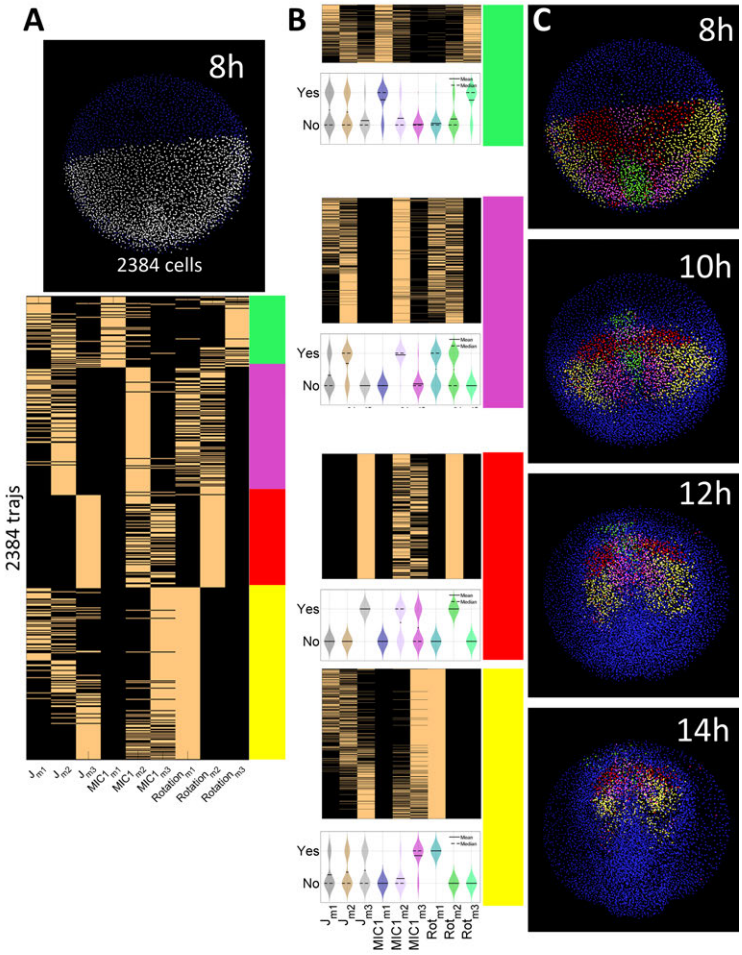

Figure 5.5: **A**: Top: Material domain M_{all} at the $t_{ref} = 8$ hpf covering hypoblast and epiblast (white selection). Bottom: Mechanical signature in terms of canonical profiles of each trajectory within M_{all} ordered by a hierarchical clustering. **B**: Characterization of each cluster segmented according to the mechanical signature revealing more characteristic features. **C**: Several time steps of the spatio-temporal organization of the clusters.

5.3 Conclusion

The framework proposed in Chapters 3 and 4 was applied to characterize mechanical patterns in zebrafish development between 6 and 14 hpf using 5 wild-type specimens imaged with two-photon fluorescent microscopy with marked nuclei. These images were used to generate a digital cell lineage using cell tracking methods which served as the input for the framework. The lineage was approximated as a trajectory flow field that integrated mesoscopic information of displacements (twice the

diameter of a cell) to build a differentiable vector field and the associated complete trajectory field. Descriptors maps derived from the kinematics of the flow field showed that the mechanical activity organized in scales larger than the cell, forming supracelullar patterns between 7 and 12 hours of development. The appearance of these large scale patterns justified the use of continuum mechanics analysis for this interval of the development. However, the framework presented limitations to describe mechanical activity for 12 and 14 hpf, so another strategies (experimental and methodological) should be implemented to measure smaller scale interactions in later stages.

Regarding biological insight, the framework applied to images covering the formation of the presumptive forebrain, allowed us to quantify the main flow topology events that explain large-scale movements during gastrulation in the animal pole. We could also compare the dynamics of the germ layers involved in this stage (hypoblast and epiblast) in a cohort of embryos by analyzing the flow trajectories associated to their cell populations (profiling). Thus, we could observe the same topology events as a history of stimuli experienced by the tissues and compare the timing among the cohort. By comparing the instantaneous and cumulative deformation profiles and maps, it was possible to observe how instantaneous deformation organized through time forming mechanical patterns that described the shaping process.

Moreover, characteristic profiles with a specific spatial organization were extracted with unsupervised techniques revealing order and coherence of the mechanical activity during gastrulation. We obtained a classification of cell domain in terms of mechanical activity what was related to the anatomical configuration of the embryo. Although, more statistical validation and whole-embryo imaging would be necessary, the results suggested that it would be possible to define the phenotype macroscopic mechanics in terms of canonical profiles that could be also used for comparison and assessing the impact of genetic modifications. Furthermore, we expect that with a more complete characterization (genetics and other mechanics scales), this type of framework could help describing the cells differentiation process along several stages of development.

Chapter 6

Drosophila amnioserosa tissue continuous analysis

The framework of analysis proposed in Chapter 3 and 4 has been used to analyze the behaviour of the amnioserosa (AS) tissue, an epithelial tissue of the Drosophila embryo that covers a gap at the dorsal side of the embryo [Gorfinkiel et al., 2011]. During almost three hours, AS cells generate the major force driving Dorsal Closure through the apical contraction of its individual cells [Kiehart et al., 2000]. Previous analysis have shown that this contraction is pulsatile with cells exhibiting periodic $2-5$ minutes oscillations in their apical cell area and driven by the transient activity of the actomyosin cytoskeleton [Solon et al., 2009, Sokolow et al., 2012, Blanchard et al., 2010]. At the mechanical level, AS cells evolve from being a fluid to become more solid-like as the tissue increases its stiffness [Machado et al., in press].

So far, automated studies have relied on measurements at the cell level using cell shape variations statistics and deformation fields calculated with PIV. These metrics do not provide the necessary resolution to allow the observation and quantification of subcellular patterns. Also, cell shape based metrics do not have the necessary sampling to allow the observation of coherent mesoscopic patterns. We apply the B-splines sequential registration implementation of the motion model and the mechanical descriptors to investigate the subcellular and supracellular patterns in the AS cells at different temporal scales thanks to the Lagrangian descriptors. Thus, we discovered that the oscillating patterns of AS are organized beyond the cell structure, showing mesoscopic patterns crossing cells with a temporal dependency on myosin expression, but with a characteristic spatial organization that cannot fully explained through a corelation with the myosin appearance distribution.

6.1 Methods and materials

6.1.1 *In-vivo* images of Drosophila's AS

For the live imaging, we used a stock carrying $ubiECad-GFP$ and $zipperCPTI002907$ (available from Kyoto Stock Center). Stage $12-13$ Drosophila embryos were dechorionated, mounted in coverslips with the dorsal side glued to the glass and covered with Voltalef oil 10S (Attachem). The AS was imaged at $25-28$°C. using an inverted LSM710 laser scanning microscope with a $63X$ oil immersion Plan-Apochromat ($NA = 1.4$) objective. A region of the AS was imaged with an argon laser and using spectral detectors to collect the emitted signal between 495 and $620nm$. $5-6$ z sections $1\mu m$ apart were collected every 10 seconds with a spatial resolution of $0.44\mu m$. GFP and YFP specific signals were extracted using the linear unmixing tool. Imaged embryos were left to develop until larval stages to check that they survive normally until the end of embryogenesis.

With this imaging setup, five datasets $D1-5$ of the AS during the *slow stage* have been acquired and then pre-processed and analyzed. The membranes channel has been pre-processed using the Weickert version of non-linear anisotropic diffusion filtering available as an ICY plugin [Chaumont et al., 2012]. The myosin channel has been pre-processed using $2D$ Gaussian smoothing and a histogram equalization of each frame to homogenize the intensity values along the image sequence.

6.1.2 Digital reconstruction of the AS tissue

Image processing modules have been implemented to reconstruct a digital version of the Drosophila's AS datasets so the mechanical patterns could be validated and compared with cell based measurements. Cell segmentation can be achieved by a range of image analysis techniques when cell markers (such as nuclei detections) are available to initialize the segmentation method. For this analysis, the nuclei stained data was not available, so that one fluorescent channel could be exploited to image myosin expression. A methodology to obtain reliable cell segmentation and tracking without nuclei marked images was implemented as described below:

AS cells segmentation

The filtered membranes channel is binarized by applying Otsu thresholding to obtain an initial rough segmentation of the membranes boundaries. Then, an area opening is used to clean up small objects and a closing is used to close gaps in the initial segmentation. In the image sequence, the AS tissue contour is partially or totally missing due to the depth of the acquisition but it is needed to obtain a robust segmentation of the border cells. This tissue contour is estimated by calculating the convex envelope of the binarized and filtered cells contours. Having the binary contour of the tissue and comprised cells, a $2D+t$ watershed transformation [Luengo-Oroz et al., 2012, Pastor-Escuredo et al.,

2012] is applied to obtain a segmentation of the cells using the redundancy of the spatio-temporal domain and the temporal consistency to improve the spatial segmentation. The centroid of each region in the resulting segmentation is calculated and assigned as the candidate nuclei center for each cell.

Then, a tagging tool (Processing) has been implemented to correct the automatically extracted candidate centers by adding and deleting new ones per time step. The validated markers are eventually used on the original filtered images to perform a full resolution $2D$ watershed to obtain the most accurate segmentation possible avoiding oversegmentation and spatial leakage. This interactive semi-automated method for cell segmentation provides a ground-truth segmentation of the cells boundaries $x_{mem}(t)$ to then validate the continuous motion estimation and create cell-aggregated descriptors.

Cell tracking

Several tracking techniques could be applied including techniques that would exploit the spatio-temporal segmentation calculated before [Maška et al., 2014]. However, as the AS cells do not describe a large migration movement but a local oscillation, a simple method was implemented. The centroids previously validated have been used to generate the tracking with an Euclidean distance criterion between markers in two consecutive frames. Thus, we obtained the ground-truth of the cell size evolution by a discrete perspective to be compared with the continuous approach. It is important to note that kinematics measurements do not rely on this tracking and they rely solely in the trajectory field generated by the B-splines registration module.

6.1.3 Dense mechanical tissue description by sequential B-splines registration

The B-splines framework presented in Chapter 3 is the basis of the workflow of analysis (Fig. 6.1) of the AS in this Chapter. It provides a dense characterization based on the B-splines $\mathbf{g_t}$ of the deformation that allows us to customize the resolution of the description $\mathbf{v_{reg}}(\mathbf{x_i})$ and select multi-scale domains (sub-cellular, cellular or supracellular) to be described. The motion estimation that provides the trajectory field $Trajs$ (material lines of the tissue through time) has been validated using the tissue reconstruction obtained as described in the previous section. This validation step is used to define the registration parameters for the given datasets, so the method is tuned for the specific temporal and spatial resolutions and the scales of the information of the *in-vivo* data.

After the calibration of the registration, the elements of the motion model (differentiable vector field and material trajectories) are used to generate a temporal multi-scale series of descriptors that comprises instantaneous deformation maps (descriptors P, $e1$, $e2$) and cumulative fine deformation descriptors for any interval of time (descriptors J, $c1$, $c2$, $FTLE$). These descriptors are visualized using an ad-hoc platform written in Matlab and also used to generate mechanical profiles of regions of interests as described in the next section of results.

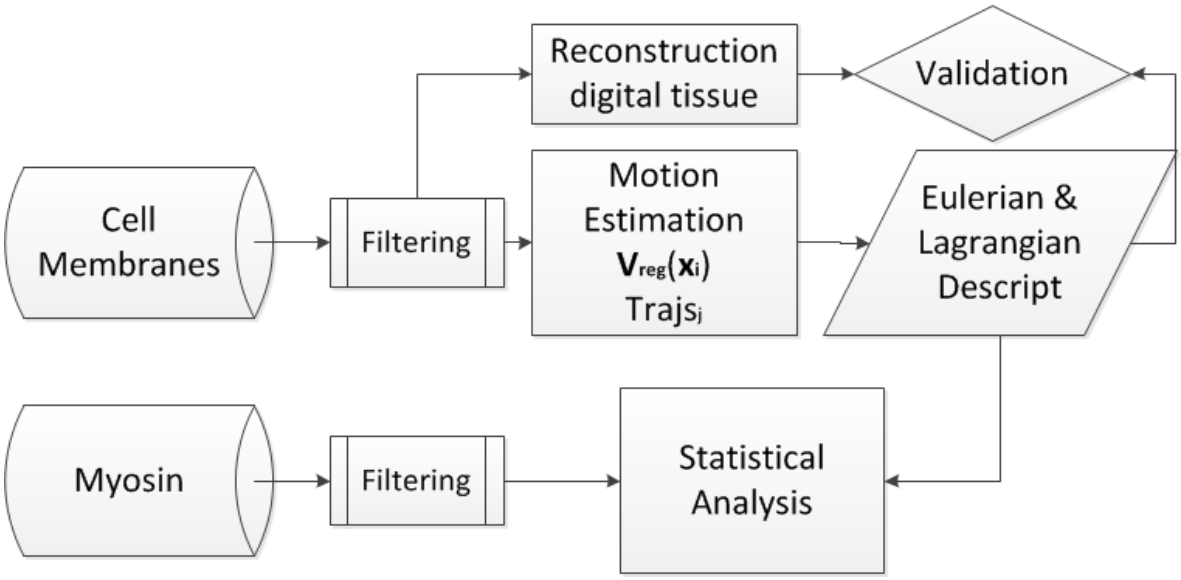

Figure 6.1: Workflow of processing based on B-splines to estimate continuous motion characterization and using image processing tools to validate and initialized the quantification of deformation descriptors.

6.2 Results

6.2.1 Validation of the dense tissue motion estimation of tissue with sequential B-splines registration

The described workflow in Fig. 6.1 has been applied to the five Drosophila's AS dataset $D1-5$ to obtain deformation fields and deformation descriptors derived from tensorial analysis in different time-scales and for several spatial domains. First, we have tested the accuracy of the reconstructed deformation obtained from the B-splines sequential registration. Several parameters values for the B-splines registration module have been used and tested to obtain an optimal configuration. The parameters testing has been performed by using the membranes segmentation (see section 6.1.2) as a reference of the motion in the image sequence as a set of ground-truth points $x_{mem}(t)$. The points defined by the segmentation in the first time step $x_{mem}(t0)$ have been used as the starting points of automatically generated trajectories by integrating the displacements field generated by the B-splines registration (see section 3.3.2). Therefore, these trajectories are an estimation of the cell membranes boundaries positions $Traj_{mem_{t0}}$. This estimation is compared in several time points with membranes contour segmentation $x_{mem}(t)$ of the dataset $D4$ to measure the overlapping and quantify the error derived from the B-splines registration. The overlapping of points along time has been fitted to a power-law to observe the evolution of the error for the interval of time considered (120 time steps or 20 min). This curve has been calculated for several registration parameters so the best configuration is chosen as the one that describes the smoothest decay of the overlapped area along time as shown in

Fig. 6.2, corresponding to a distance between B-splines nodes $cnode = 20$ pixels and a regularization weight $alpha = 0.5$.

The error grows for the first 20 time steps and then it stabilizes before the step 40 to keep and overlapping around the 80% of the points between the independent methods: cell segmentation and the motion estimation. However, the results show that the error does not keep growing, and therefore, the B-splines based trajectories that define the continuous motion model are a suitable tool to describe the dynamics along the intervals of time under study.

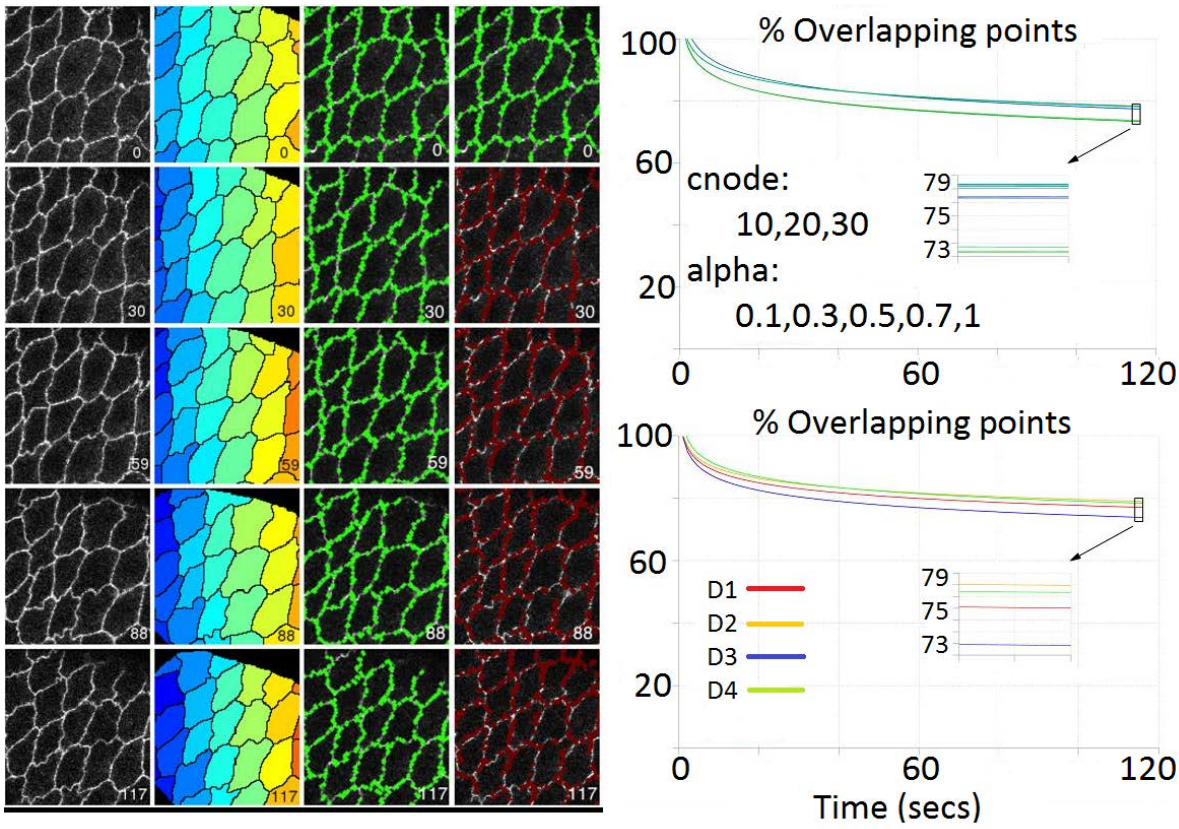

Figure 6.2: A: From left to right: several timesteps (0, 30, 59, 88, 117 seconds) of raw data, membranes segmentation, the original membranes map $x_{mem}(t)$ and the estimated membranes map with the B-splines $Traj_{mem_{t0}}$ starting in $x_{mem}(t0)$. B: The power law fitting of the error as the overlapping between the estimated map and the original membranes map along time for several registration parameters for the dataset $D4$. C: Power law fitting of the error of the best parameters of the dataset $D4$ applied to the other datasets in the study.

6.2.2 A dense mechanical description of AS tissue's instantaneous dynamics

The frame-to-frame images transformations expressed by the B-splines allowed us to define the vector field $\mathbf{v_{cont}} = \mathbf{v_{reg}}(\mathbf{x_i})$ as described in section 3.3. The B-splines can be used to define dense vector fields or grid vector fields depending on the sampling required to measure the target dynamics. For

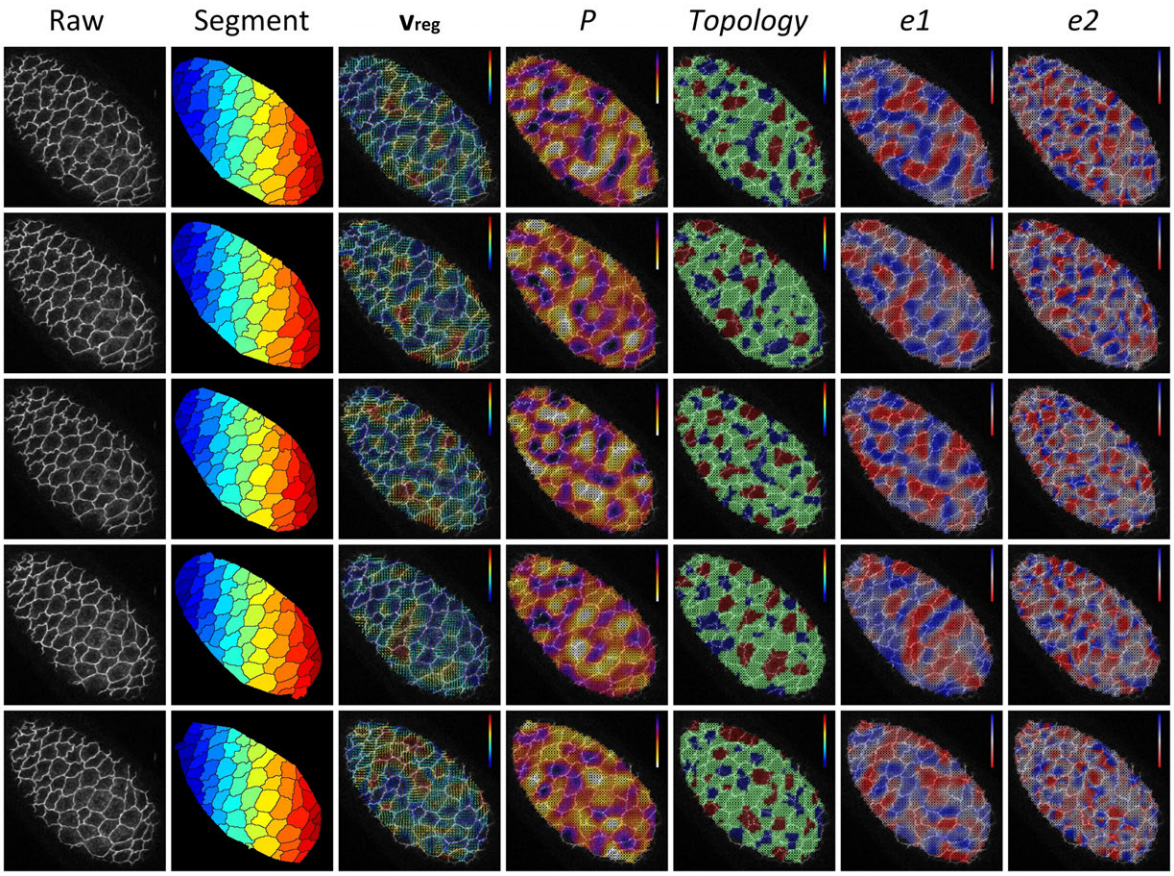

Figure 6.3: Generated descriptors fields in several time points. First column: Raw membranes data. Second column: Cell segmentation. Third column: Velocity field obtained through the B-splines in a grid representation. Fourth column: Descriptor P. Fifth column: Basic topology (red: sink, blue: source, green: saddle). Sixth column: $e1$ first component (greatest magnitude) of strain. Seventh column: $e2$ second component (smallest component) of strain.

this analysis, a grid ($\mathbf{x_{grid}}$) of $10 = cnode/2$ pixels spacing has been used to calculate the vector field and the kinematics descriptors inside the AS tissue (cell diameter is about $20pixels$ compared to the grid spacing $10pixels$).

The evaluation by the B-splines motion estimation of the grid points independently as spatial positions (Eulerian perspective) enables for the quantification of the kinematics as instantaneous snapshots of the dynamics of the AS. Fig. 6.3 shows the patterns of the deformation field, the local area changes (descriptor P) and the principal strain components in the apical plane ($e1$ and $e2$). This description has a granularity smaller than the cell so it provides subcelullar resolution. However, the emerging patterns of this finer resolution show clusters of mechanical activity above the cellular level and across cells, so the spatial patterning of the instantaneous deformation forms supracellular structures. These results support the usefulness of the continuous based analysis, as within the cell, heterogeneous me-

chanical behavior is observed that can not be captured with cell-level measurements of the tissue dynamics revealing supracellular patterns yet to be understood. Furthermore, this result suggests that the oscillatory behavior of AS and its periodicity (spatial and temporal) may be identified at a more local level than the cell but under the constrains of a certain mesoscopic level of organization of the AS tissue even at instantaneous temporal scales (10 seconds)

6.2.3 Characterization of contractile oscillation at the cellular level

Previous quantitative studies of AS apical cell area fluctuations have shown that they oscillate with a dominant frequency ranging $4 - 10mHz$ [Wells et al., 2014, Blanchard et al., 2010]. As DC progresses, there is an increase in the dominant frequency contribution and a gradual decrease in the amplitude of oscillations. These fluctuations are driven by the oscillatory activity of the actomyosin cytoskeleton which oscillates in antiphase with the cell area signal, with peaks in myosin signal preceding troughs in cell area by around 1.3π.

However, the results presented in the previous section show that the deformation of the tissue follows patterns not delimited strictly by cell boundaries. In order to characterize the contractile behavior with the continuous analysis and validate it, we computed the dense representation of the Lagrangian volume change from the initial time step $J_{t0}(t)$ within the cell segmentation along time so we can compare this dynamic profile with the discrete characterization of cell size change $Area(t)/Area_{t0}$. It is important to note that an Eulerian analysis of the deformation with techniques such as the PIV could not provide a consistent timeline of the cell-aggregated deformation from an initial state and could only be used to provide a statistical approximation of the size change rate by the descriptor P.

In Fig. 6.4, we show the error between $Area(t)/Area_{t0}$ and the $mean(J_{t0}(t))$ computed as the squared differences between both time series for each cell. We present two representations of the error: aggregated by time step and aggregated by cell. The error along time for each dataset is presented by the median of the error of all cells in one time step. The results show that the metric behaves well for the datasets indicating that the error due to the sequential registration does not grow uncontrolled along time which is consistent with the results observed in the validation of the membranes boundaries estimation. The error by cell is calculated as the mean of the values along time for each cell. The results show that the error is mainly focused on specific cells which have been inspected visually confirming that most part of the non-matching values between two time series are due to a bad segmentation or problems in the boundaries of the tissue and therefore the source of error is mainly due to the values of $Area(t)/Area_{t0}$ rather than a bad approximation generated by $mean(J_{t0}(t))$.

It can be therefore assumed that the continuous approximation describes properly the changes in the apical surface of the cells to further study the oscillatory behavior of the tissue. Furthermore, the Lagrangian profile of the cell domains does not need a segmentation along all time steps but the initialization of the cell surface at an initial time point getting rid of the task of validating and

correcting cell segmentation for discrete analysis. Also, this analysis provides more resolution of the cell behavior providing a dense spatio-temporal characterization within the cell rather than a single valued characterization based on the segmentation or any other discrete cell-based analysis.

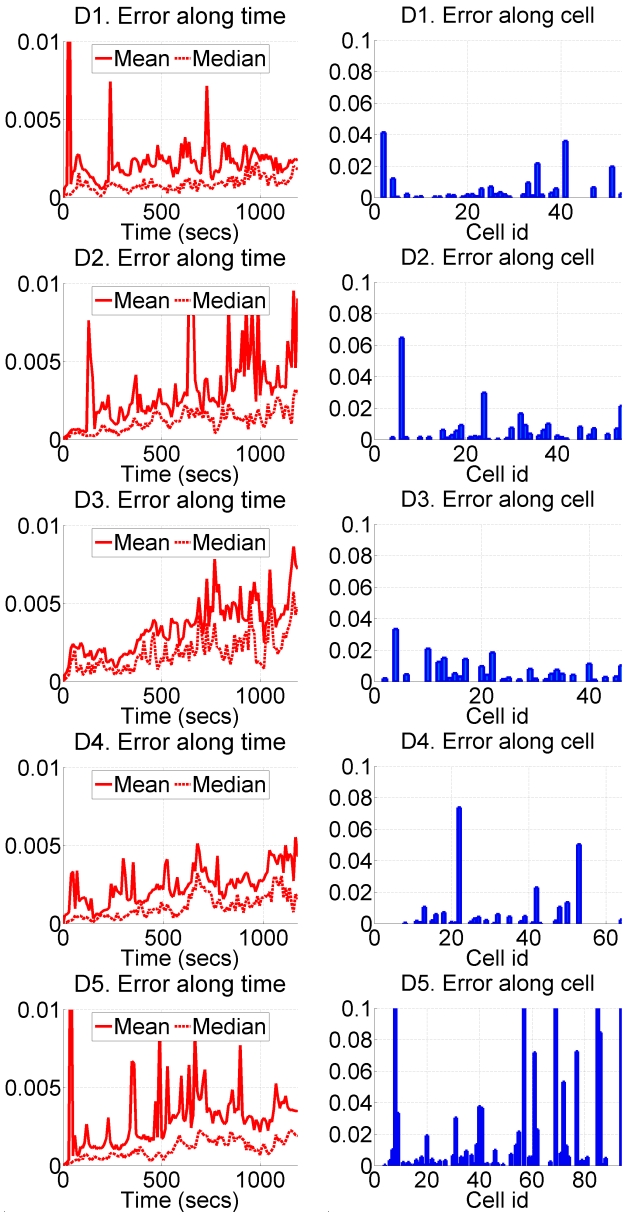

Figure 6.4: Left: Error along time (median and mean of error in all cells) for $D1-5$. Right: Accumulated error by cell averaged in time. Each bar is located at the cell id within the embryo

Fig. 6.5 shows the mean and std of the Lagrangian dynamic profiles $J_{t0}(t)$, $Area(t)/Area_{t0}$ and the level of myosin for some selected cells along time. Here, the $std(J_{t0}(t))$ informs about how similar is the cumulative behavior for the material points inside the cell. Therefore, the increase of the std implies an organization of the instantaneous heterogeneity (Fig. 6.3) into cumulative heterogeneity

between material points even within the same cell. The time series of myosin level for each cell is calculated as the percentile 75% of the myosin values enclosed in the cell region for each time step.

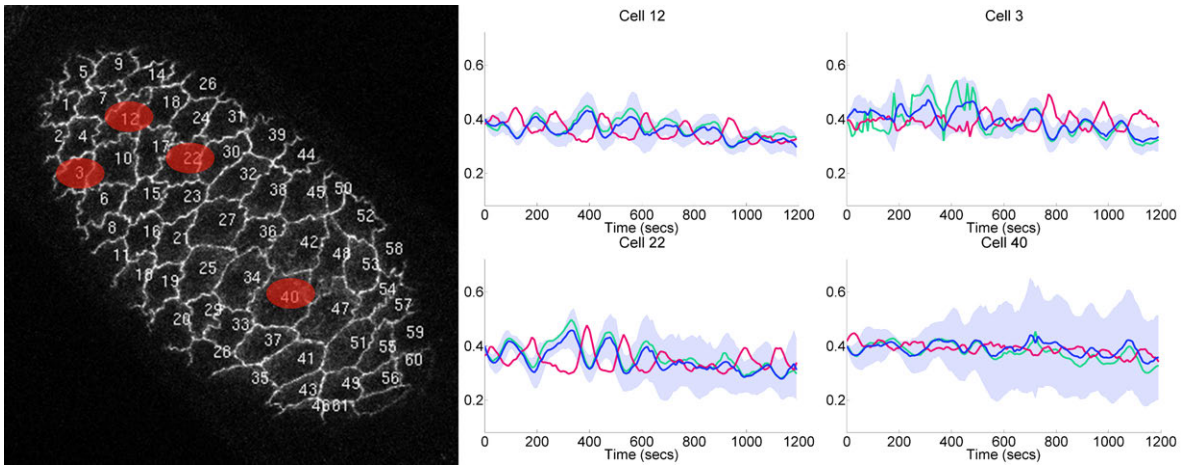

Figure 6.5: Right: Embryo and the id of the cells analyzed. Right: profile of several cells comparing the statistics of J within the cell along time (blue), the area change rate extracted from the segmentation (green) and the myosin estimated inside the cell (magenta)

The results shown a correct correlation with the time series of the cell size as validated above and also an accurate anti-correlation with the myosin level which is also consistent with the literature. Even more, the dense characterization of the cell behaves more robustly without the high-frequency peaks observed for the cell segmentation based characterization which is more sensitive to automated processing errors. Only for some cells, the std grows along time meaning that the heterogeneity of those cells may grow because they occupy a singular location within the tissue where the dynamics are different or they lead to quantification errors.

In general, it can be assumed that the dense characterization of the contractile behavior of the cell in the AS provides at least as accurate results as the discrete analysis of the cells shape, but it provides a richer characterization that may be useful to understand how singular behaviors may play a role in the global organization of the AS dynamics. Moreover, the cellular level analysis based in the sequential B-splines estimation is more robust for an automated analysis because it relies on the trajectory field $Trajs_j$ derived from $\mathbf{g_t}$ an initial segmentation of the cells. Thus, it would not require a supervised correction of cell segmentation for all time steps, but only an initial step validation for the initial labeling of the trajectories generated from the dense grid.

6.2.4 Mechanical oscillation and myosin expression periodicity

The methodology also allows to go to the subcellular level to understand the response of the tissue against the exerted forces but as a continuum instead of observing the aggregated cell behavior. A

tagging tool was used to identify several myosin foci generating the corresponding local spatial region for each of them. This local region is used to select the material trajectories passing through the foci and generating a spatio-temporal material domain of the tissue influenced by each focus. By centering the analysis in the maximum of the myosin focus as reference event, the timeline of deformation of the tissue influenced by the focus can be deconvolved for a time interval around the event.

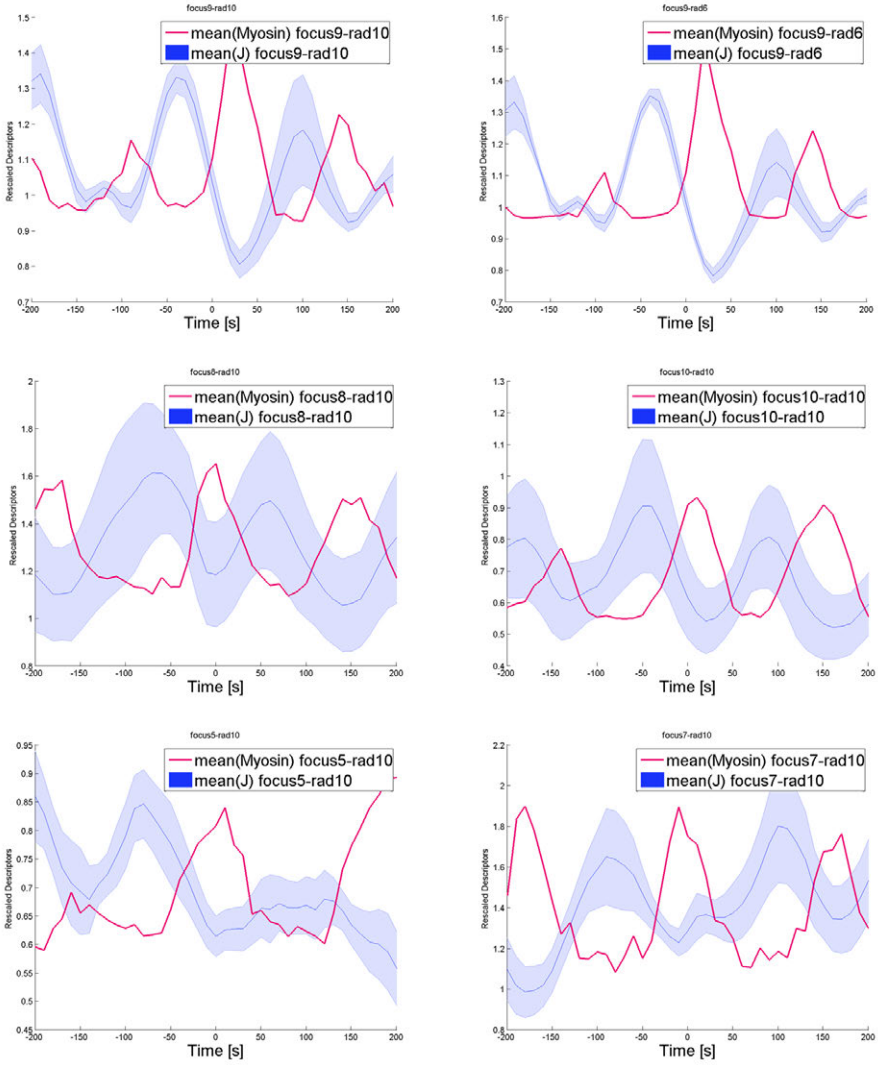

Figure 6.6: Several foci of $D2$ showing the myosin profile and the compression of the tissue J around the maximum of the focus event in space and time

In Fig. 6.6, several foci out of the 20 foci studied for $D2$ have been selected and the profile of a circular region around the foci (maximum radius $4\mu m$) is shown during a symmetric temporal interval. It can be seen that the response of the local domains to the underlying force indicated by the myosin shows important variability. Considering the description of J, the local domain behaves homogeneously in some cases and it would have a heterogeneous behavior in other ones. It is also

interesting that the amplitudes and the time of the response can also vary. This result suggests that the local domains of the tissue respond differently to exerted forces in a very local domain and this variability would possibly have not only a local impact but it contributes to, and is influenced, by higher scales of patterning.

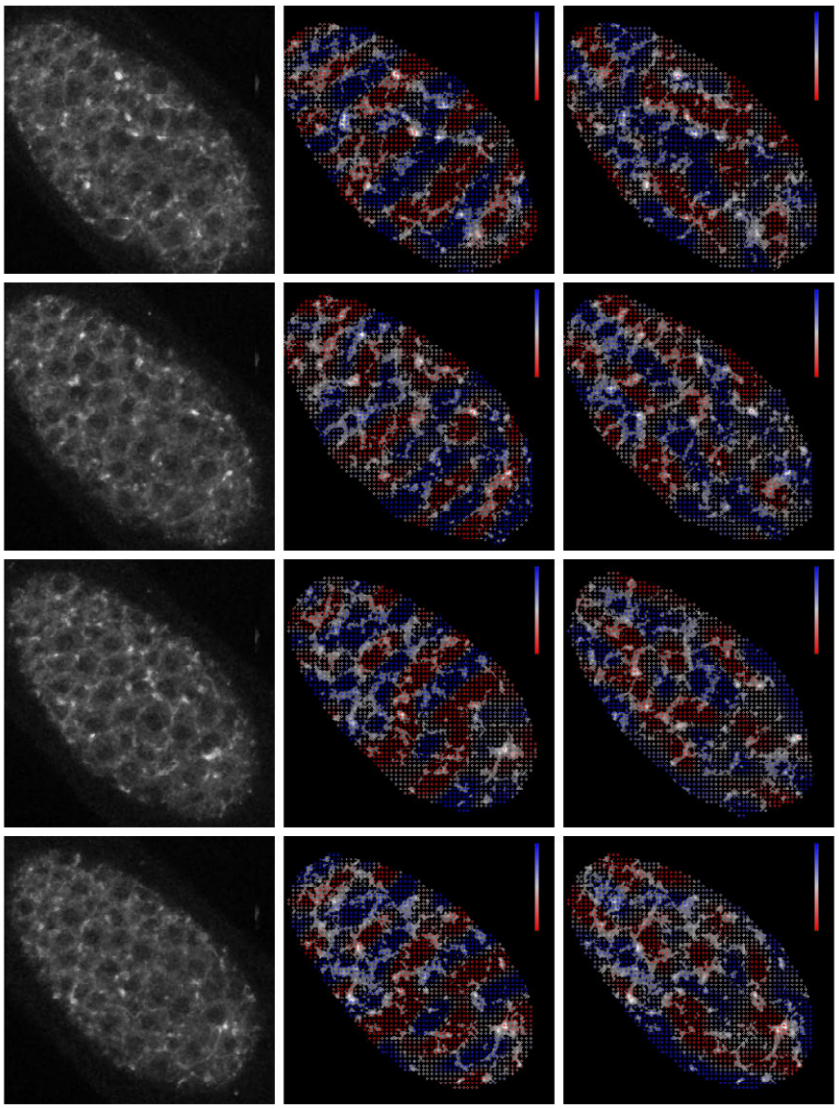

Figure 6.7: First column: myosin labeled image. Second column: Strain rate projected in the AP direction. Third column: Strain rate projected in the ML direction. Each column represents several time points within the 20 mins period analyzed.

6.2.5 Meso-level patterning in the tissue and active force generation

The dense mechanical description of the strain rates shown in Fig. 6.3 suggested the existence of supracellular patterns that potentially emerge from the additive effect of simultaneous exerted stresses,

also regulated by the cells behavior. However, the spatial organization of this oscillatory mechanisms is not yet understood clearly. In order to further understand the spatial organization, we calculated the components of the strain rate oriented in each of the axis of the embryo (anterior-posterior and lateral), resulting in two descriptor fields e_{AP} and e_{ML}. In Fig. 6.7, we observed the myosin channel in several time steps and the patterning described by e_{AP} and e_{ML} (see Videos). The AP strain organizes orthogonally to that axis and the same occurs with the ML strain regarding the ML axis. The patterning is not localized in small blobs but forming stripes along the tissue with a clear continuity that wraps and crosses cells. Interestingly, although the cells have a consistent oscillatory behavior of myosin presence and compression, the patterning of the tissue is not identified with cells but with structures that depend on the geometry of the tissue. This result supports the idea of tissue-level constrains in the deformation leading to local variability and that potentially may regulate the oscillatory behavior of the AS cells.

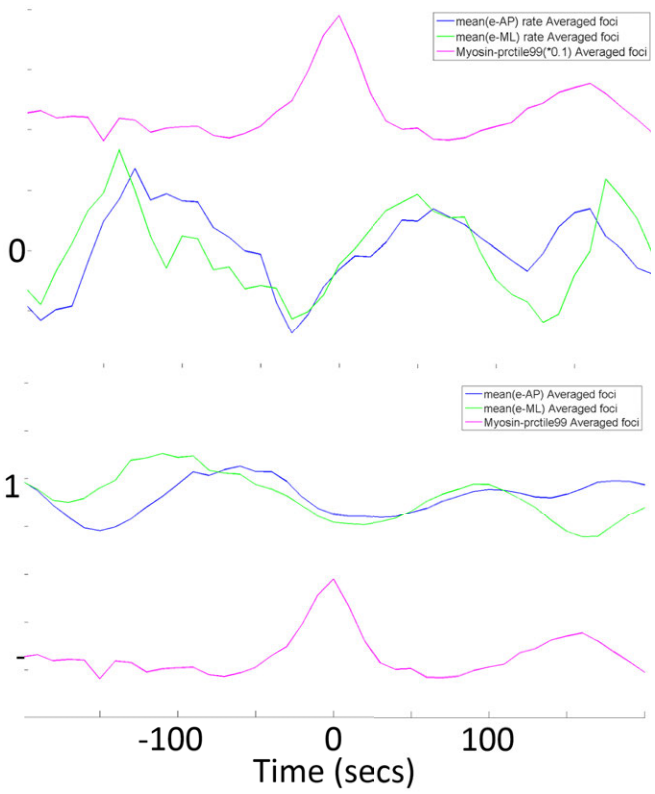

Figure 6.8: Instantaneous (top) and cumulative (bottom) e_{AP} and e_{ML} and myosin averaged for 20 foci in $D2$ centered around the myosin max.

In Fig. 6.8, we compare both the strain rate and the cumulative strain oriented in the two embryo axis and the myosin, averaging of several foci aligned in the maximum of myosin. The rate of strain shows a sharp maximum compression earlier than the maximum of myosing (30 seconds appro.), so

this shift is precise among the selected foci and could be a robust indicator of the tissue behavior. However, the cumulative strain does not show a characteristic event (Fig. 6.8). Another important feature is that both strain rates are negative during the myosin cycle from $40 - 50$ seconds before maximum until 10 seconds after the maximum of myosin.

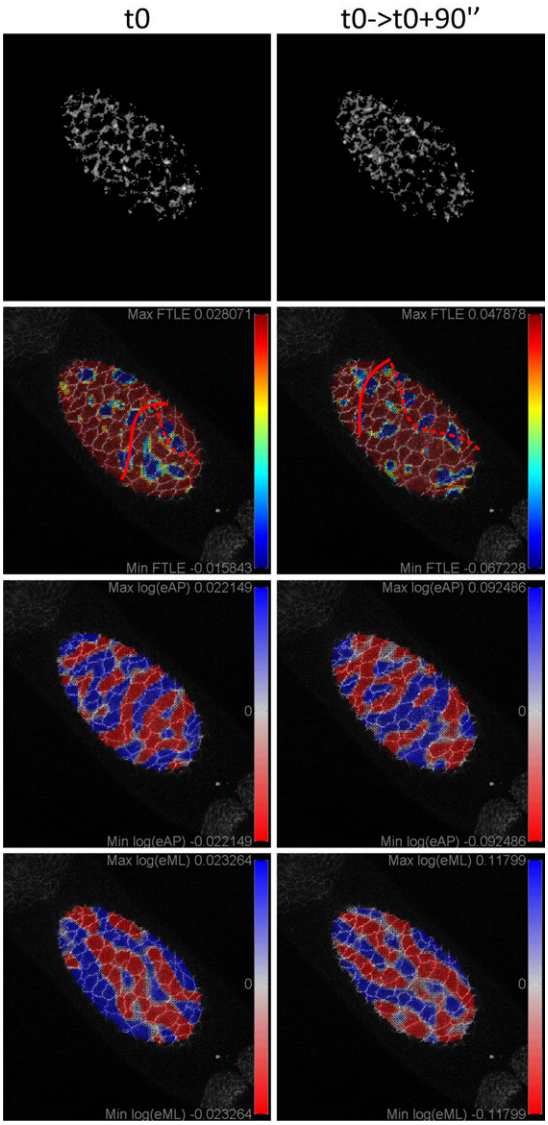

Figure 6.9: First row: Myosin at $t0$ and $t0 + 90$ secs. Second row: $FTLE$ in $t0$ instantaneous (left) and using window integration from $t0$ to $t0 + 90$ secs (right). Third/Fourth row: e_{AP} and e_{ML} for the same integration window. Red lines highlight connected strain paths in the AP strain and dashed red lines for the ML strain.

In order to further understand the timing between the myosin appearance and the compression in the two embryo directions, we computed the $FTLE$ field (see section 4.4.2) for two different temporal scales: 10 seconds and 90 seconds (see Video). By doing this, we could observe the current instantaneous strain and also the strain seen one minute and half after when the compression is over

and the strain would be near the maximum of expansion of the next cycle (see Fig. 6.8). Interestingly, Fig. 6.9 shows compressive regions (blue blobs) in the two directions determined by negative values of the $FTLE$ field organized very locally and symmetrically. In some cases an e_{AP} or e_{ML} stripes emerge as a connected path between $FTLE$ negative blobs. These paths should be analyzed in order to understand the transmission of force along the tissue in specific directions. It is also important to observe a spatial periodicity in the e_{AP} and e_{ML} patterns, consistent with the bidimensional oscillatory behavior of the tissue. As shown in Fig. 6.7, these patterns are likely to depend on the tissue geometry and have a spatial frequency comparable to the cells diameter, however this result also suggests that the patterns could emerge from the propagation of force. Furthermore, the orientation of the patterns is strongly correlated with the orientation of the $FTLE$ blobs. These blobs have also a complementary spatial distribution between the two time windows. Therefore, the tissue seems to adjust to situations of mechanical equilibrium in space and time (possibly regulated by some cellular mechanism) that transmit forces along the embryo under geometrical constraints to finally give rise to strain patterns consistent with the oscillatory behavior of the AS.

6.3 Conclusions

The framework was applied to study the contractile oscillatory behavior of the amnioserosa during the dorsal closure in Drosophila melanogaster embryos imaged with confocal fluorescent microscopy. The continuum analysis of the motion estimated with the B-splines sequential registration offered a resolution of the deformation at the subcellular level. The visualization of the descriptors discovered supra-cellular patterns underlying a tissue organization not fully correlated with the cells of the tissue. Furthermore, the results suggested that the supracellular patterning cannot be explained only by a spatial organization of the myosin foci as we observed strain patterns emerging between foci at long spatial distances. We assumed that this strain propagation depended on the tissue state and the relaxation level of the tissue (not influenced by other myosin foci), being influenced also by the tissue geometry (clear AP and ML oriented patterns). Therefore, it could be hypothesized that this deformation patterning would require an organization coupling several scales yet to be quantified.

Further analysis should be done to more accurately describe the different types of deformation response to the myosin concentration. This characterization would serve to generate models of the contractile oscillation as a continuum. An initial hypothesis of the patterning mechanism observed is that the tissue responds to a characteristic frequency determined by the acto-myosin network that generate forces but selects a spatial phase depending on the state of the tissue (history of spatio-temporal mechanical stimuli and geometry constraints). Eventually, the model should include a multi-level interaction in different time-scales between force generation points (indicated by myosin foci), the tissue organization mechanism and the cellular regulatory behavior.

Chapter 7

Conclusions

7.1 Contributions

Given the objectives described in section 1.2 and the state-of-the-art described in chapter 2, the main contributions of this PhD Thesis are the following:

- A framework to quantify the multi-scale deformation patterns undergone by tissues and cell domains during the shaping process of embryogenesis in different time length-scales.
- The framework relies on a Lagrangian description of the system based on implicit trajectories in a continuous motion to build multi-scale deformation and strain descriptors.
- Furthermore, a new representation scheme that enables the comparison of cohorts of specimens in terms of biomechanical profiles, independent of spatial coordinates. This comparison is therefore based on the history of deformation instead of the matching spatial patterns. The approach seems better suited to quantify the synchronism of local bio-mechanical processes along any stage of development.

In order to implement such a framework, several modules have been designed and implemented:

- A continuous motion description that is either estimated using particle tracking or B-splines sequential registration, so the framework can be applied to a wide range of data and biological studies, adapted to the level of organization of the mechanical activity. The continuous motion description is composed by a differentiable displacements field and a complete and unique trajectory field consistent with the displacements field, so it can be assimilated to a continuous flow (particles describing long trajectories) or soft tissue motion (local movement of material points within the tissues).

- A validation framework for both implementations so the spatio-temporal continuity of the description can be granted for sequences of data where the temporal resolution enables instantaneous observation of the dynamics.
- A comprehensive framework of mechanical descriptors comprising a complete characterization of the instantaneous and finite-time deformation and strain patterns derived from tensorial analysis over the motion description
- A visualization framework for $3D$ data based on the platform Mov-IT and a $2D$ framework implemented ad-hoc (Matlab) to visualize all the descriptors overlying this information with the different imaging channels and the digital reconstruction obtained from the data.
- A statistical analysis module that exploits the descriptors to profile tissues and find structures and patterns that describe the instantaneous and cumulative mechanical activity in the tissues. Additionally, unsupervised classification has been used to generate unbiased categorization of structures and patterns with a specific mechanical characterization for specific intervals of time.

The framework was applied in the following studies:

- The application of this framework to the study of the zebrafish gastrulation allowed us to define detailed mechanical maps and Lagrangian biomechanical profiles for several stages of its development, providing a quantitative developmental table in mesoscopic mechanical terms. We could provide quantitative assessment of the mechanical differences between the germ layers epiblast and hypoblast and how these tissues describe a specific deformation progression in a cohort of specimens. This was possible by a $3D$ Lagrangian description of the patterns through time. Additionally, we could identify characteristic spatio-temporal patterns of deformation with a spatio-temporal organization that partially explains the wild-type fate map (map of cells differentiation in the wild-type phenotype). These patterns can be therefore considered part of the mechanical organization that shapes the embryo and its phenotype.
- The framework was also applied to characterize the behavior of the Drosophila's amnioserosa (AS), a tissue that shows an oscillatory behavior during the dorsal closure and finally contracts driving the closure of the epithelium at both sides. It was possible to reproduce the results that have been reported using a discrete analysis of the AS cells, but also it was possible to discover supra-cellular patterns of strain components in the orientation of the anterior-posterior and lateral axis that could be the product of the coordination of local biomolecular factors and mechanical constraints imposed by tissue structure and geometry. Furthermore, the framework allowed a sub-cellular characterization of the strain response to the stresses indicated by myosin concentration showing promising results that could lead to a categorization of the local tissue response depending on cellular and supra-cellular conditions.

7.2 Impact and Limitations

7.2.1 Theoretical considerations on systems biology

The *in-vivo* embryogenesis observation and analysis have evolved thanks to the green revolution initiated with the GFP fluorescent protein used as marker of biological processes and structures. Furthermore, significant advances in microscopy technologies are now providing researchers with the experimental tools to study different scales of biological phenomena with high spatio-temporal resolution. Biological compatible markers located inside the embryo enable to image structural and functional information using microscope machinery. However, this observation is so far mediated because the images acquired capture instantaneous snapshots of the underlying processes instead of directly reconstructing them. The *in-vivo* data used to understand embryogenesis is therefore a sequence of snapshots of the development in which each snapshot ($2D$ slices or $3D$ stacks) show a global configuration of the mechanical, genetic and biochemical processes happening in that precise time point. Thus, the processes appeared unwired from their own timeline. Several image processing methodologies have been proposed to connect this spatio-temporal information at the cellular level to obtain the cell lineage. However, even with the best microscope technologies available nowadays, the trade-off between spatial and temporal resolution presents unavoidable limitations to reconstruct cell lineages and quantify precisely fate maps by scalable automated means. Apart from the spatio-temporal resolution limitation, there is indeed a theoretical and experimental bias in how embryogenesis is quantified through the lens of the microscope.

The framework proposed fills the gap to study how mechanical patterning, restricted to a kinematics description of deformation and strain, influences and organizes the embryogenesis shaping processes [Keller, 2012]. This quantification cannot be carried out only with an instantaneous quantification of mechanical patterns in the image, but through a novel representation of the mechanics like the one proposed that enables to quantify patterns along trajectories undergoing the mechanical processes. Thus, this framework generalizes current approaches in $2D$ providing a similar description at the cell and tissue levels, but extending the analysis to discover organization of $3D + time$ patterns in several temporal length-scales. This work approaches embryogenesis mechanics in a systematic way to define elements of the embryonic *mechanome* and explain physics of the embryo *phenomics*.

7.2.2 Selection of motion estimation method

The continuous motion estimation methods proposed enable to generate the mechanics description in a wide range of biological images. The B-splines sequential registration has been fully developed for $2D + time$ data (a $3D + time$ version is available and partially tested for other applications)) and provides accurate estimation of the motion with high-quality image intensity data. The optimal

spatial and temporal resolutions depend on the scale of the motion and the length-scales of the structures reconstructed. We assessed that the B-splines registration would work on sequences of images where the spatial scale of deformation to be analyzed is small compared with the spacing between B-splines control nodes ($cnode$ parameter) that can be afforded. The framework requires that the scale of the deformation can be assumed as infinitesimal for the temporal resolution of the image data. In this PhD Thesis, we successfully used this implementation to study cell oscillations characterized by cell membranes, so several B-splines nodes could be place within a cell so the resolution of the displacements was highly subcellular. The quality of these images was high and the temporal resolution (10 seconds) favored the registration because the membranes movements were smooth along the image sequence. The application of this framework to $3D$ images would require very high-quality images in z-dimensions so it does not hampers the accuracy of the estimation. The B-splines registration presents the main advantage, over other image based techniques such as PIV, that expresses the deformation in terms of continuous functions allowing a more natural, detailed and also analytical representation of deformation driven by continuous motion.

On the other hand, the tracking based implementation is very suitable to scales present in $3D + time$ data showing large movements. The tracking methods estimates movement in terms of particle detection, therefore the approach is less sensitive to image quality degradation along the z-dimension than image based methods such as PIV and B-splines. However, the scale of the deformation observed is based on relative motion cell trajectories forming a sparse and heterogeneous displacements field. Therefore, this source of motion data requires integrating the information at a mesoscopic scale in order to provide a description. This approach highlights patterns underlying collective behavior and a magnitude of motion comparable to the cell size, so the nuclei displacements provide significant information given the temporal resolution of acquisitions.

In the study cases of this Thesis, cell tracking approach was not able to obtain a dense characterization of amnioserosa tissue as cells do not change their position significantly through time, but only their membranes deform in a scale that is much smaller than the cell size between steps. Conversely, B-splines sequential registration in $3D$ did not produce satisfactory results in the datasets of zebrafish gastrulation, because of the difficulties derived from the complexity and resolution of the data, to optimize the registration. High density of splines control nodes led to badly optimized and expensive computation registration, whereas low density of control nodes led to a bad estimation due to the quality of the $3D$ stacks. However, the B-splines sequential registration has been successfully applied to $3D$ data in parallel studies to this Thesis after defining very specific quality and resolution requirements. In large embryos, this type of motion estimation would be useful to estimate motion along the segmentation stage and late development of concrete structures could be analyzed in $3D$.

It is important to point out that the scale of movement observed instantaneously depends on the temporal resolution, so any process could be imaged with very high temporal resolution allowing

the use of intensity based techniques such as registration. However, the temporal resolution must be optimized globally along the sequence and the scale of motion in the interval of interest. In this context, the registration technique could be also used to zoom in during large scale motion processes to describe sub-processes involving smaller scale deformation (such as oscillations and cell contractions during the onset of gastrulation), provided a pyramid of multi-scale resolution images is properly built.

Anticipating future work, it was concluded that hybrid techniques either expressing tracking displacements as B-splines functions or registration methods corrected in smaller scales with detection and linking would potentially help to improve the flexibility and performance of the proposed framework. After all, the theoretical limitation of both approaches comes from the nature of the mechanical processes and the nature of the motion. Non collective behavior leading to network-like interactions and intercalation between small cells would be difficult to be modeled as a continuous vector field and other approaches should be used.

7.2.3 Mechanics considerations

This PhD Thesis covers a kinematics description of embryogenesis as clarified in chapter 1. Kinematics descriptors, which are inspired in continuum (solid and fluid) computational mechanics, are derived from the estimated motion under the assumption of local spatial differentiability and smoothness of trajectories, with a temporal resolution of the imaging that provides ”instantaneous” description of the dynamics along the sequence of images.

The description provided does not assume any type of mechanical properties of tissues, cell autonomous behavior or localization of exerted forces. Due to the findings of the research along this Thesis, it is not clear which is the best strategy to characterize mechanical properties or to infer stresses *in-vivo* from the strains quantified. Several techniques, inspired in Traction Force Microscopy [Hall et al., 2013, Ishihara et al., 2013], try to solve local inverse problems. This approach seems suitable for very specific mechanical situations, where cell behavior and interactions through cell junctions (forming local deformation patterns) and tissue properties have already configured. However, the complexity of interactions, produced by concurrent active and passive multi-scale behaviors [Blanchard and Adams, 2011] during embryogenesis, makes very difficult to generalize approaches where stresses have to be inferred from the same source of data from which strains are calculated. Furthermore, the inherited difficulties to determine a ”zero-force” state in developing tissues increases the complexity of experimental and analysis methods to quantify embryogenesis forces *in-vivo*. This problem is currently addressed with laser-cuts methods to determine a ”zero-force” state at the time of the tissue ablation by the laser, which avoids a non-invasive *in-vivo* observation of the embryogenesis after. We believe that it would be necessary to introduce passive elements with known mechanical properties in the tissues that report about stresses, in the direction of the work proposed by Campas

et al. [2014], for further advances in the field.

From a larger scale perspective, a hydro-dynamics behavior of embryos during embryogenesis has also been proposed [Fleury et al., 2015], which is consistent with the patterns obtained with the quantitative analysis of the zebrafish gastrulation (topology of jet-vortexes motion in a fluid governed by a Poisson equation [1]). In this scenario, no local forces are needed to describe the topology, but the embryo could behave at this large scale as a fluid moving through the action of a large force exerted at a long distance. Thus, the effect of the force could hold due to a mass conservation principle in the fluid and the flow topology on one spatial point (such as the vortexes) could affect the whole embryo. On the other hand, the low magnitude of the motion compared to the cell size results in a low Reynolds number, so the flow described by the cell movements has no inertia. That property implies that the embryonic flow has no memory, so local forces could appear to control the shaping process locally as part of a whole regulatory mechanism. These hypothesis have to be properly quantified but are consistent with the instantaneous and cumulative deformation descriptions provided in chapter 5.

Overall, although the methodology proposed is just restricted to kinematics, the results obtained provide the first quantitatve multi-scale assessment of biomechanical patterning of the embryo beyond local tissue behavior, providing a systematic way to measure temporal multi-scale patterns in different levels of description.

7.2.4 Biological insight

The application of the framework to real data of embryogenesis led to biological insights. The study of the zebrafish gastrulation provided a new quantification of mechanical activity through stages of development revealing macroscopic traits due to large scale deformation undergone during gastrulation. These patterns were observed in a cohort of embryos but, given their high spatial and temporal complexity, they hampers to be compared as maps. The observation of these patterns through the trajectories revealed an incremental localization of mechanical activity in specific domains that we could identify with unsupervised classification techniques. The organization suggests a scale of organization comparable to the organization of the cell differentiation map (fate map), encouraging further investigation. A question that arises is which would be the role of mesoscopic mechanical activity in cell differentiation and its coordination or coupling with genetic patterns. More research has to be done in this direction to understand the interactions of genetics and mechanics in cell differentiation and in which length-scales and time intervals this combined interaction could really influence the differentiation process.

The study of the Drosophila's amnioserosa has confirmed previous research in the tissue, but the provided framework seems to allow a detail of description suitable to gain more insight. Best contri-

[1] Check this video for an example of a fluid jet: https://www.youtube.com/watch?v=zdI6OUJGZzU

bution has been to quantify a multi-scale coupling of mechanical behaviors (subcellular, cellular and supracellular scales) revealing that not only collective cell behavior give rise to the oscillatory contraction of the tissue, but mesoscopic constraints influence the mechanism. Further research is required to understand the timing hidden in this multi-scale mechanism as well as to formulate hypothesis and models that could be confronted with the kinematics analysis results.

7.3 Future work

This descriptive framework has the potential of being applied to numerous biological problems and the versatility will grow when better spatio-temporal data can be acquired. One of the most interesting lines of future research will be to apply this methodology to whole-embryo data so the meso-level mechanical characterizations can be compared among embryos,ensuring the selection of complete domains, and a canonical representation of embryo phenotypes can be statistically demonstrated. In that sense, it will be also possible to generate Lagrangian atlas of embryos, so information can be compared in terms of processes and not in terms of anatomical landmarks or instantaneous functional data difficult to cross-identify between embryos because of spatio-temporal variability.

Furthermore, the investigation of the most relevant length-scales will be necessary to observe the correlation between the dynamical structures and gene expression patterns. It can be assumed that mechanics will play an important role in the organization of the genetic patterns and this role should be analyzed in different spatio-temporal scales. Thus, this work encourages specific studies on phenotype comparison of mechanical, biomolecular and genetic patterns, so the main factors in phenotype differentiation can be quantified.

A deeper understanding of the levels and interactions of the mechanical factors in embryogenesis will be another important area of research. The meso-level organization of spatio-temporal dynamics in different stages and intervals of development emerges from force generation and force transduction mechanisms, so this description could be exploited to refine models and simulations of embryogenesis processes. In that sense, theoretical, methodological and experimental challenges will appear while trying to quantify the mechanical factors (see section 7.2.3) and to model how they organize to establish the patterning of embryogenesis, because it will be necessary to combine different scales of analysis along the development. Specially, the accurate and non-invasive measurement of stresses from *in-vivo* images will be necessary to convert multi-scale strain maps into a multi-scale force generation and communication mechanisms description.

In summary, an integrative research will require to determine the causality and the interplay between the mentioned mechanical factors, the biomolecular activity and the genetics in their different characteristic scales yet to be fully determined. From the results obtained in this Thesis, we could hypothesize that these mechanisms organize not only in short temporal scales, but also in long temporal

scales, so it will be necessary to build multi-level and multi-scale maps of interactions that eventually could explain the mechanisms that orchestrate the variable and robust morphogenesis of living systems.

Appendices

Appendix A

Mechanics formulation and theory

A.1 Tensors and tensors operations

A.1.1 Second order tensors

The tensors introduced in the presentation are generally defined as second order tensors. Specifically, the tensors describing the deformation of material points IDG and $FTDG$ are characterized in terms of the partial derivatives between the spatial vector $\mathbf{x_a}$ and the material vector $\mathbf{X_A}$, so the IDG tensor for each sample (material) point $\mathbf{x_i}$ can be more precisely defined as:

$$\mathbf{f}_t(\mathbf{x_i}) = \left(\frac{\partial x_a}{\partial X_A}\right)_{x_i} = \left(\frac{\partial \mathbf{x_a^{t+\Delta t}}}{\partial \mathbf{x_A^t}}\right)_{x_i}$$

expressing the instantaneous incremental deformation of the particle between t and $t + \Delta t$ (where we assumed that Δt is instantaneous). The $FTDG$ tensor would be then defined as:

$$\mathbf{F}(\mathbf{x_i}) = \mathbf{F_{aA}} = \left(\frac{\partial \mathbf{x_a}}{\partial \mathbf{X_A}}\right)_{x_i}$$

where $\mathbf{x_a}$ and $\mathbf{X_A}$ are the two positions of the particle in the finite-time interval limits.

A.1.2 Chain rule of interior product of tensors

The computation of the $FTDG$ tensor involves the interior product of the IDG tensors along time (here $[m-2, m]$) with the chain rule.

$$\mathbf{F}_{m-2}^{m} = \mathbf{f}_{m-1}\mathbf{f}_{m-2}$$

The chain rule involves a calculus relationship between the partial derivatives of the tensors:

$$\mathbf{F}_{m-2}^{m} == \frac{\partial \mathbf{x}_m}{\partial \mathbf{x}_{m-1}} \frac{\partial \mathbf{x}_{m-1}}{\partial \mathbf{x}_{m-2}}$$

As tensors, each operation is computed as an interior product of tensors (matrices):

$$\mathbf{AB} = A_{ip}B_{pj}$$

A.1.3 Principal components and invariants of tensors

The tensors are normally characterized with their principal components, calculated as the eigenvalues and eigenvectors of the matrix representing the tensor. These components provide information about the magnitude and the direction of the tensor components such as principal strain components. In $3D$ complex geometries, these components imply very difficult to interpret visualization tools (such as glyphs). Therefore, we will use scalar descriptors as principal invariants of the tensor that provide the quantitative description. Given the tensor $\mathbf{A}$, the principal invariants are defined as:

- First invariant: $I_1 = \text{tr}(A)$:
- Second invariant: $I_2 = \frac{1}{2}(\text{tr}^2(A) - \text{tr}(A^2)$
- Third invariant: $I_3 = \det(A)$

A.2 Eulerian and Lagrangian clarification

A.2.1 Definition

We define the different approaches of analysis as:

- Eulerian: Analysis of the dynamics from a spatial reference frame. Each sample is a spatial position. The dynamic system is defined by the streamlines (tangent lines of the vector field).
- Lagrangian: Analysis of the dynamics from a material reference frame. Each sample is a material point or particle moving. The dynamic system is defined by the pathlines (integrating the vector field).

In steady flows (do not change through time), streamlines and pathlines are the equivalent as all particles passing through a spatial point move in the same way.

Additionally, gradients are computed differently by an Eulerian definition which is normally used in fluid mechanics:

$$\frac{du(x,t)}{dt} = \frac{\partial u}{\partial t} + \frac{\partial u}{\partial x}\frac{\partial x}{\partial t};$$

and a Lagrangian one, normally used in solid mechanics:

$$\frac{du(X,t)}{dt} = \frac{\partial u}{\partial t}$$

A.2.2 Lagrangian framework

We proposed a generalized Lagrangian description of the embryo dynamics in comparison to an Eulerian characterization, meaning that we consider samples as material points that move forming the embryo. In that sense, our mechanics description is similar to continuum solids [Capaldi, 2012, Chadwick, 2012], but also to fluid analysis based on pathlines, such as the Lagrangian Coherent Structures formulation [Shadden et al., 2005, Peacock and Dabiri, 2010].

The displacements field calculated with image analysis techniques are normally computed as particle movement, through tracking or optical flow-like techniques. In that sense, all the deformation analysis is based on a Lagrangian (material) formulation. However, each time step is considered independently, so the material points are not treated as such, but as spatial points, so the instantaneous descriptor provided is classified as Eulerian.

Through the motion estimation description based on a differentiable vector field and a trajectory field, we fully define the embryo and tissue dynamics as a continuum under a Lagrangian framework, having a complete spatio-temporal map of material points along the interval of analysis that allows us to compute the deformation along several time intervals.

A.3 Infinitesimal Deformation

A.3.1 Infinitesimal deformation tensors

Under the assumption of high-temporal resolution for the phenomena observed, the instantaneous descriptors can be obtained from a linear decomposition of the IDG tensor $\mathbf{f_t}$ (or simply $\mathbf{f}$), as it is proposed in the bibliography [Helman and Hesselink, 1991]. We maintain these descriptors analogously to the descriptors used to characterize flows topology and strain rates.

The Incremental Gradient of Displacements -IGD- tensor $\mathbf{h} = \mathbf{f} - \mathbf{I}$ provides information of the topology of the deformation (equivalent to the velocity gradient if we consider instantaneous observation). This tensor contains complex eigenvalues indicating rotation rate and real components indicating linear deformation. The first principal invariant P provides information of the expansion and compression rate. In non-compressible flows $P = 0$, which is common for fluids, but in biological tissues P can take positive and negative values. The second invariant Q describes the behavior of the elongation and the rotation. In case $Q > 0$, the field rotates, but if $Q < 0$ the field deforms linearly. When $P = 0$ this invariant is a good indicator of the rotation rate. To better characterize this behavior we use the rotation discriminant D:

$$D = 27R^2 + (4P^3 - 18PQ)R + (4Q^3 - P^2Q^2) \tag{A.1}$$

This scalar provides very topological information of the invariants as $D = 0$ separates the clas-

sification of the field having complex eigenvalues or only real eigenvalues, so for high values of D it is possible to ensure that the field rotates because the magnitude of the complex eigenvalues is much larger than the magnitude of the real eigenvalues. Although D is a more sensitive descriptor (because of the high-order terms of eq. A.1) than Q, D is a better indicator of rotation than Q for compressible materials.

The shears are calculated from the symmetric part of $\mathbf{h}$, as the infinitesimal incremental strain tensor $\boldsymbol{\varepsilon}$ comprising the principal components of incremental strain of the field $\{e_1, e_2, e_3\}$ (strain rates in our assumption $\Delta t \to 0$.

$$\boldsymbol{\varepsilon} = \frac{1}{2}(\mathbf{h} + \mathbf{h}^{\mathbf{t}}) \tag{A.2}$$

This tensor in non compressible continuum provides information about shears using the second invariant Q_s, however in compressible continuum this descriptor also contains information about volume variations. In order to better study reconfigurations of the tissues seen as distortion, the deviatoric tensor $\mathbf{d}$ subtracts the volume changes (traceless symmetric tensor) forcing the first invariant to be 0.

$$\mathbf{d} = \boldsymbol{\varepsilon} - \frac{1}{3} tr(\boldsymbol{\varepsilon})\mathbf{I} \tag{A.3}$$

The eigenvalues $\{d_1, d_2, d_3\}$ and the invariant Q_d of this tensor provide information of the tissue or cell domains rearrangements induced by cell intercalation and shape changes.

The infinitesimal incremental rotation is extracted as the angular velocity and the axial vector associated to the skew-symmetric tensor $\boldsymbol{\Omega}$ of $\mathbf{h}$. The direction of the rotation in Cartesian components can be extracted as follows:

$$\boldsymbol{\Omega} = \begin{vmatrix} 0 & -w_3 & w_2 \\ w_3 & 0 & -w_1 \\ -w_2 & w_1 & 0 \end{vmatrix}.$$

where $\boldsymbol{\phi} = (w_1, w_2, w_3)$ defines the infinitesimal rotation vector $\mathbf{w}$ that provides a directionality of the rotation quantified with Q and D.

A.3.2 Infinitesimal deformation descriptors

Given a IDG tensor characterizing the deformation between time steps assuming $\Delta t \to 0$, we summarized the infinitesimal deformation descriptors calculations here:

- $P = \text{tr}(\mathbf{h})$
- $Q = \frac{1}{2}(\text{tr}^2(\mathbf{h}) - \text{tr}(\mathbf{h}^2)$
- $D = 27R^2 + (4P^3 - 18PQ)R + (4Q^3 - P^2Q^2)$ where $R = \det(\mathbf{h})$

- $Q_s = \frac{1}{2}(\text{tr}^2(\boldsymbol{\varepsilon}) - \text{tr}(\boldsymbol{\varepsilon}^2)$
- $\{e_1, e_2, e_3\} = eig(\boldsymbol{\varepsilon})$
- $Q_d = \frac{1}{2}(\text{tr}^2(\mathbf{d}) - \text{tr}(\mathbf{d}^2)$
- $\{d_1, d_2, d_3\} = eig(\mathbf{d})$
- $w = \|\mathbf{w}\|$

A.4 Finite deformation

A.4.1 Finite deformation tensors

The FTDG tensors can be arbitrarily large for a time interval $[t_n, t_m]$, so finite deformation tensors and desriptors formulation must be used to avoid characterization errors:

$$\mathbf{F} = \mathbf{RU} \tag{A.4}$$

where $\mathbf{R}$ is the finite rotation tensor (proper orthogonal tensor) and $\mathbf{U}$ the finite elongations tensor (positive definite symmetric tensor). To obtain these two matrices is necessary to perform the right polar decomposition of $\mathbf{F}$ (unique decomposition). First, we obtain the *Cauchy-Green* (CG) tensors which are rotation-free tensors:

$$RightCGtensor : \mathbf{C} = \mathbf{F}^T\mathbf{F} \tag{A.5}$$

$$LeftCGtensor : \mathbf{B} = \mathbf{F}\mathbf{F}^T \tag{A.6}$$

Eigenvalues between 0 and 1 stand for shrinking principal components whereas eigenvalues > 1 are the extension principal components. The tensor $\mathbf{C}$ has principal components in the same principal directions than the tensor $\mathbf{U}$ and their determinants keep a quadratic relationship $\det(\mathbf{C}) = \det(\mathbf{U}^2) = \det(\mathbf{F}^2)) = J^2$. The third invariant (determinant) J is the descriptor of volumetric changes for finite-time deformation. Then, the tensor $\mathbf{U}$ can be computed as described in [Simo and Hughes, 2006, Chadwick, 2012]:

- First, the eigenvalues of $\mathbf{C}\{e_1, e_2, e_3\}$ are extracted to obtain the invariants $\{i_1, i_2, i_3\}$:

$$I_1 = e_1 + e_2 + e_3 \; I_2 = e_1e_2 + e_1e_3 + e_2e_3 \; I_3 = e_1e_2e_3$$

- Then, $\mathbf{U}$ is calculated as:

$$\mathbf{U} = \frac{1}{A}[-\mathbf{C}^2 + (I_1^2 - I_2)\mathbf{C} + I_1 I_3 \mathbf{I}]$$

  where $A = I_1 I_2 - I_3$ and $\mathbf{I}$ is the identity matrix.

- Then, we can simply isolate the tensor $\mathbf{R}$ from:

$$\mathbf{R} = \mathbf{F}\mathbf{U}^{-1} \tag{A.7}$$

This rotation tensor allows us to express the rotation, according to Euler's theorem, by an angle rotation θ and the axis of rotation $\mathbf{n}$ that will be evolving through time:

$$\cos\theta = \frac{\mathrm{tr}R - 1}{2} \tag{A.8}$$

where $\mathbf{w_1}$ and $\mathbf{w_2}$ are the eigenvectors of the complex eigenvalues of $\mathbf{R}$.

The finite strain tensors can be obtained from the *Cauchy-Green* tensors allowing us to express the strains in the material coordinates getting the *Lagrange* finite strain tensor $\boldsymbol{\gamma}$:

$$\boldsymbol{\gamma} = \frac{1}{2}(\mathbf{C} - \mathbf{I}) \tag{A.9}$$

or in the spatial coordinates obtaining the *Almansi-Euler* finite strain tensor $\boldsymbol{\eta}$:

$$\boldsymbol{\eta} = \frac{1}{2}(\mathbf{I} - \mathbf{B}^{-1}) \tag{A.10}$$

These tensors are therefore a normalized version of the Cauchy-Green tensors.

Deformation can produce a volumetric change (J) and also to the distortion of the material. In order to isolate those behaviors, the gradient of isochoric deformation tensor may be also computed, whose eigenvalues $\{ic_1\, ic_2\, ic_3\}$ represent the deformation free of volume changes undergone by the continuum, related specially to the shears.

$$\tilde{\mathbf{F}} = J^{-1/3}\mathbf{F} \text{ where } \det(\tilde{\mathbf{F}}) = 1 \tag{A.11}$$

The first and second invariants of the *Cauchy-Green* tensor $\tilde{\mathbf{C}}$ derived from here $\tilde{\mathbf{F}}$ ($MIC1$ and $MIC2$) give the information about the tissue distortion along a finite time interval.

The $FTLE$ field has been used in fluids to obtain Lagrangian Coherent Structures $LCSs$ [Peacock and Haller, 2013, Shadden et al., 2005, Haller, 2001]. In non-compressible flows, this field shows the transport boundaries of the flow as lines of high-intensity values of the field (ridges). The $LCSs$ are defined as regions where there is no flux crossing them, therefore, the topology of the flow in the

$LCSs$ is a saddle point, line or plane stable through time. This field is derived from the Green-Cauchy right tensor $\mathbf{C}$ and its eigenvalues $\{c_i\}$ within an interval of time $[t_n\, t_m]$ ($T = t_m - t_n$) as follows:

$$FTLE:\ \sigma_n^m = \frac{1}{T}\ln(\sqrt{\max(c_i)}) \tag{A.12}$$

For compressible flows ($J \neq 1$) the interpretation of the $FTLE$ also conveys density changes along time. This phenomenon thickens the $FTLE$ ridges and introduces uncertainty about the presence of flux through the LCS. To isolate both behaviors and enforce the absence of flux through the LCS, we calculated the $isoFTLE$ for the isochoric deformation tensor $\tilde{\mathbf{F}}$ and its Cauchy-Green associated tensor $\tilde{\mathbf{C}}$. By applying the expression eq. A.12 over the eigenvalues derived from $\tilde{\mathbf{C}}$, we obtain the isochoric $FTLE$ field $\tilde{\sigma}_n^m$. The ridges of this field are LCS that are not crossed by any flux. The $FTLE$ field as calculated in A.12 contains repelling structures that separate the flow at both sides of the $FTLE$ ridges. The attracting structures are calculated in a similar way with the backward tracking. As the trajectories have to be complete and consistent, the same trajectory field is used, but the chain rule operates with the inverse of the gradient of incremental deformation. Thus, the backward $bFTLE$ and backward isochoric $ibFTLE$ can be derived from the same trajectory field. Combining forward and backwards description, it is possible to categorize zones of relaxation ($FTLE$) and repelling behavior ($iFTLE$) or attracting behavior ($ibFTLE$) and contraction ($bFTLE$).

A.4.2 Finite deformation descriptors

Given a FTDG tensor for a finite time interval of time $\mathbf{F}$, we summarized the finite deformation descriptors calculations here:

- $J = \det(\mathbf{F})$
- $MIC1 = \text{tr}(\tilde{\mathbf{C}})$
- $MIC2 = \frac{1}{2}(\text{tr}^2(\tilde{\mathbf{C}}) - \text{tr}(\tilde{\mathbf{C}}^2)$
- $\theta = \arccos(\frac{\text{tr}(\mathbf{R})-1}{2})$ and $\mathbf{n} = \mathbf{w_1} \times \mathbf{w_2}$
- $FTLE:\ \sigma_n^m = \frac{1}{T}\ln(\sqrt{\max(c_i)})$
- $iFTLE:\ \sigma_n^{\tilde{m}} = \frac{1}{T}\ln(\sqrt{\max(ic_i)})$

PUBLICATIONS

Journal papers

Pastor-Escuredo, D., Savy, T., Lombardot, B., Boyreau, A., Goicolea, J.M., Bourgine, P., Santos, A., del Alamo, J.C., Peyriéras, N., Ledesma-Carbayo, M.J. “Order and coherence of mechanical patterning in the zebrafish gastrulation”. (submitted to Science)

Pastor-Escuredo, D. et al. “Multi-scale characterization of the oscillatory contractions of the Drosophila’s amnioserosa”. (in preparation)

Rossini, L., Martinez-Legazpi, P., Vu, V., Fernández-Friera, L., Perez del Villar, C., Rodríguez-López, S., Benito, Y., Borja, M-G., Pastor-Escuredo, D., Yotti, R., Ledesma-Carbayo, M.J. , Kahn, A.M., Ibanez, B., Fernández-Avilés, F., May-Newman, K., Bermejo, J., del Alamo, J.C. “A Clinical Method for Mapping and Quantifying Blood Stasis in the Left Ventricle”. J. Biomech.In Press, 2015.

Maška, M., Ulman, V., Svoboda, D., Matula, P., Matula, P., Ederra, C., Urbiola, A., España, T., Venkatesan, S., Balak, D.M.W., Karas, P., Bolcková, T., Štreitová, M., Carthel, C., Coraluppi, S., Harder, N., Rohr, K., Magnusson, K.E.G., Jaldén, J., Blau, H.M., Dzyubachyk, O., Krížek, P., Hagen, G.M., Pastor-Escuredo, D., Jimenez-Carretero, D., Ledesma-Carbayo, M.J., Muñoz-Barrutia, A., Meijering, E., Kozubek, M., Ortiz-de-Solorzano, C. “A benchmark for comparison of cell tracking algorithms”. Bioinformatics, 30(11):1609-1617. Jun. 2014 (doi: 10.1093/bioinformatics/btu080).

García-Álvarez, A., Fernández-Friera, L., García-Ruiz, J.M., Nuño-Ayala, M., Pereda, D., Fernández-Jiménez, R., Guzmán, G., Sanchez-Quintana, D., Alberich-Bayarri, A., Pastor-Escudero, D., Sanz-Rosa, D., García-Prieto, J., Gonzalez-Mirelis, J.G., Pizarro, G., Jimenez-Borreguero, L.J., Fuster, V., Sanz, J., Ibáñez, B. “ Noninvasive Monitoring of Serial Changes in Pulmonary Vascular Resistance and Acute Vasodilator Testing Using Cardiac Magnetic Resonance” Journal American College Cardiology, 62(17):1621-1631. Oct. 2013 (doi: 10.1016/j.jacc.2013.07.037).

Luengo-Oroz, M.A., Pastor-Escuredo, D., Castro-Gonzalez, C., Faure, E., Savy, T., Lombardot, B., Rubio-Guivernau, J.L., Duloquin, L., Ledesma-Carbayo, M.J., Bourgine, P., Peyrieras, N., Santos, A. “3D+t Morphological Processing: Applications to Embryogenesis Image Analysis”. IEEE Trans. Image Process., 21(8):3518-3530. Aug. 2012 (doi: 10.1109/TIP.2012.2197007).

Luengo-Oroz, M.A., Rubio-Guivernau, J.L., Faure, E., Savy, T., Duloquin, L., Olivier, N., Pastor-Escuredo, D., Ledesma-Carbayo, M.J., Débarre, D., Bourgine, P., Beaurepaire, E., Peyriéras, N., Santos, A. "Methodology for Reconstructing Early Zebrafish Development From In Vivo Multiphoton Microscopy". IEEE Trans. Image Process., 21(4):2335-2340. Apr. 2012 (doi: 10.1109/TIP.2011.2177911).

Conferences

Pastor-Escuredo, D., Luengo-Oroz, M.A., Duloquin, L., Lombardot, B., Ledesma-Carbayo, M., Bourgine, P., Peyrieras, N., Santos, A. “Spatio-Temporal Filtering with Morphological Operators for Robust Cell Migration Estimation in in-vivo Images”. IEEE International Symposium on Biomedical Imaging: From Nano to Macro (ISBI 2012), pp. 1312-1315. Barcelona (Spain), May 2012 (doi: 10.1109/ISBI.2012.6235804).

Pastor-Escuredo, D., Luengo-Oroz, M.A., Lombardot, B., Gonzálvez, I., Duloquin, L., Savy, T., Bourgine, P., Peyriéras, N., Santos, A. "Cell tracking in fluorescence images of embryogenesis processes with morphological reconstruction by 4D-tubular structuring elements". Proc 31st Annual International IEEE EMBS Conference, pp. 970-973. Minneapolis (MN, USA), Sep. 2009 (doi: 10.1109/IEMBS.2009.5333756).

Bibliography

F. Amat, W. Lemon, D. Mossing, K. McDole, Y. Wan, K. Branson, E. Myers, and P. Keller. Fast, accurate reconstruction of cell lineages from large-scale fluorescence microscopy data. *Nature methods*, 11(9):951, 2014.

J. C. Arciero, Q. Mi, M. F. Branca, D. J. Hackam, and D. Swigon. Continuum model of collective cell migration in wound healing and colony expansion. *Biophysical Journal*, 100(3):535–543, 2011.

A. Asnacios and O. Hamant. The mechanics behind cell polarity. *Trends in cell biology*, 22(11): 584–591, 2012.

D. Azevedo, M. Antunes, S. Prag, X. Ma, U. Hacker, G. W. Brodland, M. S. Hutson, J. Solon, and A. Jacinto. Drhogef2 regulates cellular tension and cell pulsations in the amnioserosa during drosophila dorsal closure. *PloS one*, 6(9):e23964, 2011.

M. Behrndt, G. Salbreux, P. Campinho, R. Hauschild, F. Oswald, J. Roensch, S. W. Grill, and C.-P. Heisenberg. Forces driving epithelial spreading in zebrafish gastrulation. *Science*, 338(6104): 257–260, 2012.

Y. Bellaiche, F. Bosveld, F. Graner, K. Mikula, M. Remesikova, and M. Smisek. New robust algorithm for tracking cells in videos of drosophila morphogenesis based on finding an ideal path in segmented spatio-temporal cellular structures. In *Engineering in Medicine and Biology Society, EMBC, 2011 Annual International Conference of the IEEE*, pages 6609–6612. IEEE, 2011.

C. Bertet, L. Sulak, and T. Lecuit. Myosin-dependent junction remodelling controls planar cell intercalation and axis elongation. *Nature*, 429(6992):667–671, 2004.

G. B. Blanchard and R. J. Adams. Measuring the multi-scale integration of mechanical forces during morphogenesis. *Current opinion in genetics and development*, 21(5):653–663, 2011.

G. B. Blanchard, A. J. Kabla, N. L. Schultz, L. C. Butler, B. Sanson, N. Gorfinkiel, L. Mahadevan, and R. J. Adams. Tissue tectonics: morphogenetic strain rates, cell shape change and intercalation. *Nature Methods*, 6(6):458–464, 2009.

G. B. Blanchard, S. Murugesu, R. J. Adams, A. Martinez-Arias, and N. Gorfinkiel. Cytoskeletal dynamics and supracellular organisation of cell shape fluctuations during dorsal closure. *Development*, 137(16):2743–2752, 2010.

N. R. Blum, H. N. Rosen, and G. Levkowitz. High resolution fate map of the zebrafish diencephalon. *Developmental Dynamics*, 238(7):1827–1835, 2009.

F. Bosveld, I. Bonnet, B. Guirao, S. Tlili, Z. Wang, A. Petitalot, R. Marchand, P.-L. Bardet, P. Marcq, F. Graner, et al. Mechanical control of morphogenesis by fat/dachsous/four-jointed planar cell polarity pathway. *Science*, 336(6082):724–727, 2012.

T. Brend and S. A. Holley. Zebrafish whole mount high-resolution double fluorescent in situ hybridization. *Journal of visualized experiments: JoVE*, (25), 2009.

G. W. Brodland, V. Conte, P. G. Cranston, J. Veldhuis, S. Narasimhan, M. S. Hutson, A. Jacinto, F. Ulrich, B. Baum, and M. Miodownik. Video force microscopy reveals the mechanics of ventral furrow invagination in drosophila. *Proceedings of the National Academy of Sciences*, 107(51): 22111–22116, 2010.

G. W. Brodland, J. H. Veldhuis, S. Kim, M. Perrone, D. Mashburn, and M. S. Hutson. Cellfit: A cellular force-inference toolkit using curvilinear cell boundaries. *PLoS ONE*, 9(6), 2014.

C. G. Burns, D. J. Milan, E. J. Grande, W. Rottbauer, C. A. MacRae, and M. C. Fishman. High-throughput assay for small molecules that modulate zebrafish embryonic heart rate. *Nature chemical biology*, 1(5):263–264, 2005.

O. Campas, T. Mammoto, S. Hasso, R. A. Sperling, D. O'Connell, A. G. Bischof, R. Maas, D. A. Weitz, L. Mahadevan, and D. E. Ingber. Quantifying cell-generated mechanical forces within living embryonic tissues. *Nature methods*, 11(2):183–189, 2014.

P. Campinho, M. Behrndt, J. Ranft, T. Risler, N. Minc, and C.-P. Heisenberg. Tension-oriented cell divisions limit anisotropic tissue tension in epithelial spreading during zebrafish epiboly. *Nature cell biology*, 15(12):1405–1414, 2013.

F. M. Capaldi. *Continuum mechanics: constitutive modeling of structural and biological materials*. Cambridge University Press, 2012.

C. Castro-González, M. Luengo-Oroz, L. Douloquin, T. Savy, C. Melani, S. Desnoulez, M. Ledesma-Carbayo, P. Bourgine, N. Peyriéras, and A. Santos. Towards a digital model of zebrafish embryogenesis. Integration of cell tracking and gene expression quantification. In *Proc. IEEE EMBS Conference*, pages 5520–5523, 2010.

C. Castro-González, M. A. Luengo-Oroz, L. Duloquin, T. Savy, B. Rizzi, S. Desnoulez, R. Doursat, Y. L. Kergosien, M. J. Ledesma-Carbayo, P. Bourgine, et al. A digital framework to build, visualize and analyze a gene expression atlas with cellular resolution in zebrafish early embryogenesis. *PLoS Computational Biology*, 10(6):e1003670, 2014.

P. Chadwick. *Continuum mechanics: concise theory and problems*. Courier Corporation, 2012.

F. D. Chaumont, S. Dallongeville, N. Chenouard, N. Herve, S. Pop, T. Provoost, V. Meas-Yedid, P. Pankajakshan, T. Lecomte, and Y. L. Montagner. Icy: an open bioimage informatics platform for extended reproducible research. *Nature methods*, 9(7):690–696, 2012.

K. K. Chiou, L. Hufnagel, and B. I. Shraiman. Mechanical stress inference for two dimensional cell arrays. *PLoS Comput Biol*, 8(5):e1002512, 2012.

D. M. Chudakov, M. V. Matz, S. Lukyanov, and K. A. Lukyanov. Fluorescent proteins and their applications in imaging living cells and tissues. *Physiological reviews*, 90(3):1103–1163, 2010.

D. J. David, A. Tishkina, and T. J. Harris. The par complex regulates pulsed actomyosin contractions during amnioserosa apical constriction in drosophila. *Development*, 137(10):1645–1655, 2010.

L. Davidson, M. von Dassow, and J. Zhou. Multi-scale mechanics from molecules to morphogenesis. *The international journal of biochemistry and cell biology*, 41(11):2147–2162, 11 2009.

R. Doursat. The self-made puzzle: integrating self-assembly and pattern formation under nonrandom genetic regulation. In *Int. J. Complex Syst*, page 2292, 2008.

E. Faure et al. An algorithmic workflow for the automated processing of 3D+time microscopy images of developing organisms and the reconstruction of their cell lineage. *Nature Communications (in press)*, 2015.

S. J. England, G. B. Blanchard, L. Mahadevan, and R. J. Adams. A dynamic fate map of the forebrain shows how vertebrate eyes form and explains two causes of cyclopia. *Development*, 133(23):4613–4617, 2006.

R. Farhadifar, J.-C. Roper, B. Aigouy, S. Eaton, and F. Julicher. The influence of cell mechanics, cell-cell interactions, and proliferation on epithelial packing. *Current Biology*, 17(24):2095–2104, 2007.

R. Fernandez, P. Das, V. Mirabet, E. Moscardi, J. Traas, J. Verdeil, G. Malandain, and C. Godin. Imaging plant growth in 4D: robust tissue reconstruction and lineaging at cell resolution. *Nature Methods*, 7(7):547–553, 2010.

A. G. Fletcher, M. Osterfield, R. E. Baker, and S. Y. Shvartsman. Vertex models of epithelial morphogenesis. *Biophysical journal*, 106(11):2291–2304, 2014.

V. Fleury, N. R. Chevalier, F. Furfaro, and J.-L. Duband. Buckling along boundaries of elastic contrast as a mechanism for early vertebrate morphogenesis. *The European Physical Journal E*, 38(2):1–19, 2015.

C. C. Fowlkes, C. L. L. Hendriks, S. V. Keranen, G. H. Weber, O. Rubel, M.-Y. Huang, S. Chatoor, A. H. DePace, L. Simirenko, and C. Henriquez. A quantitative spatiotemporal atlas of gene expression in the drosophila blastoderm. *Cell*, 133(2):364–374, 2008.

L. Gao, L. Shao, C. D. Higgins, J. S. Poulton, M. Peifer, M. W. Davidson, X. Wu, B. Goldstein, and E. Betzig. Noninvasive imaging beyond the diffraction limit of 3D dynamics in thickly fluorescent specimens. *Cell*, 151(6):1370–1385, 2012.

L. Gao, L. Shao, B.-C. Chen, and E. Betzig. 3D live fluorescence imaging of cellular dynamics using bessel beam plane illumination microscopy. *Nature Protocols*, 9(5):1083–1101, 2014.

N. S. Glickman, C. B. Kimmel, M. A. Jones, and R. J. Adams. Shaping the zebrafish notochord. *Development*, 130(5):873–887, 2003.

N. Gorfinkiel. Mechano-chemical coupling drives cell area oscillations during morphogenesis. *Biophysical journal*, 104(1):1–3, 2013.

N. Gorfinkiel and G. B. Blanchard. Dynamics of actomyosin contractile activity during epithelial morphogenesis. *Current opinion in cell biology*, 23(5):531–539, 2011.

N. Gorfinkiel, G. B. Blanchard, R. J. Adams, and A. M. Arias. Mechanical control of global cell behaviour during dorsal closure in drosophila. *Development*, 136(11):1889, 2009.

N. Gorfinkiel, S. Schamberg, and G. B. Blanchard. Integrative approaches to morphogenesis: lessons from dorsal closure. *Genesis*, 49(7):522–533, 2011.

F. Graner, B. Dollet, C. Raufaste, and P. Marmottant. Discrete rearranging disordered patterns, part i: Robust statistical tools in two or three dimensions. *The European Physical Journal E*, 25(4): 349–369, 2008.

C. Guillot and T. Lecuit. Mechanics of epithelial tissue homeostasis and morphogenesis. *Science*, 340 (6137):1185–1189, 2013.

A. Haeger, K. Wolf, M. M. Zegers, and P. Friedl. Collective cell migration: guidance principles and hierarchies. *Trends in cell biology*, 25(9):556–566, 2015.

M. S. Hall, R. Long, X. Feng, Y. Huang, C.-Y. Hui, and M. Wu. Toward single cell traction microscopy within 3D collagen matrices. *Experimental cell research*, 319(16):2396–2408, 2013.

G. Haller. Distinguished material surfaces and coherent structures in three-dimensional fluid flows. *Physica D: Nonlinear Phenomena*, 149(4):248–277, 2001.

C.-P. Heisenberg and Y. Bellaïche. Forces in tissue morphogenesis and patterning. *Cell*, 153(5): 948–962, 2013.

J. L. Helman and L. Hesselink. Visualizing vector field topology in fluid flows. *Computer Graphics and Applications, IEEE*, 11(3):36–46, 1991.

S. Herszterg, A. Leibfried, F. Bosveld, C. Martin, and Y. Bellaiche. Interplay between the dividing cell and its neighbors regulates adherens junction formation during cytokinesis in epithelial tissue. *Developmental cell*, 24(3):256–270, 2013.

A. J. Hill, H. Teraoka, W. Heideman, and R. E. Peterson. Zebrafish as a model vertebrate for investigating chemical toxicity. *Toxicological sciences*, 86(1):6–19, 2005.

M. S. Hutson and X. Ma. Plasma and cavitation dynamics during pulsed laser microsurgery in vivo. *Physical Review Letters*, 99(15):158104, 2007.

M. S. Hutson, Y. Tokutake, M.-S. Chang, J. W. Bloor, S. Venakides, D. P. Kiehart, and G. S. Edwards. Forces for morphogenesis investigated with laser microsurgery and quantitative modeling. *Science*, 300(5616):145–149, 2003.

S. Ishihara and K. Sugimura. Bayesian inference of force dynamics during morphogenesis. *Journal of theoretical biology*, 313:201–211, 2012.

S. Ishihara, K. Sugimura, S. Cox, I. Bonnet, Y. Bellaiche, and F. Graner. Comparative study of non-invasive force and stress inference methods in tissue. *The European Physical Journal E*, 36(4): 1–13, 2013.

J. R. Jessen, J. Topczewski, S. Bingham, D. S. Sepich, F. Marlow, A. Chandrasekhar, and L. Solnica-Krezel. Zebrafish trilobite identifies new roles for strabismus in gastrulation and neuronal movements. *Nature cell biology*, 4(8):610–615, 2002.

E. Jonietz. Mechanics: The forces of cancer. *Nature*, 491(7425):S56–S57, 2012.

K. E. Kasza and J. A. Zallen. Dynamics and regulation of contractile actin-myosin networks in morphogenesis. *Current opinion in cell biology*, 23(1):30–38, 2011.

K. E. Kasza, D. L. Farrell, and J. A. Zallen. Spatiotemporal control of epithelial remodeling by regulated myosin phosphorylation. *Proceedings of the National Academy of Sciences*, 111(32): 11732–11737, 2014.

R. D. Keane and R. J. Adrian. Theory of cross-correlation analysis of piv images. *Applied scientific research*, 49(3):191–215, 1992.

P. J. Keller. Imaging morphogenesis: Technological advances and biological insights. *Science*, 340 (6137):1234168, 2013.

P. J. Keller and M. B. Ahrens. Visualizing whole-brain activity and development at the single-cell level using light-sheet microscopy. *Neuron*, 85(3):462–483, 2015.

P. J. Keller and E. H. K. Stelzer. Quantitative in vivo imaging of entire embryos with digital scanned laser light sheet fluorescence microscopy. *Current opinion in neurobiology*, 18(6):624–632, 2008.

P. J. Keller, A. D. Schmidt, J. Wittbrodt, and E. H. K. Stelzer. Reconstruction of zebrafish early embryonic development by scanned light sheet microscopy. *Science*, 322(5904):1065, 2008.

R. Keller. Physical biology returns to morphogenesis. *Science*, 338(6104):201–203, 2012.

R. Keller, L. Davidson, A. Edlund, T. Elul, M. Ezin, D. Shook, and P. Skoglund. Mechanisms of convergence and extension by cell intercalation. *Philosophical Transactions of the Royal Society of London.Series B: Biological Sciences*, 355(1399):897–922, 2000.

R. Keller, L. A. Davidson, and D. R. Shook. How we are shaped: the biomechanics of gastrulation. *Differentiation*, 71(3):171–205, 2003.

R. Kennaway, E. Coen, A. Green, and A. Bangham. Generation of diverse biological forms through combinatorial interactions between tissue polarity and growth. *PLoS computational biology*, 7(6): e1002071, 2011.

K. Khairy and P. Keller. Reconstructing embryonic development. *Genesis*, 49(7):488–513, 2011.

D. P. Kiehart, C. G. Galbraith, K. A. Edwards, W. L. Rickoll, and R. A. Montague. Multiple forces contribute to cell sheet morphogenesis for dorsal closure in drosophila. *The Journal of cell biology*, 149(2):471–490, 2000.

C. B. Kimmel, R. Warga, and T. Schilling. Origin and organization of the zebrafish fate map. *Development*, 108(4):581, 1990.

H. Kitano et al. Computational systems biology. *Nature*, 420(6912):206–210, 2002.

K. M. Kwan, H. Otsuna, H. Kidokoro, K. R. Carney, Y. Saijoh, and C.-B. Chien. A complex choreography of cell movements shapes the vertebrate eye. *Development*, 139(2):359–372, 2012.

J. Kybic and M. Unser. Fast parametric elastic image registration. *IEEE Trans. Image Proc.*, 12(11): 1427–1442, 2003.

T. Lecuit and P.-F. Lenne. Cell surface mechanics and the control of cell shape, tissue patterns and morphogenesis. *Nature Reviews Molecular Cell Biology*, 8(8):633–644, 2007.

T. Lecuit, P.-F. Lenne, and E. Munro. Force generation, transmission, and integration during cell and tissue morphogenesis. *Annual Review of Cell and Developmental Biology*, 27:157–184, 2011.

M. Ledesma-Carbayo, P. Mahia-Casado, A. Santos, E. Perez-David, M. Garcia-Fernandez, and M. Desco. Cardiac motion analysis from ultrasound sequences using nonrigid registration: validation against doppler tissue velocity. *Ultrasound in medicine biology*, 32(4):483–490, 2006.

M. J. Ledesma-Carbayo, J. Kybic, M. Desco, A. Santos, M. Suhling, P. Hunziker, and M. Unser. Spatio-temporal nonrigid registration for ultrasound cardiac motion estimation. *IEEE Transactions on Medical Imaging*, 24(9):1113–1126, 2005.

R. Levayer and T. Lecuit. Biomechanical regulation of contractility: spatial control and dynamics. *Trends in cell biology*, 22(2):61–81, 2012.

K. R. Levental, H. Yu, L. Kass, J. N. Lakins, M. Egeblad, J. T. Erler, S. F. Fong, K. Csiszar, A. Giaccia, and W. Weninger. Matrix crosslinking forces tumor progression by enhancing integrin signaling. *Cell*, 139(5):891–906, 2009.

F. Long, J. Zhou, and H. Peng. Visualization and Analysis of 3D Microscopic Images. *PLoS Computational Biology*, 8(6):e1002519, 2012.

M. Luengo-Oroz, M. Ledesma-Carbayo, N. Peyriéras, and A. Santos. Image analysis for understanding embryo development: a bridge from microscopy to biological insights. *Current Opinion in Genetics & Development*, 21(5):630–637, 2011.

M. A. Luengo-Oroz, D. Pastor-Escuredo, C. Castro-Gonzalez, E. Faure, T. Savy, B. Lombardot, J. L. Rubio-Guivernau, L. Duloquin, M. J. Ledesma-Carbayo, P. Bourgine, A. Santos, and N. Peyrieras. 3D+t Morphological Processing: Applications to Embryogenesis Image Analysis. *IEEE Transactions on Image Processing*, 21(8):3518–3530, 2012.

X. Ma, H. E. Lynch, P. C. Scully, and M. S. Hutson. Probing embryonic tissue mechanics with laser hole drilling. *Physical biology*, 6(3):036004, 2009.

P. Machado, J. Duque, J. Etienne, A. Martinez Arias, G. Blanchard, and N. Gorfinkiel. Emergent material properties of developing epithelial tissue. *BMC Biology*, in press.

P. F. Machado, G. B. Blanchard, J. Duque, and N. Gorfinkiel. Cytoskeletal turnover and myosin contractility drive cell autonomous oscillations in a model of drosophila dorsal closure. *The European Physical Journal Special Topics*, 223(7):1391–1402, 2014.

P. Mahou, J. Vermot, E. Beaurepaire, and W. Supatto. Multicolor two-photon light-sheet microscopy. *Nature methods*, 11(6):600–601, 2014.

J.-L. Maitre and C.-P. Heisenberg. Three functions of cadherins in cell adhesion. *Current Biology*, 23 (14):R626–R633, 2013.

A. C. Martin. Pulsation and stabilization: Contractile forces that underlie morphogenesis. *Developmental biology*, 341(1):114–125, 2010.

V. Maruthamuthu, B. Sabass, U. S. Schwarz, and M. L. Gardel. Cell-ECM traction force modulates endogenous tension at cell-cell contacts. *Proceedings of the National Academy of Sciences*, 108 (12):4708–4713, 2011.

M. Maška, V. Ulman, D. Svoboda, P. Matula, P. Matula, C. Ederra, A. Urbiola, T. España, S. Venkatesan, D. M. Balak, et al. A benchmark for comparison of cell tracking algorithms. *Bioinformatics*, 30(11):1609–1617, 2014.

M. L. McCain, H. Lee, Y. Aratyn-Schaus, A. G. Kléber, and K. K. Parker. Cooperative coupling of cell-matrix and cell–cell adhesions in cardiac muscle. *Proceedings of the National Academy of Sciences*, 109(25):9881–9886, 2012.

A. McMahon, W. Supatto, S. E. Fraser, and A. Stathopoulos. Dynamic analyses of drosophila gastrulation provide insights into collective cell migration. *Science*, 322(5907):1546–1550, 2008.

S. Megason, S. Srinivas, M. Dickinson, and A. Hadjantonakis. Microscopy to mechanism across the scales of development. *Current Opinion in Genetics & Development*, 21:519–522, 2011.

S. G. Megason. In toto imaging of embryogenesis with confocal time-lapse microscopy. *Methods Mol Biol*, 546:317–332, 2009.

S. G. Megason and S. E. Fraser. Digitizing life at the level of the cell: high-performance laser-scanning microscopy and image analysis for in toto imaging of development. *Mechanisms of development*, 120(11):1407–1420, 2003.

S. G. Megason and S. E. Fraser. Imaging in systems biology. *Cell*, 130(5):784–795, 2007.

E. Meijering, O. Dzyubachyk, I. Smal, and W. A. van Cappellen. Tracking in cell and developmental biology. *Seminars in cell and developmental biology*, 20(8):894–902, 2009.

E. Meijering, O. Dzyubachyk, and I. Smal. Methods for cell and particle tracking. *Methods Enzymol*, 504(9):183–200, 2012.

F. Meyer. Iterative image transformations for an automatic screening of cervical smears. *Journal of Histochemistry and Cytochemistry*, 27(1):128, 1979.

R. Mikut, T. Dickmeis, W. Driever, P. Geurts, F. A. Hamprecht, B. X. Kausler, M. J. Ledesma-Carbayo, R. Marée, K. Mikula, P. Pantazis, et al. Automated processing of zebrafish imaging data: a survey. *Zebrafish*, 10(3):401–421, 2013.

A. Munjal and T. Lecuit. Actomyosin networks and tissue morphogenesis. *Development*, 141(9): 1789–1793, 2014.

A. C. Oates, N. Gorfinkiel, M. Gonzalez-Gaitan, and C. P. Heisenberg. Quantitative approaches in developmental biology. *Nature Reviews Genetics*, 10(8):517–530, 2009.

T. Oliver, K. Jacobson, and M. Dembo. Design and use of substrata to measure traction forces exerted by cultured cells. *Methods in enzymology*, 298:497–521, 1998.

N. Olivier, M. A. Luengo-Oroz, L. Duloquin, E. Faure, T. Savy, I. Veilleux, X. Solinas, D. Debarre, P. Bourgine, A. Santos, N. Peyrieras, and E. Baurepaire. Cell lineage reconstruction of early zebrafish embryos using label-free nonlinear microscopy. *Science*, 329(5994):967–971, 2010.

F. Pampaloni, B.-J. Chang, and E. H. Stelzer. Light sheet-based fluorescence microscopy (lsfm) for the quantitative imaging of cells and tissues. *Cell and tissue research*, 360(1):129–141, 2015.

P. Pantazis and W. Supatto. Advances in whole-embryo imaging: a quantitative transition is underway. *Nature Reviews Molecular Cell Biology*, 15(5):327–339, 2014.

A. Paré, A. Vichas, C. Fincher, Z. Mirman, D. Farrell, A. Mainieri, and J. Zallen. A positional toll receptor code directs convergent extension in drosophila. *Nature*, 515(7528):523, 2014.

D. Pastor, M. Luengo-Oroz, B. Lombardot, I. Gonzalvez, L. Duloquin, T. Savy, P. Bourgine, N. Peyrieras, and A. Santos. Cell tracking in fluorescence images of embryogenesis processes with morphological reconstruction by 4d-tubular structuring elements. In *Engineering in Medicine and Biology Society, 2009. EMBC 2009. Annual International Conference of the IEEE*, pages 970–973. IEEE, 2009.

D. Pastor-Escuredo, M. A. Luengo-Oroz, L. Duloquin, B. Lombardot, M. Ledesma-Carbayo, P. Bourgine, N. Peyrieras, and A. Santos. Spatio temporal filtering with morphological operators for robust cell migration estimation in in vivo images. In *Biomedical Imaging (ISBI), 2012 9th IEEE International Symposium on*, pages 1312–1315. IEEE, 2012.

J. B. Pawley and B. R. Masters. Handbook of biological confocal microscopy. *Journal of Biomedical Optics*, 13:029902, 2008.

T. Peacock and J. Dabiri. Introduction to focus issue: Lagrangian coherent structures. *Chaos: An Interdisciplinary Journal of Nonlinear Science*, 20(1):017501–017501–3, 2010.

T. Peacock and G. Haller. Lagrangian coherent structures: The hidden skeleton of fluid flows. *Physics Today*, 66(2):41–47, 2013.

H. Peng. Bioimage informatics: a new area of engineering biology. *Bioinformatics*, 24(17):1827, 2008.

H. Peng, P. Chung, F. Long, L. Qu, A. Jenett, A. M. Seeds, E. W. Myers, and J. H. Simpson. Brainaligner: 3D registration atlases of drosophila brains. *Nature Methods*, 8(6):493–498, 2011.

T. Pietzsch, S. Saalfeld, S. Preibisch, and P. Tomancak. Bigdataviewer: visualization and processing for large image data sets. *Nature Methods*, 12(6):481–483, 2015.

D. Potikanond and F. Verbeek. Visualization and analysis of 3D gene expression patterns in zebrafish using web services. In *IST/SPIE Electronic Imaging*, pages 829412–829412–11. International Society for Optics and Photonics, 2012.

S. Preibisch, T. Rohlfing, M. P. Hasak, and P. Tomancak. Mosaicing of single plane illumination microscopy images using groupwise registration and fast content-based image fusion. In *Medical Imaging*, pages 69140E–69140E–8. International Society for Optics and Photonics, 2008.

M. Rauzi, P. Verant, T. Lecuit, and P.-F. Lenne. Nature and anisotropy of cortical forces orienting drosophila tissue morphogenesis. *Nature cell biology*, 10(12):1401–1410, 2008.

M. Rauzi, P.-F. Lenne, and T. Lecuit. Planar polarized actomyosin contractile flows control epithelial junction remodelling. *Nature*, 468(7327):1110–1114, 2010.

J. Rittscher, D. Padfield, A. Santamaria, J. Tu, A. Can, M. Bello, D. Gao, A. Sood, M. Gerdes, and F. Ginty. Methods and algorithms for extracting high-content signatures from cells, tissues, and model organisms. In *Biomedical Imaging: From Nano to Macro, 2011 IEEE International Symposium on*, pages 1712–1716. IEEE, 2011.

T. Rohlfing, C. R. Maurer Jr, D. A. Bluemke, and M. A. Jacobs. Volume-preserving nonrigid registration of mr breast images using free-form deformation with an incompressibility constraint. *IEEE Transactions on Medical Imaging*, 22(6):730–741, 2003.

O. Ronneberger, K. Liu, M. Rath, D. Ruess, T. Mueller, H. Skibbe, B. Drayer, T. Schmidt, A. Filippi, and R. Nitschke. Vibe-z: a framework for 3D virtual colocalization analysis in zebrafish larval brains. *Nature Methods*, 9(7):735–742, 2012.

J. L. Rubio-Guivernau, V. Gurchenkov, M. A. Luengo-Oroz, L. Duloquin, P. Bourgine, A. Santos, N. Peyrieras, and M. J. Ledesma-Carbayo. Wavelet-based image fusion in multi-view three-dimensional microscopy. *Bioinformatics*, 28(2):238–245, 2012.

S. Saraçli, N. Doğan, and İ. Doğan. Comparison of hierarchical cluster analysis methods by cophenetic correlation. *Journal of Inequalities and Applications*, 2013(1):1–8, 2013.

B. Schmid, G. Shah, N. Scherf, M. Weber, K. Thierbach, C. P. Campos, I. Roeder, P. Aanstad, and J. Huisken. High-speed panoramic light-sheet microscopy reveals global endodermal cell dynamics. *Nature*, 4(2207), 2013.

S. C. Shadden, F. Lekien, and J. E. Marsden. Definition and properties of lagrangian coherent structures from finite-time lyapunov exponents in two-dimensional aperiodic flows. *Physica D: Nonlinear Phenomena*, 212:271–304, 2005.

M. J. Siedlik and C. M. Nelson. Regulation of tissue morphodynamics: an important role for actomyosin contractility. *Current opinion in genetics and development*, 32:80–85, 2015.

J. C. Simo and T. J. Hughes. *Computational inelasticity*, volume 7. Springer Science & Business Media, 2006.

A. Sokolow, Y. Toyama, D. P. Kiehart, and G. S. Edwards. Cell ingression and apical shape oscillations during dorsal closure in drosophila. *Biophysical journal*, 102(5):969–979, 2012.

J. Solon, A. Kaya-Copur, J. Colombelli, and D. Brunner. Pulsed forces timed by a ratchet-like mechanism drive directed tissue movement during dorsal closure. *Cell*, 137(7):1331–1342, 2009.

C. O. Sorzano, P. Thevenaz, and M. Unser. Elastic registration of biological images using vector-spline regularization. *IEEE Transactions on Biomedical Engineering*, 52(4):652–663, 2005.

T. Stearns. Green flourescent protein: The green revolution. *Current Biology*, 5(3):262–264, 1995.

W. Supatto, A. McMahon, S. E. Fraser, and A. Stathopoulos. Quantitative imaging of collective cell migration during drosophila gastrulation: multiphoton microscopy and computational analysis. *Nature protocols*, 4(10):1397–1412, 2009.

W. Supatto, T. V. Truong, D. Débarre, and E. Beaurepaire. Advances in multiphoton microscopy for imaging embryos. *Current opinion in genetics & development*, 21(5):538–548, 2011.

D. T. Tambe, C. C. Hardin, T. E. Angelini, K. Rajendran, C. Y. Park, X. Serra-Picamal, E. H. Zhou, M. H. Zaman, J. P. Butler, and D. A. Weitz. Collective cell guidance by cooperative intercellular forces. *Nature materials*, 10(6):469–475, 2011.

M. Tawk, C. Araya, D. A. Lyons, A. M. Reugels, G. C. Girdler, P. R. Bayley, D. R. Hyde, M. Tada, and J. D. Clarke. A mirror-symmetric cell division that orchestrates neuroepithelial morphogenesis. *Nature*, 446(7137):797–800, 2007.

M. Temerinac-Ott, O. Ronneberger, P. Ochs, W. Driever, T. Brox, and H. Burkhardt. Multiview deblurring for 3-d images from light-sheet-based fluorescence microscopy. *IEEE Transactions on Image Processing*, 21(4):1863–1873, 2012.

P. Thévenaz and M. Unser. Optimization of mutual information for multiresolution image registration. *IEEE Transactions on Image Processing*, 9(12):2083–2099, 2000.

P. Thévenaz, U. E. Ruttimann, and M. Unser. A pyramid approach to subpixel registration based on intensity. *IEEE Trans. Image Proc.*, 7(1):1–15, 1998.

S. Tlili, C. Gay, F. Graner, P. Marcq, F. Molino, and P. Saramito. Colloquium: Mechanical formalisms for tissue dynamics. *The European Physical Journal E*, 38(5):1–31, 2015.

R. Tomer, K. Khairy, F. Amat, and P. J. Keller. Quantitative high-speed imaging of entire developing embryos with simultaneous multiview light-sheet microscopy. *Nature methods*, 9(7):755–763, 2012.

X. Trepat, M. R. Wasserman, T. E. Angelini, E. Millet, D. A. Weitz, J. P. Butler, and J. J. Fredberg. Physical forces during collective cell migration. *Nature physics*, 5(6):426–430, 2009.

R. S. Udan, V. G. Piazza, C.-w. Hsu, A.-K. Hadjantonakis, and M. E. Dickinson. Quantitative imaging of cell dynamics in mouse embryos using light-sheet microscopy. *Development*, 141(22):4406–4414, 2014.

C. G. Vasquez, M. Tworoger, and A. C. Martin. Dynamic myosin phosphorylation regulates contractile pulses and tissue integrity during epithelial morphogenesis. *The Journal of cell biology*, 206 (3):435–450, 2014.

M. von Dassow and L. A. Davidson. Variation and robustness of the mechanics of gastrulation: The role of tissue mechanical properties during morphogenesis. *Birth Defects Research Part C: Embryo Today: Reviews*, 81(4):253–269, 2007.

J. H. Wang and J.-S. Lin. Cell traction force and measurement methods. *Biomechanics and modeling in mechanobiology*, 6(6):361–371, 2007.

Q. Wang, J. J. Feng, and L. M. Pismen. A cell-level biomechanical model of drosophila dorsal closure. *Biophysical journal*, 103(11):2265–2274, 2012.

R. M. Warga and D. A. Kane. One-eyed pinhead regulates cell motility independent of squint/cyclops signaling. *Developmental biology*, 261(2):391–411, 2003.

A. R. Wells, R. S. Zou, U. S. Tulu, A. C. Sokolow, J. M. Crawford, G. S. Edwards, and D. P. Kiehart. Complete canthi removal reveals that forces from the amnioserosa alone are sufficient to drive dorsal closure in drosophila. *Molecular biology of the cell*, 25(22):3552–3568, 2014.

S. Wolf, W. Supatto, G. Debregeas, P. Mahou, S. G. Kruglik, J.-M. Sintes, E. Beaurepaire, and R. Candelier. Whole-brain functional imaging with two-photon light-sheet microscopy. *Nature methods*, 12(5):379–380, 2015.

G. Wollny, M. Ledesma-Carbayo, P. Kellman, and A. Santos. Exploiting quasiperiodicity in motion correction of free-breathing myocardial perfusion MRI. *Medical Imaging, IEEE Transactions on*, 29(8):1516–1527, 2010.

K. Woo and S. E. Fraser. Order and coherence in the fate map of the zebrafish nervous system. *Development*, 121(8):2595–2609, 1995.

S. Xie and A. Martin. Intracellular signalling and intercellular coupling coordinate heterogeneous contractile events to facilitate tissue folding. *Nature communications*, 6:7161, 2015.

L. Yang, N. Y. Ho, R. Alshut, J. Legradi, C. Weiss, M. Reischl, R. Mikut, U. Liebel, F. Muller, and U. Strahle. Zebrafish embryos as models for embryotoxic and teratological effects of chemicals. *Reproductive Toxicology*, 28(2):245–253, 2009.

E. A. Zamir, B. J. Rongish, and C. D. Little. The ECM moves during primitive streak formation-computation of ECM versus cellular motion. *PLoS biology*, 6(10):e247, 2008.